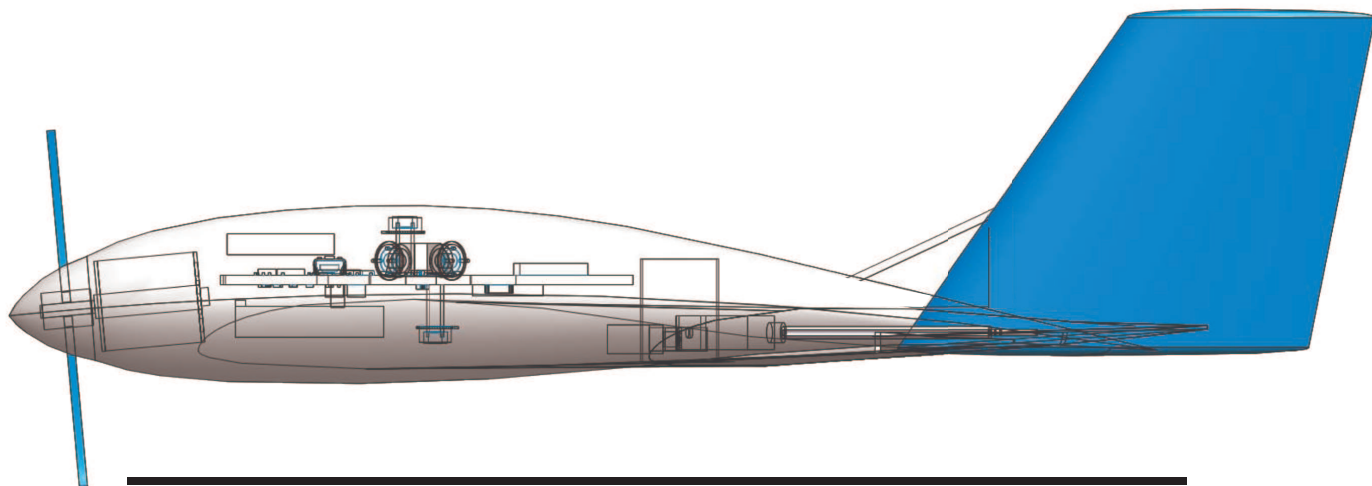


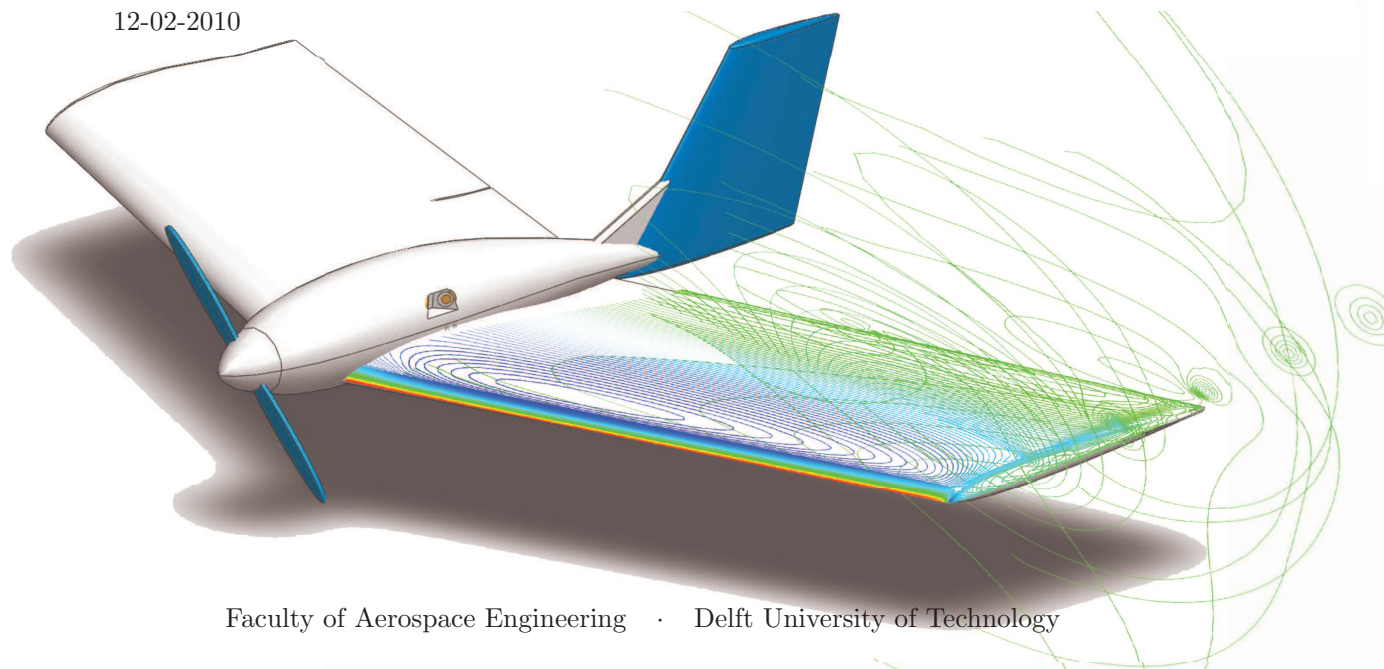
MASTER OF SCIENCE THESIS



Aerodynamic Design and Optimization of a Long Range Mini-UAV

Dennis Trips B.Sc.

12-02-2010



Faculty of Aerospace Engineering · Delft University of Technology



Aerodynamic Design and Optimization of a Long Range Mini-UAV

MASTER OF SCIENCE THESIS

For obtaining the degree of Master of Science in Aerospace
Engineering at Delft University of Technology

Dennis Trips B.Sc.

12-02-2010



Copyright © Dennis Trips B.Sc.
All rights reserved.

DELFT UNIVERSITY OF TECHNOLOGY
DEPARTMENT OF
SYSTEM ENGINEERING AND AIRCRAFT DESIGN

The undersigned hereby certify that they have read and recommend to the Faculty of Aerospace Engineering for acceptance a thesis entitled “**Aerodynamic Design and Optimization of a Long Range Mini-UAV**” by **Dennis Trips B.Sc.** in partial fulfillment of the requirements for the degree of **Master of Science**.

Dated: 12-02-2010

Head of the SEAD department:

Prof. dr. ir. M. van Tooren

Supervisor:

MSc. M.H. Straathof

Second supervisor:

MSc. ing. B.D.W. Remes

Reader:

Ir. W.A. Timmer

Acknowledgements

First of all I want to thank my supervisor Michiel Straathof for always providing assistance whenever needed and for dealing with the tedious task of correcting this report. I also wish to address my gratitude towards the people of the MAVLab. Bart Remes and Rick Ruijsink who provided a lot of guidance and experience during the practical parts of this assignment. Christophe de Wagter for helping out with the autopilot and for flying the mini-UAV in manual mode. Guido de Croon for helping in organizing the EMAV2009 and providing ideas on optimization tools.

I also wish to thank Bart Bruggeman, Vinodh Gunaseelan, Remco Zwinderman, Tamara Doornbos and Ritesh Sharma for helping out with building the models, balance and aircraft. Without their help this thesis would not have been possible.

Thanks also goes out to the guys in “de put” for the great moments spent together in our office and to Sejla Lagumdzija for designing the front cover of this thesis.

Last but not least I want to thank my parents for always trying to help the best they can and for giving me the opportunity to become an aerospace engineer.

I wish to dedicate this thesis to my brother, Benny Trips.

Abstract

This thesis focuses on the development of an aerodynamic optimization algorithm for long range mini-UAV's. This algorithm is applied to the design of the TU Delft mini-UAV that participated in the EMAV2009 outdoor endurance mission. The analysis of the low Reynolds number ($< 2.5 \cdot 10^5$) aerodynamics on the wing is performed using a quasi-3D method which combines a vortex lattice method with viscous airfoil data. The optimization part of the program is accomplished by a sequential quadratic programming algorithm. RANS-CFD calculations and wind tunnel experiments were performed to validate the newly developed quasi-3D method. The final design for the mini-UAV has lift over drag ratio of 11.8 and a high capacity battery (8Ah) which give it a total range of 166 km.

Contents

Acknowledgements	v
Abstract	vi
List of Figures	xvi
List of Tables	xvii
Nomenclature	xix
1 Introduction	1
2 Assignment Description	3
2.1 Thesis Project Description	3
3 Theory	5
3.1 Aerodynamics	5
3.1.1 Lift	5
3.1.2 Drag	10
3.1.3 Stability	27
3.2 Optimization	34
3.2.1 The Optimization Algorithm	34
3.2.2 Variables and Constraints	37
3.2.3 The Optimization Objective	38
4 Implementation of the Theory	45
4.1 Program Setup	45
4.1.1 Program Initialization	46
4.1.2 Changing the Wing Twist	50

4.1.3	Evaluating the Objective Function	51
4.1.4	Checking Termination Criteria and Non-linear Constraints	51
4.1.5	Determining the New Search Direction	53
4.1.6	Changing the Wing Geometry and the Flight Speed	53
4.1.7	Airfoil Data Storage and Retrieval	54
4.1.8	AVL and Xfoil Settings	58
4.2	Differences between the Quasi-3D Method and the Theory	59
4.2.1	Problems with the Induced Drag	60
4.2.2	Improved Estimation of the Zero Lift Angle of Attack	60
4.3	Quantitative Validation of the Quasi-3D Method	63
4.3.1	Validation with CFD	63
4.3.2	Validation with Wind Tunnel Results	74
4.3.3	General Validation Conclusions	82
4.4	Qualitative Comparison of the Quasi-3D Method to Fluent	82
4.4.1	Time Required for an Aerodynamic Evaluation	83
4.4.2	Low Reynolds Number Viscous Effects	83
4.4.3	Easy Generation of the Mesh	84
5	Wind Tunnel Experiments	85
5.1	Wind Tunnel Measurement Setup	86
5.1.1	The Low Speed Low Turbulence Wind Tunnel	86
5.1.2	Balance	87
5.1.3	Wind Tunnel Model Construction	97
5.1.4	Wind Tunnel Test Plan	100
5.2	Wind Tunnel Results	104
5.2.1	Force Measurements	104
5.2.2	Boundary Layer Visualizations	114
5.3	Conclusions Concerning the Wind Tunnel Experiments	122
6	Results	125
6.1	Optimization Results	125
6.1.1	Optimization with Tight Constraints and the Prototype as an Initial Point	126
6.1.2	Optimization with Tight Constraints and an Inferior Initial Point	131
6.1.3	Optimization with Relaxed Constraints	134
6.2	The Competition Aircraft	137
6.2.1	Geometric and Structural Details	137
6.2.2	Aircraft Components	138
6.2.3	Aerodynamics and Performance Details	142
7	Conclusions and Recommendations	147
7.1	Conclusions	147
7.2	Recommendations	149

A Original Assignment Formulation	155
B Wing Geometry Details	157
C ATI Nano 17 SI-25-0.25 Data Sheet	159
D 3-Views	161

List of Figures

3.1	Values of K_v plotted against the aspect ratio corrected for the mach number (figure is extracted from reference [16] page 28).	7
3.2	Lift coefficient comparison between equation 3.1 and wind tunnel data for a thick straight wing at different aspect ratios (figure is extracted from [16] page 48).	8
3.3	Comparison between a potential method, equation 3.1 and Fluent for a 20° sweep, $A = 3$ wing.	8
3.4	Comparison between a thick airfoil, turbulent, viscous, lift curve and a thin airfoil inviscid lift curve. Both calculations are performed with Xfoil. . . .	9
3.5	Overview of the different drag contributions and the defenition of $C_{D_{ref}}$ and $C_{L_{ref}}$	11
3.6	Visualization of the angles and forces present in the quasi-3D method to combine a inviscid lift distribution with viscous airfoil data. (L' = local lift force from lift distribution, l = viscous airfoil lift force (at α_{eff}), D' = local total (profile and induced) drag force, d = airfoil profile drag force (at α_{eff})).	13
3.7	Definition of the forces and angles used to determine the inviscid downwash angle.	15
3.8	Illustration of a laminar separation bubble on an airfoil (picture extracted from ref. [7] page 74).	18
3.9	Pressure arrows for an airfoil at $Re = 3000000$ (no bubble) and for $Re = 500000$ (bubble present).	18
3.10	Edge velocity and momentum loss jumps at reattachment (figure copied from ref. [12] page 725).	19
3.11	Illustration of a typical pressure gradient for Low Reynolds number airfoils.	20
3.12	Effect of the transition location on bubble size and momentum loss (figure copied from ref. [12] page 726).	21
3.13	Friction drag coefficient for plane surfaces plotted against the Reynolds number (page 2-6 reference [15]).	22

3.14	Parasitic interference drag in the corner between a wing and a fuselage for different longitudinal locations of the wing/vertical tail (page 8-15 reference [15]).	25
3.15	Illustration of forces and moments involved in trimming an aircraft ($L =$ lift, $D =$ drag, $M =$ aerodynamic moment, $W =$ aircraft weight).	30
3.16	Evolution from a normal configuration to a swept tailless aircraft.	32
3.17	Forces and moments contributing to the wing moment coefficient.	32
4.1	Program flow diagram.	46
4.2	Overview of the program structure, in which it is visualized how functions relate to each other.	47
4.3	Example of the geometric variables for a wing with three sections (the subscripts define the vector element).	49
4.4	Illustration of the iterative loop to determine the required twist.	50
4.5	Effects of bubble bursting and the comparison with Xfoil results (figure obtained from reference [8]).	53
4.6	Overview of how the airfoil aerodynamic data is stored in a structured way.	55
4.7	Overview of how the airfoil aerodynamic data is created and retrieved.	56
4.8	Interpolation for airfoil aerodynamic data retrieval.	57
4.9	Comparison between original paneling (upper airfoil) with 77 panels and the rearranged paneling with 240 elements (lower airfoil).	58
4.10	Comparison between Xfoil calculations at different turbulence levels.	59
4.11	Typical AVL grid.	60
4.12	Inviscid, thin definition of α_0	61
4.13	Viscous definition of α_0	62
4.14	Outer dimensions of the domain around the wing.	64
4.15	Refinement of the grid around the wing. The denser grid to capture the boundary layer is clearly visible in the left picture. The refinement of the grid near the edges (leading edge , trailing edge and the tip) can be seen in the top view of the wing in the right picture.	64
4.16	Variation of $(\frac{C_L}{C_D})_{max}$ against the taper ratio.	67
4.17	Variation of $(\frac{C_L}{C_D})_{max}$ against the sweep.	67
4.18	Validation plot for wing001000.	69
4.19	Validation plot for wing000500.	70
4.20	Validation plot for wing000300.	71
4.21	Validation plot for wing201000.	72
4.22	Validation plot for wing401000.	73
4.23	Variation of $(\frac{C_L}{C_D})_{max}$ against the sweep.	75
4.24	Validation plot for NACA2400.	77
4.25	Validation plot for NACA24150.	78
4.26	Validation plot for NACA24300.	79

4.27	Validation plot for NACA243085.	80
4.28	Validation plot for NACA3-10-18.	81
5.1	Wind tunnel measurement setup.	86
5.2	Nano 17 force/torque sensor system with data logging card.	88
5.3	Wind tunnel balance yaw and pitch system.	88
5.4	Finished yaw-pitch system with the sensor connected on top.	89
5.5	SPG785A-BM servo gearbox.	90
5.6	Definition of the pitch-offset angle.	91
5.7	Visualization of the rotation between the sensor reference system and the aerodynamic reference system.	93
5.8	Values of K_1 and K_3 for a number of bodies (figure obtained from reference [23]).	94
5.9	Values of τ_1 for a number of tunnel types. Use $b/B = 0$ for bodies of revolution (figure obtained from reference [23]).	94
5.10	Principle of modeling the lift interference effect trough mirroring horse-shoe vortices with respect to the wind tunnel walls (figure obtained from reference [30]).	96
5.11	Wing, upper and lower surface, production molds in the process of being prepared for production.	98
5.12	Foam core, of which two are needed during the construction of the wing, and the CNC-hotwire foam cutter.	99
5.13	The finished competition aircraft.	100
5.14	Lift coefficient against the angle of attack for the S5010 airfoil.	105
5.15	Lift coefficient against the angle of attack for the Prototype wing. Experimental data compared to CFD and the quasi-3D method.	106
5.16	Drag polar for elevons in neutral position and for a deflection of 7.5° up.	106
5.17	Drag polar for elevons in neutral position and for a deflection of 7.5° up.	107
5.18	Servo mount for the pitch servo.	109
5.19	Forces acting on the balance head causing strain in the system.	111
5.20	Changes in the lift coefficient due to a strain correction on the results.	112
5.21	Changes in the drag polar due to a strain correction on the results.	112
5.22	Changes in the lift over drag ratio due to a strain correction on the results.	113
5.23	Drag polar for angles of attack going from $0^\circ \rightarrow 22^\circ \rightarrow -8^\circ \rightarrow 0^\circ$	113
5.24	Effect of the pitch-offset angle on the lift over drag ratio.	114
5.25	Effect of the pitch-offset angle on the drag coefficient.	115
5.26	Boundary layer visualization for prototype A (upper) and prototype B (lower) at $\alpha = 5^\circ$	116
5.27	Boundary layer features on the S5010 airfoil at $\alpha = 5^\circ$ and $Re = 2 \cdot 10^5$	116
5.28	Illustration of a rounded tip and a straight tip with there tip vortex.	117
5.29	Boundary layer visualization for prototype A at $\alpha = 5^\circ$ and a turbulator strip at 5% of the chord length.	118

5.30	Boundary layer visualization for prototype A at $\alpha = 5^\circ$, with a turbulator strip encapsulated by the bubble.	118
5.31	Boundary layer visualization of upper and lower wing surface for prototype B at different angles of attack.	120
5.32	Boundary layer comparison between a propeller off and a propeller/motor on case for prototype B ($\alpha = 5^\circ$).	121
5.33	Boundary layer comparison for the prototype B wing with the elevons neutral and 11° ($\alpha = 5^\circ$).	122
6.1	Comparison between the initial wing geometry and the resulting geometry after the optimization.	128
6.2	Lift over drag ratio for different velocities, maintaining straight, level and trimmed flight.	129
6.3	Aerodynamic coefficients for the optimized wing at $19.1m/s$	130
6.4	Comaprison between optimized wing from section 6.1.1(red) and the optimization of this section (green).	132
6.5	Aerodynamic coefficients for the optimized wing at $19.3m/s$	133
6.6	Comaprison between optimized wing from section 6.1.1 (upper) and the optimization of this section (lower).	135
6.7	Aerodynamic coefficients for the optimized wing.	136
6.8	polars for the S5010 airfoil at a Reynolds number of $2 \cdot 10^5$	137
6.9	General overview of the electric layout for the EMAV2009 competition aircraft.	139
6.10	Autopilot build into the prototype aircraft.	139
6.11	Range plotted against the battery capacity(ranging from 0-200 Ah), for a fixed aircraft shape with a varying weight with respect to the battery capacity, and a $5W$ subsystem power consumption.	141
6.12	Range plotted against the battery capacity(ranging from 0-15 Ah), for a fixed aircraft shape with a varying weight with respect to the battery capacity, and a $5W$ subsystem power consumption.	142
6.13	Subsystem locations in the aircraft.	144
6.14	Aerodynamic coefficients for the TRIP50 aircraft at $20m/s$	145
C.1	Nano 17 dimensions.	160
D.1	Three view of Prototype A and the TRIP50.	162
D.2	Three view of Prototype B.	163

List of Tables

3.1	Comparison between calculated and experimental drag coefficients for streamlined bodies of revolution (drag coefficients are based on the fuselage wetted area).	24
3.2	Comparison between experiments/CFD and the calculated aerodynamic center using equation 3.32 and 3.36.	29
3.3	Flying plank airfoils with corresponding moment coefficients and zero lift angles of attack.	31
4.1	Comparison of $(C_L/C_D)_{max}$ and its corresponding lift coefficient, between CFD and the quasi-3D method.	66
4.2	Comparison of $(C_L/C_D)_{max}$ and its corresponding lift coefficient, between experimental results and the quasi-3D method.	74
5.1	Overview of components involved in setting the pitch angle and their likelihood of causing errors.	108
5.2	Wing geometries of the two prototypes.	114
6.1	Wing planform of the TRIP50.	138
6.2	Tail planform of the TRIP50.	138
6.3	Weight breakdown of the TRIP50.	143
B.1	Wing geometries used for the Quasi-3D validation.	158
C.1	Force range and resolution information for the Nano 17 SI-25-0.25.	159
C.2	Calculated stiffness information for the Nano 17 SI-25-0.25.	159

Nomenclature

Latin Symbols

A	Aspect ratio	[-]
A_{tun}	Wind tunnel aspect ratio	[-]
b	Wing Span	[m]
b^*	Fuselage width at largest cross-section	[m]
C	Battery Capacity	[Ah]
c	Chord length	[m]
C'	Wind tunnel cross-sectional area of the test section	[m^2]
c_{avg}	Average geometric wing chord	[m]
C_D	Aircraft drag coefficient	[-]
C_{D_b}	Induced interference drag (referred to $S_{covered}$)	[-]
C_{D_c}	Corrected drag coefficient	[-]
C_{D_i}	Induced drag coefficient	[-]
C_{D_p}	Profile drag coefficient	[-]
C_{D_s}	Secondary drag coefficient	[-]
$C_{D_{fus}}$	Fuselage drag coefficient	[-]
$C_{D_{int_{tail}}}$	Fuselage-tail interference drag	[-]
$C_{D_{int}}$	Interference drag coefficient	[-]
$C_{D_{ref}}$	Reference drag coefficient	[-]
$C_{D_{strip}}$	Drag coefficient calculated with the strip method	[-]
$C_{D_{tail}}$	Tail drag coefficient	[-]
$C_{D_{tot_w}}$	Total wing drag coefficient	[-]

C_{D_v}	Vortex drag coefficient	[-]
C_f	Friction coefficient	[-]
$C_{f_{fus}}$	Fuselage friction coefficient	[-]
$C_{f_{lam}}$	Laminar friction coefficient	[-]
$C_{f_{turb}}$	Turbulent friction coefficient	[-]
$C_{L'}$	Local lift coefficient perpendicular to V_∞	[-]
C_L	Aircraft lift coefficient	[-]
C_l	Airfoil lift coefficient	[-]
$C_{L_c^*}$	Corrected C_L^*	[-]
C_{L^*}	Moment coefficient of L^*	[-]
C_{L_α}	Aircraft lift curve slope	[-]
C_{l_α}	Airfoil lift curve slope	$[\frac{1}{\circ}]$
C_{L_b}	Lift coefficient due to wing fuselage interaction (referred to $S_{covered}$)	[-]
C_{L_c}	Corrected lift coefficient	[-]
C_{L_p}	Aircraft potential (linear) lift coefficient	[-]
C_{L_v}	Aircraft vortex (non-linear) lift coefficient	[-]
$C_{l_{\alpha visc}}$	Lift curve slope for the viscous airfoil data	$[\frac{1}{\circ}]$
$C_{L_{max}}$	Aircraft maximum lift coefficient	[-]
$C_{L_{ref}}$	Reference lift coefficient	[-]
C_M	Aircraft moment coefficient	[-]
C_{M_1}	Wing moment coefficient due to airfoil moment coefficients	[-]
C_{M_2}	Wing moment coefficient due to the lift distribution at zero total lift	[-]
C_{M_c}	Corrected C_M	[-]
$C_{M_{\delta_e}}$	Change in the moment coefficient due to an elevator deflection	$[\frac{1}{\circ}]$
$C_{M_{ac_w}}$	Moment coefficient at the wing aerodynamic center	[-]
$C_{m_{ac}}$	Airfoil moment coefficient around its aerodynamic center	[-]
$C_{M_{origin\alpha}}$	Moment coefficient slope, at the wing origin, with respect to the angle of attack	[-]
$C_{M_{origin}}$	Moment coefficient at the wing origin	[-]
c_{mac}	Mean aerodynamic chord	[m]
C_N	Moment coefficient of N	[-]
C_{N_c}	Corrected C_N	[-]
c_{ref}	Reference chord length (mean aerodynamic chord)	[m]
c_{root}	Root chord	[m]
C_{S^*}	Side force coefficient	[-]
C_{S_c}	Corrected side force coefficient	[-]
c_{tip}	Tip chord	[-]
D	Drag force	[N]
d	Airfoil drag force at α_{eff}	[N]

D'	Local total (viscous and induced) drag coefficient	$[N]$
d^*	Fuselage diameter of the largest cross-section	$[m]$
d_{eq}^*	Fuselage equivalent diameter	$[m]$
E	Flight endurance	$[s]$
e	Oswald factor	$[-]$
f	Empirical correction factor to correct C_{M_1} for planform effects	$[-]$
F_x, F_y, F_z	Aerodynamic forces in the sensor reference frame	$[N]$
$F_{z_{aero}}$	Aerodynamic force in the sensor z-axis	$[N]$
H	Shape factor	$[-]$
h	Height of the wind tunnel test section	$[m]$
h^*	Fuselage height at largest cross-section	$[m]$
$I_{el_{prop}}$	Electrical current used for propulsion	$[A]$
$I_{el_{sub}}$	Electrical current used by all non-propulsive subsystems	$[A]$
I_{el}	Electrical current	$[A]$
k	Induced drag amplification factor	$[-]$
K_p	Potential lift parameter	$[-]$
K_v	Vortex parameter	$[-]$
K_{t_y}	Torsional stiffness of the sensor	$[\frac{Nm}{\circ}]$
$K_{t_{tot}}$	Total torsional stiffness of the balance	$[\frac{Nm}{\circ}]$
L	Lift force	$[N]$
l	Airfoil lift force at α_{eff}	$[N]$
L'	Local lift coefficient in a lift distribution over a wing	$[N]$
L^*	Aerodynamic moment around the velocity axis	$[Nm]$
l^*	Fuselage length	$[m]$
M	Aerodynamic moment around the lateral aerodynamic axis	$[Nm]$
M'	Mach number	$[-]$
N	Aerodynamic moment around the vertical aerodynamic axis	$[Nm]$
n_{crit}	Critical amplification ratio	$[-]$
p	Profile drag amplification factor	$[-]$
P_r	Power required	$[W]$
P_{el}	Electrical power	$[W]$
q	Dynamic pressure	$[\frac{kg}{m \cdot s^2}]$
q_c	Corrected dynamic pressure	$[\frac{kg}{m \cdot s^2}]$
R	Range	$[m]$
Re	Reynold number	$[-]$
Re_{eff}	Local Reynolds number based on V_{eff}	$[-]$
Re_{fus}	Fuselage Reynolds number	$[-]$
Re_{min}	Lowest Reynold number on the wing	$[-]$

S	Wing surface area	$[m^2]$
S'	Strip surface area	$[m^2]$
S^*	Aerodynamic side force	$[N]$
S_s	Reference surface areas of the secondary drag coefficients	$[m^2]$
S_v	Vertical tail surface area	$[m^2]$
$S_{covered}$	The wing area covered by the fuselage	$[m^2]$
S_{fus}	Fuselage largest cross-sectional area	$[m^2]$
S_{ref}	Reference area (equal to the wing area)	$[m^2]$
T_x, T_y, T_z	Measured aerodynamic moments in the sensor reference frame	$[Nm]$
$T_{y_{aero}}$	Aerodynamic moment around the sensor y-axis	$[Nm]$
u_e	Boundary layer edge velocity	$[\frac{m}{s}]$
U_{el}	Electrical tension	$[V]$
V_∞	Freestream velocity	$[\frac{m}{s}]$
V_{bal}	Balance volume	$[m^3]$
V_{eff}	Local effective velocity	$[\frac{m}{s}]$
V_{fus}	Fuselage Volume	$[m^3]$
V_{stall}	Stall speed	$[\frac{m}{s}]$
V_{wing}	Wing volume	$[m^3]$
W	Aircraft weight	$[N]$
x	Longitudinal coordinate (positive rearward)	$[m]$
x_n	Longitudinal location of the neutral point	$[m]$
x_{ac_v}	Aerodynamic center of the vertical tail	$[m]$
x_{ac}	Longitudinal location of the wing aerodynamic center	$[m]$
x_{cg}	Longitudinal location of the center of gravity	$[m]$
$x_{tr_{low}}$	Transition point on the lower surface of the airfoil	$[\%c]$
$x_{tr_{up}}$	Transition point on the upper surface of the airfoil	$[\%c]$
x_{tr}	Longitudinal location of the transition point as a percentage of the length it acts on	$[\%c]$
y	Lateral coordinate (positive to the right)	$[m]$
z	Normal coordinate (positive downward)	$[m]$
\mathbf{c}	Vector containing the design constants for the optimization	$[-]$
\mathbf{x}^*	Vector containing the optimized design variables	$[-]$
\mathbf{x}	Vector containing the design variables for the optimization	$[-]$

Greek Symbols

α	Angle of attack	$[^\circ]$
α_0	Zero lift angle of attack	$[^\circ]$

α_i	Induced downwash angle	[°]
$\alpha_{0_{visc}}$	Zero lift angle of attack for the viscous airfoil data	[°]
α_{eff}	Effective angle of attack ($\alpha_{eff} = \alpha - \epsilon$)	[°]
α_{inc}	Incidence angle between the wing zero lift line and the fuselage axis	[°]
α_{offset}	Pitch offset angle between the sensor and the aircraft	[°]
β	Side slip angle	[°]
β'	$\sqrt{1 - M'^2}$	[-]
$\Delta\alpha_{linkage}$	Difference in the pitch angle due to strain in the linkage	[°]
$\Delta\alpha_{maxHF}$	Difference in the pitch angle due to exceeding the servo maximum hold force	[°]
$\Delta\alpha_{offset}$	Error in the pitch offset angle	[°]
$\Delta\alpha_{play}$	Difference in the pitch angle due to play	[°]
$\Delta\alpha_{sensor}$	Difference in the pitch angle due to torsional stiffness of the sensor	[°]
$\Delta\alpha_{servo}$	Difference in the pitch angle due to strain on the servo	[°]
$\Delta\alpha_{strain}$	Difference in the pitch angle due to the total strain	[°]
δ^*	Boundary layer displacement thickness	[m]
ϵ	Geometric twist angle	[°]
ϵ_{SB_w}	Velocity increase due to the solid blockage of the wing	[-]
$\epsilon_{SB_{bal}}$	Velocity increase due to the solid blockage of the wind tunnel balance	[-]
$\epsilon_{SB_{fus}}$	Velocity increase due to the solid blockage of the fuselage	[-]
$\epsilon_{SB_{wake}}$	Velocity increase due to the solid blockage of the wind tunnel wake	[-]
ϵ_{SB}	Total velocity increase due to the solid blockage	[-]
η_j	Propulsive efficiency	[-]
η_{tot}	Total propulsive efficiency, from batteries to prop	[-]
λ	Taper Ratio	[-]
$\Lambda_{0.25}$	Quarter chord sweep angle	[°]
$\Lambda_{0.5}$	Mid chord sweep angle	[°]
ν	Kinematic viscosity	$[\frac{m^2}{s}]$
ρ	Air density	$[\frac{kg}{m^3}]$
σ	Stability margin	[-]
θ	Momentum loss thickness	[m]
ξ, η	Boundary layer coordinates	[m]

Abbreviations

DAR	Design integration and operation of Aircraft and Rotorcraft
EMAV	European Micro Aerial Vehicle competition
LTT	Low speed Low Turbulence wind Tunnel

mini-UAV Mini Unmanned Aerial Vehicle

SEAD System Engineering and Aircraft Design

Chapter 1

Introduction

In the last decade a lot of UAV's have been developed for military applications. These UAV's are mostly very large and have performance capabilities equal to or better than manned aircraft. However a trend is observed towards smaller, mini-UAV's, that serve the purpose of being an "eye in the sky" for information gathering and reconnaissance missions. These applications might also serve civil purposes, e.g. assisting fire-fighter crews, power line inspections and filming sports events. Miniaturization of electronics and major leaps in battery technology have pushed the development of mini-UAV's towards practical applications. However the development of knowledge on designing high performance aircraft in this field has still a long way to go. Up until now, the aerodynamics for mini-UAV's is hardly understood as remote controlled toy planes were the only beneficiaries of this knowledge. The available computational aerodynamics tools, including advanced CFD methods, are incapable of predicting the low Reynolds number ($< 2.5 \cdot 10^5$) flow phenomena on wings. The best tool available at this moment is Xfoil which provides a reasonable approximation of the low Reynolds number effects on airfoils.

This thesis will focus on the aerodynamic design of a mini-UAV that will compete in the EMAV2009 (European Micro Aerial Vehicle Competition 2009) endurance mission. The mission consists out of several phases but the focus lies on flying as far as possible. To obtain this goal an aerodynamic tool will have to be developed for the analysis of the aerodynamic forces acting on the wing. These forces are required for obtaining information on the aerodynamic efficiency of the aircraft and to determine its range capabilities. An optimization algorithm will be added on top of this analysis tool to establish the best possible preliminary design. It was decided that a tailless aircraft configuration would be the starting point of the design, putting the focus on the wing design. This requires that the neutral point of the aircraft and the moment acting on it will have to be predicted very accurately to establish stable trimmed flight. Literature on wind tunnel force measurements and advanced CFD methods will be used to validate the data.

Wind tunnel tests are required to validate the results obtained with the wing optimization tool. Two models will be tested in the low-speed, low-turbulence wind tunnel of the TU Delft. The small forces acting on mini-UAV's require a new balance for force

measurements. Especially the drag force is really small, but it has to be determined very accurately to establish a validation for the aerodynamic efficiency.

Several DAR-exercises will be performed on the practical side of the thesis work. A summary of these exercises will be presented throughout this document. Those assignments consist of: milling molds, building wind tunnel models, designing and building a new wind tunnel balance and designing the propulsion system for the competition aircraft.

In chapter 2 a detailed description of the assignment is presented and a project goal is formulated. This is followed by chapter 3 with an in dept theoretical investigation to establish the tools required for the creation of the aerodynamic analysis program. Next, a short introduction into the theory behind the sequential quadratic programming algorithm is presented. This algorithm will be used to perform the optimization. Several objective functions will be formulated for the design of electrically powered aircraft. The final implementation of this knowledge is presented in chapter 4 together with an extensive validation of the developed aerodynamics analysis tool. Details on the preparations for and the results of the wind tunnel experiments will be presented in chapter 5. This is followed by an analysis of the results obtained with the optimization algorithm, in chapter 6. Finally, in chapter 7, the conclusions and recommendations will be formulated.

Chapter 2

Assignment Description

In this chapter, the thesis assignment is summarized, and slightly adapted from the original one. A project goal will be formulated which will function as a guideline for this thesis. The original assignment description can be found in appendix A.

2.1 Thesis Project Description

The main goal of the thesis work is to find an optimal aerodynamic shape for a mini-UAV that will participate in the EMAV2009 competition. The requirements of this competition put certain restrictions on the maximum size of the aircraft and, for safety reasons, on its momentum. The aircraft should fit, in all configurations, in a sphere of 50 cm diameter and the maximum momentum should be lower than $20 \frac{kg \cdot m}{s}$ (for detailed competition rules, see ref [2]). The objective of the competition is to fly as far as possible resulting in a maximization of the lift over drag ratio.

The proposed use of FLUENT is partially discarded due to its inability to change the geometry and grid in an automated manner, its inability to predict the location of the transition point, and its rather high calculation times. Instead the option of combining a 3D vortex lattice method with a 2D panel method with an added boundary layer will be studied. However, validation of this method can be done by comparing it with FLUENT results and experimental data.

For the optimization it is possible to use different options. As there are metaheuristic algorithms, gradient based optimizers, and the adjoint-equation method. The adjoint equation method is an elaborate method and will probably take longer than a single thesis subject to program.

While optimizing for range it has to take into account that a stable aircraft should be created with sufficient internal space for the electronics. This is to ensure a feasible design with flight characteristics that can be handled by the autopilot.

All this can be summarized in the following project goal.

Project Goal

Design of a mini-UAV for the EMAV 2009 outdoor competition using a novel aerodynamic optimization tool, with the objective to win the competition.

Chapter 3

Theory

In this chapter an explanation will be presented on the aerodynamics that one can expect when working with a tailless mini-UAV's. This is then followed by an explanation on the theory behind the sequential quadratic optimization tool, used to obtain the best aerodynamic shape. A lot of the information in this chapter is gathered from different sources and is synthesized here to provide background information for subsequent chapters.

3.1 Aerodynamics

The focus of this section is on low Reynolds number, low aspect ratio (LAR) wing aerodynamics. The reason to focus on this aerodynamic field lies in the requirements and logical limits set forward for mini-UAV's. Low Reynolds numbers are the result of the low speeds in combination with the small wing chords, while the LAR (< 4) is the result of a combination of different factors, being: high wing loadings due to high aircraft weight, stall speed requirements and limits on the wing span.

3.1.1 Lift

Low aspect ratio wings generate lift due to two effects. As for all wings, lift is generated by the circulation around the wing, also referred to as linear lift because of its linear nature with respect to the angle of attack. A second non-linear lift is due to vortex lift. This vortex lift can be produced on the leading edge of the wing or at the side edges of the wing. The leading edge vortex is generated when the wing is highly swept and when it has a sharp leading edge. The side edge vortex is present on all wings but its effect is only noticed in the wake, while in the case of low aspect ratios (≤ 3.5), the vortex will have its effect on the wake and the wing. The prediction of side vortex flow characteristics is presented in reference [17].

Aircraft Lift Coefficient

For a tailless aircraft configuration the assumption is made that the only part of the aircraft generating lift is the main wing. This lift is thus composed of the above mentioned components and one way of approximating it is by using:

$$C_L = C_{L_p} + C_{L_v} = K_p \cdot \sin \alpha \cdot \cos^2 \alpha + K_v \cdot |\sin \alpha| \cdot \sin \alpha \cdot \cos \alpha \quad (3.1)$$

This equation was created by Polhamus in reference [22]. The potential lift coefficient, C_{L_p} , is dependent on the value of K_p which can be determined by a potential flow calculation at a single angle of attack. However, for this report the determination of the potential lift, at every angle of attack, will be calculated using a vortex lattice method, AVL. The reason for this is that in a latter stage not only the lift coefficient is required, but also the potential lift distribution.

The vortex lift coefficient depends on the angle of attack and the value of K_v . This vortex parameter is the sum of the vortex parameter for the side edge and the leading edge vortex. To generate a leading edge vortex it is required to have separated flow over the leading edge which reattaches aft on the wing. However in the case of mini-UAV's the airfoils will have significant leading edge thickness, which prevents flow separation on the leading edge. This implies that the leading edge vortex is not expected on the mini-UAV wing and will thus not be included in the calculations. Whenever referred to the vortex parameter, K_v , in this report, it will only be due to the side edge vortex (in literature referred to as $K_{v,se}$). The value of K_v for straight, untapered wings can be determined using figure 3.1 (this figure is extracted from reference [16] page 28). For swept tapered wings the calculation of K_v is much more complicated as can be seen in reference [16]. A way to efficiently implement this has not yet been found and thus remains to be determined. The simplification of using the value of K_v for straight wings and linearly scaling it for the taper ratio, is acceptable as the effect of the side edge vortex is already small for the aspect ratios under consideration.

In several reports, e.g. reference [16] and [20], this method of estimating the vortex lift effect has been compared to CFD and experimental results. It proved to work really well for different low aspect ratio wings with or without leading edge vortex. One of the comparisons can be seen in figure 3.2, in which results from equation 3.1 are plotted together with wind tunnel results for a straight wing with a 12.6% thick Göttingen 409 airfoil for different aspect ratios.

In figure 3.3 a comparison is made, for a wing with an aspect ratio equal to 3 and 20° sweep, between a potential flow method (vortex lattice), potential flow with vortex correction and a Fluent calculation. From this figure it can be seen that the difference between the potential flow and Fluent increases with increasing angle of attack, while with the vortex correction the difference is drastically reduced. When assuming Fluent is accurate, this illustrates that the vortex lift correction shows an increased accuracy in the estimation of the lift curve slope. The remaining difference can have different causes as there are, the inviscid and thin wing assumptions for the vortex lattice method, and maybe a small error in the vortex parameter, K_v , for swept wings. The thin wing assumption causes the vortex lattice method to wrongly estimate the zero lift angle of

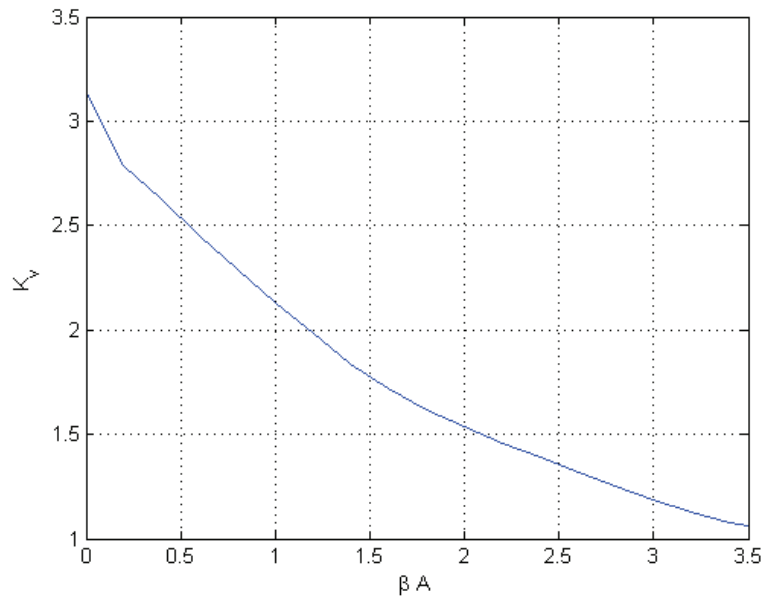


Figure 3.1: Values of K_v plotted against the aspect ratio corrected for the mach number (figure is extracted from reference [16] page 28).

attack by about 0.3° , this explains the constant difference between the curves. In chapter 4 a correction for this difference will be presented. The remaining difference in the lift curve slope is rather small and is also caused by the assumptions of a thin wing in inviscid flow. This is clearly demonstrated when we compare airfoils in Xfoil submitted to the same conditions and assumption as in Fluent and AVL. In figure 3.4 the lift coefficient of the airfoil used in the wings for figure 3.3, is plotted against the angle of attack. The lift coefficient is plotted for the case of a thick airfoil with forced turbulent flow over it at a Reynolds number of 200000, illustrating the Fluent case. The other graph is for the same airfoil but with its thickness to chord ratio reduced to 1% (originally 10%), simulating a thin airfoil, and the calculation was performed for a invicid flow, this compares to the AVL calculation. Two things become clear when looking at figure 3.4 and illustrate the differences found between Fluent and AVL. The zero lift angle of attack for the thin airfoil is 0.36° lower than for the thick airfoil in viscous flow, almost exactly the same difference as mentioned earlier in the 3D-case. The lift curve slope for the thick airfoil is higher as for the thin airfoil, this is also what was expected by looking at figure 3.3. So the differences in figure 3.3, remaining after the vortex lift correction, are caused by the assumptions made in the vortex lattice method.

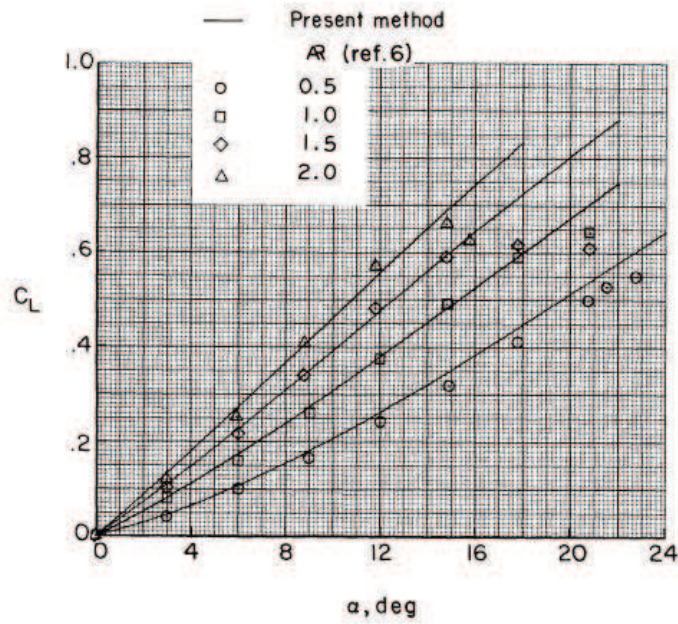


Figure 3.2: Lift coefficient comparison between equation 3.1 and wind tunnel data for a thick straight wing at different aspect ratios (figure is extracted from [16] page 48).

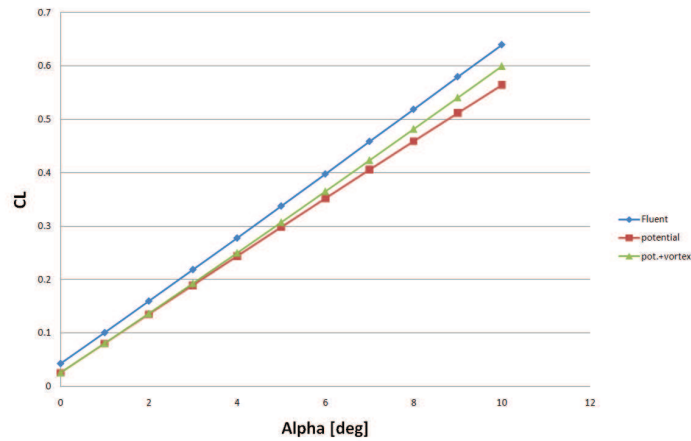


Figure 3.3: Comparison between a potential method, equation 3.1 and Fluent for a 20° sweep, $A = 3$ wing.

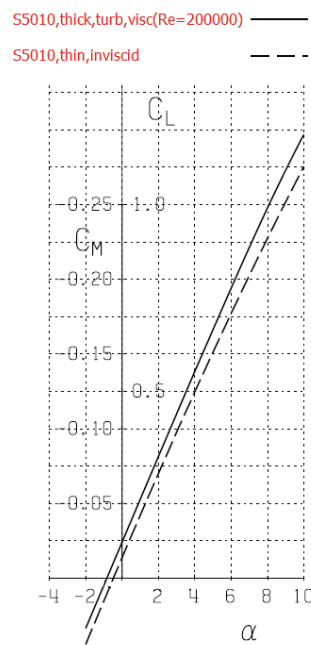


Figure 3.4: Comparison between a thick airfoil, turbulent, viscous, lift curve and a thin airfoil inviscid lift curve. Both calculations are performed with Xfoil.

3.1.2 Drag

In this section an overview will be presented on the aerodynamic drag of tailless mini-UAV's. The performance estimation, which is of major importance for the optimization (see section 3.2.3), will largely depend on the correct calculation of the drag. As an introduction, some attention will be spend on how all drag components are defined in further discussions. As there are a lot of different ways in which drag is subdivided, it is important to create an insight on how they are used in this document. This is followed by a discussion on the drag phenomena for each component, wing, tail and fuselage separately. The last section discusses the drag arising when those components are joint together.

Drag: Overview

In an aircraft drag polar it is customary to distinguish two different types of drag, a lift independent part also referred to as zero lift drag and a lift dependent part. However it is mostly unclear what they are composed of and how they are influenced. Lets start with a breakdown of the overall drag:

$$\begin{aligned}
 D &= C_D q S = \sum C_{D_s} q S_s + C_{D_p} q S + C_{D_i} q S, \\
 &\downarrow \\
 C_D &= \frac{D}{q S} = \frac{\sum C_{D_s} S_s}{S} + C_{D_p} + C_{D_i} \\
 &= \left(\frac{\sum C_{D_s} S_s}{S} + C_{D_p} \right)_{C_L=0} + p C_L^2 + k \frac{C_L^2}{\pi A} \\
 &= C_{D_0} + \frac{C_L^2}{\pi A e} \tag{3.2}
 \end{aligned}$$

The C_{D_s} represent the secondary drag coefficients for e.g. the fuselage, vertical tail. These are assumed independent of lift and are referred to there own reference areas, S_s . In this derivation they are joint under C_{D_0} , which is composed of drag from several components, and by definition is independent of the lift. Examples of components contributing to this part of the drag are the fuselage and the tail assuming small angles of attack. Those components often also present a variation with the angle of attack (lift coefficient), however for the optimization they have an inclination with respect to the wing such that they produce the least amount of drag while cruising.

The profile drag is the total drag of the wing minus the induced drag. This drag can be subdivided into airfoil friction drag and pressure drag. Friction drag is the component of the forces tangential to the airfoil's surface, acting in the direction of the flow. The pressure drag is the component of the forces normal to the surface, in the direction of the flow. These components only exist if the aerodynamic calculations on the airfoil incorporate viscous effects, potential flow calculations on airfoils (2D) produce lift but no drag (d'Alembert's paradox). A part of this drag is constant and will be added to C_{D_0} , while the other part varies with the lift and is incorporated in the second term of equation 3.2.

This second term is often referred to as “induced drag”, however this is a unfortunate name as it incorporates more than just the induced drag. It would be better to refer to it as the lift dependent drag. The Oswald factor, e , combines the induced drag factor, k , and the profile drag factor, p :

$$e = \frac{1}{k + p\pi A} \quad (3.3)$$

The only problem with equation 3.2 is the fact that the minimum drag is found at zero lift. This is however not the case for most of the aircraft with cambered airfoils. The profile drag for positively cambered airfoils has its lowest drag at a positive lift coefficient. For the three dimensional case, at low lift coefficients, the variation in the profile drag dominates over the trend in the induced drag resulting in a slight shift of the minimum drag point to positive lift coefficients (see figure 3.5). As mentioned in reference [29], this can be taken into account in equation 3.2 by defining a $C_{D_{ref}}$ and a $C_{L_{ref}}$. The definition of this $C_{D_{ref}}$ and $C_{L_{ref}}$ can be seen in figure 3.5.

$$C_D = C_{D_{ref}} + \frac{(C_L - C_{L_{ref}})^2}{\pi A e} \quad (3.4)$$

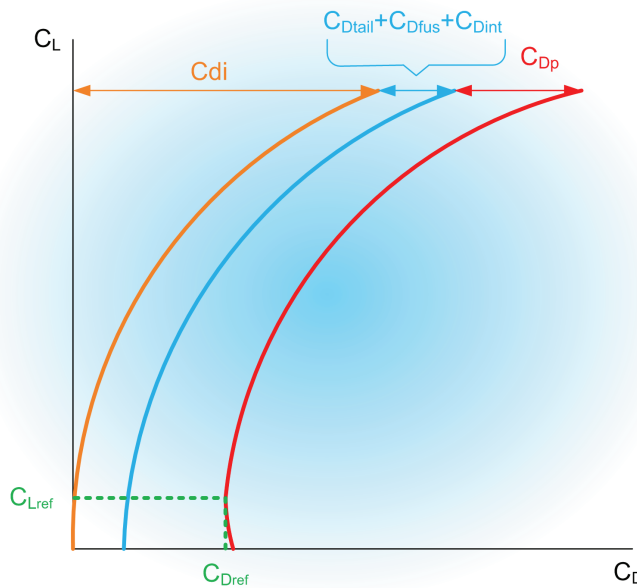


Figure 3.5: Overview of the different drag contributions and the definition of $C_{D_{ref}}$ and $C_{L_{ref}}$.

However, the method used in this report for calculating the wing drag will take the profile drag into account in a different way. The profile drag, and its variation with the lift, will be directly obtained from airfoil data, reducing the problem to the following,

$$C_D = C_{D_{fus}} + C_{D_{tail}} + C_{D_p}(C_L) + C_{D_i}(C_L) + C_{D_{int}} \quad (3.5)$$

In which $C_{D_{fus}}$ and $C_{D_{tail}}$ are invariant with the lift. The last term $C_{D_{int}}$ represents the interference drag which is due to the interference between the different components. The induced drag, C_{D_i} , is calculated using,

$$C_{D_i} = k \frac{C_L^2}{\pi A} \quad (3.6)$$

In this equation k is a amplification factor used for non-elliptical lift distributions.

Equation 3.5 avoids problems like working with reference lift and drag coefficients and it separates the lift dependent drag components.

Wing and Vertical Tail Drag

In this section the profile drag and the induced drag, both dependent on the lift, will be treated. The profile drag is dominant at lower lift coefficients and, at low Reynolds numbers, drag induced by the transitional separation bubble and other viscous effects have a large contribution to the overall drag of the wing. The drag caused by these effects is also highly variable with the lift coefficient (or angle of attack), as for example the transition point and the transitional separation bubble changes location and size with changing angle of attack. To capture these effects a different approach to estimating the profile drag will be explained in the following section.

Drag Estimation for Low Aspect Ratio Wings

It is important to find a fast way of calculating the wing profile drag and induced drag, because optimizations will require repetitive aerodynamic evaluations of different shapes. An interesting way of achieving this goal is by combining viscous airfoil data with a inviscid three dimensional wing calculation.

The viscous airfoil data can be found in literature, e.g. in references [28, 25, 27, 26], or from Xfoil viscous calculations. Xfoil is an airfoil analysis and design tool developed specifically for low Reynolds number airfoils (see reference [4]). It calculates the viscous aerodynamics using a higher order panel method coupled with a viscous/inviscid interaction method.

The three dimensional inviscid calculation can be performed using a vortex lattice method like AVL. Both programs, Xfoil and AVL, are general public licence programs available on the Internet, developed by MIT professor Mark Drela.

In reference [20] a method was described on combining airfoil data with a lift distribution over a wing, and was validated against CFD-results. This method will be repeated here, because of its importance to this report.

The first step in this method is to calculate the lift distribution on the wing using Tornado, a Matlab based vortex lattice method. This lift distribution is used in a strip method to calculate the induced downwash angle, α_i , at every spanwise strip-location. This downwash angle is then used to obtain the effective angle of attack which is required to find the corresponding drag coefficient. Figure 3.6 gives a better insight on how this method works. In this figure one can see the forces and angles at a single spanwise strip-location.

The steps required to combine the airfoil data with the lift distribution are as follows:

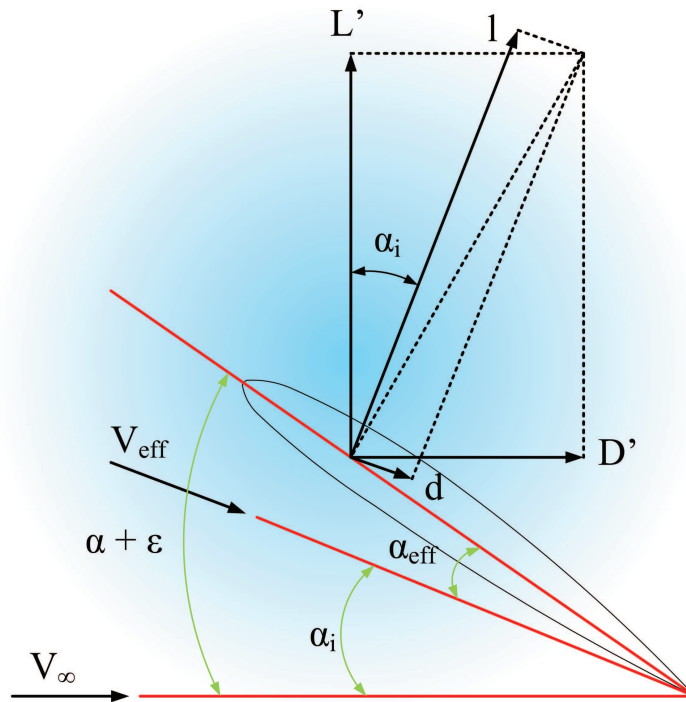


Figure 3.6: Visualization of the angles and forces present in the quasi-3D method to combine a inviscid lift distribution with viscous airfoil data. (L' = local lift force from lift distribution, l = viscous airfoil lift force (at α_{eff}), D' = local total (profile and induced) drag force, d = airfoil profile drag force (at α_{eff})).

1. Run Tornado for the wing at hand
2. Set $\alpha_i = 0$ and $d = 0$
3. $l = (L' + d \cdot \sin(\alpha_i)) / \cos(\alpha_i)$
4. Determine local velocity with $V_{eff} = V_\infty / \cos(\alpha_i)$
5. Calculate the local Reynolds number, Re_{eff} , using V_{eff}
6. Determine α_{eff} and d from values of l , Re_{eff} , V_{eff} and airfoil experimental/Xfoil data
7. Set $\alpha_i = \alpha - \alpha_{eff} + \epsilon$ (ϵ is the local geometric twist angle and is defined negative when reducing the angle of attack)
8. Repeat step 3-7 until α_i has converged
9. $D' = d \cdot \cos(\alpha_i) + l \cdot \sin(\alpha_i)$

These steps should be repeated for every strip and the sum of all the strip-drag forces gives the three dimensional wing drag force. This drag force is composed of the profile drag force and the induced drag. The induced drag part is overestimated due to a difference

between the down-wash angle used to calculate the lift and the induced drag, the reason for this is not completely clear but is also mentioned, but not clarified, in reference [15] on page 7-2.

A downside of this method is its inability to calculate beyond the maximum lift coefficient of the airfoil even if this information is available. This issue can be solved when the down-wash angle distribution is known or when it can be calculated from the lift distribution. An added advantage of using the downwash distribution is the fact that the lift estimate, obtained by the vortex lattice method, can be corrected for viscous and thickness effects. Several methods to determine this downwash distribution were tested but the method applied in the lifting line theory was the easiest to implement, fast to calculate and seemed to work very well for all wings (even swept wings). The mathematical procedure is the following. Making the same assumptions as used in the vortex lattice method, one can approximate the lift coefficient of an airfoil by,

$$C_l = C_{l_\alpha}(\alpha_{eff} - \alpha_0) \quad (3.7)$$

Rewriting this provides information about the angle of attack, required for a certain lift coefficient,

$$\alpha_{eff} = \frac{C_l}{C_{l_\alpha}} + \alpha_0 \quad (3.8)$$

This equation can be used in combination with the lift distribution, obtained from the vortex lattice method, to determine the local effective angle of attack. From this effective angle of attack it is easy to obtain the downwash angle using:

$$\alpha_i(y) = \alpha - \alpha_{eff}(y) + \epsilon(y) \quad (3.9)$$

Here α_{eff} is determined with equation 3.8, ϵ is the local twist angle, defined positive in the same direction as the wing angle of attack, α , and y represents the spanwise location on the wing.

The procedure becomes a bit more complicated as the required two dimensional lift coefficient, used to determine the downwash angle, also depends on the downwash angle. This is clearly illustrated in figure 3.7, $l = L' / \cos(\alpha_i)$, however to determine the effective angle of attack the forces must be converted into coefficients.

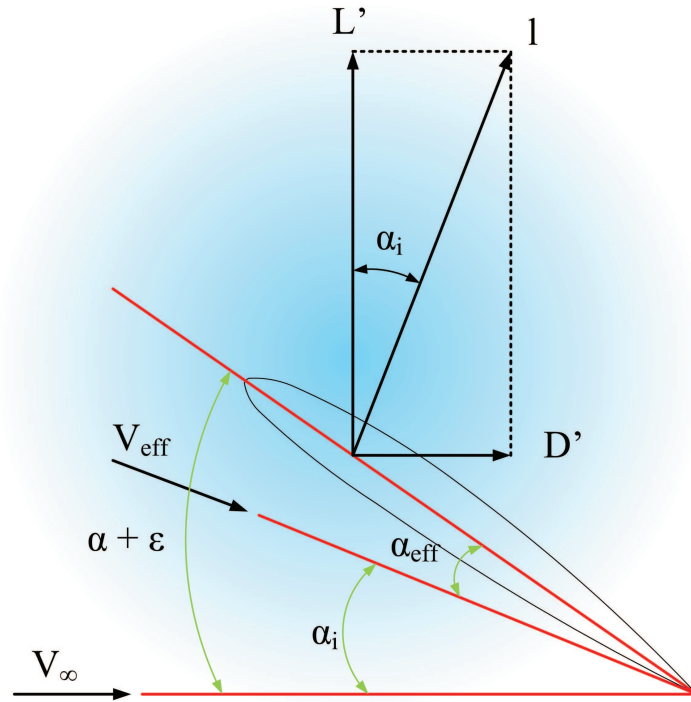


Figure 3.7: Definition of the forces and angles used to determine the inviscid downwash angle.

$$\begin{aligned}
 l &= \frac{L'}{\cos(\alpha_i)} \\
 &\Downarrow \\
 C_l \frac{1}{2} \rho V_{eff}^2 S' &= \frac{C'_L \frac{1}{2} \rho V_\infty^2 S'}{\cos(\alpha_i)} \\
 &\Downarrow \\
 C_l V_{eff}^2 &= \frac{C'_L V_\infty^2}{\cos(\alpha_i)} \\
 &\Downarrow \quad V_{eff} = \frac{V_\infty}{\cos(\alpha_i)} \\
 \frac{C_l}{(\cos(\alpha_i))^2} &= \frac{C'_L}{\cos(\alpha_i)} \\
 &\Downarrow \\
 C_l &= C'_L \cos(\alpha_i) \tag{3.10}
 \end{aligned}$$

Equation 3.10 clearly shows the dependency of C_l on α_i and thus requires a converging iterative loop to uniquely define the effective angle of attack and the the downwash angle. This iterative loop looks like this,

1. Run AVL for the wing at hand and extract the lift coefficient distribution

2. Set $\alpha_i = 0$
3. $C_l = C'_L \cos(\alpha_i)$ (equation 3.10)
4. Determine $\alpha_{eff} = \frac{C_l}{C_{l\alpha}} + \alpha_0$ (equation 3.8)
5. Determine local velocity with $V_{eff} = \frac{V_\infty}{\cos(\alpha_i)}$
6. Set $\alpha_i = \alpha - \alpha_{eff} + \epsilon$
7. Repeat step 3 to 7 until α_i has converged
8. Calculate the local Reynolds number, Re_{eff} , using V_{eff}
9. Determine C_l and C_d from values of α_{eff} , Re_{eff} and airfoil experimental or viscous Xfoil data
10. $L' = \frac{1}{2}C_l\rho V_{eff}^2 S' \cdot \cos(\alpha_i) + \frac{1}{2}C_d\rho V_{eff}^2 S' \cdot \sin(\alpha_i)$
11. $D' = \frac{1}{2}C_d\rho V_{eff}^2 S' \cdot \cos(\alpha_i) + \frac{1}{2}C_l\rho V_{eff}^2 S' \cdot \sin(\alpha_i)$

This procedure is repeated for all strips and the forces are then summed to obtain the wing lift and drag forces and coefficients. The drag estimation incorporates, like in the other method, the profile and induced drag, however the problem with an overestimated induced drag remained. Changes to the method to improve on this induced drag problem will be explained in section 4.2.1.

For low aspect ratio wings an extra drag component is present, the vortex drag. This drag is due to the tip vortex, which for low aspect ratio wings ($A \leq 3.5$), also acts on the wing itself. This is due to the side edge suction force acting in the normal direction, which has components in the lift and drag direction. In reference [17] an equation has been suggested to empirically estimate the vortex drag component:

$$C_{D_v} = K_v \cdot \sin^3(\alpha) \quad (3.11)$$

, in which K_v is the same side edge vortex parameter as in equation 3.1

This results in the following equation for the total wing drag:

$$C_{D_{totw}} = C_{D_{strip}} + K_v \cdot \sin^3(\alpha) \quad (3.12)$$

Assumptions and Capabilities of the Computational Tools

As for most aerodynamic models there are some assumptions in place which restrict the domain of validity of the method. The assumptions and capabilities of the computational tools used are the following:

- AVL:
 - 3 dimensional

- Incompressible (possible to use Prantl-Glauert correction), inviscid, irrotational flow
- Infinitely thin wing
- Small angle of attack approximation
- Xfoil:
 - 2 dimensional
 - Incompressible (Karman-Tsien compressibility correction implemented), irrotational flow
 - Viscous (fully-coupled viscous/inviscid interaction method, e^n transition criterion)
 - Airfoil with thickness
- New method under consideration in this report, quasi-3D method:
 - Quasi three dimensional
 - Incompressible, irrotational flow
 - Viscous
 - Wing with thickness

Airfoil Drag¹

Low Reynolds number (< 1 million) airfoil design is dominated by minimizing the transitional separation bubble losses, which can cause up to 50% more drag. To be able to minimize these losses one must know what the nature of this transitional bubble is.

The bubble is a product of a very stable laminar boundary layer caused by the low Reynolds numbers. The laminar boundary layer is so stable that, even after it separates from the airfoil surface, it takes some time to lose its stability and turn turbulent. The bubble is thus a sequence of events starting with the separation of the laminar boundary layer. This laminar boundary layer rapidly loses stability, turns unstable and transitions some time after separation. After the transition the boundary layer is turbulent and able to reattach. This is clearly illustrated in figure 3.8.

An interesting question at this point is how this separation bubble is able to cause drag, and how can it be minimized? There are two explanations for the same drag increase. The first takes a look at the pressure distribution over the bubble while the second one focuses on the flow itself.

The transitional separation bubble contributes to the profile drag due to its position and shape. The bubble is always located at the beginning of the pressure recovery region which is on the aft facing part of the airfoil. Due to its convex shape, a low pressure is established over the bubble. Having this low pressure perpendicular to an aft facing surface means that the component of the resulting force pulling back on the airfoil, is larger. Figure 3.9 provides a graphical presentation of this. The large pressure arrows, in

¹This section is mainly based on information found in reference [12] and [8]

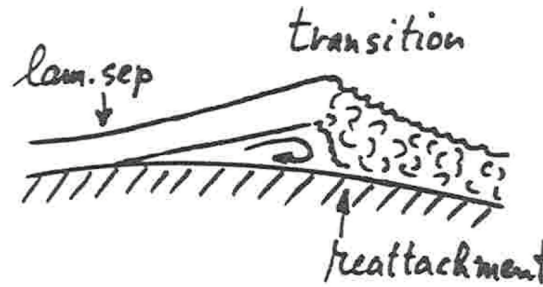


Figure 3.8: Illustration of a laminar separation bubble on an airfoil (picture extracted from ref. [7] page 74).

the red circle, represent the case where the airfoil is experiencing a Reynolds number of 500000 with a bubble present. The small arrows are the pressure arrows on the surface of the same airfoil but at a Reynolds number of 3000000 (no bubble present). It is obvious that the aft pointing component is larger for the larger arrows. Thus there is a stronger aft pulling force on the airfoil in the lower Reynolds number case.

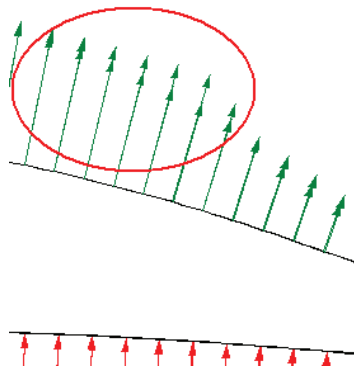


Figure 3.9: Pressure arrows for an airfoil at $Re = 3000000$ (no bubble) and for $Re = 500000$ (bubble present).

² The second explanation is more mathematically based and takes a look at what happens inside the bubble. The drag which one wants to minimize during airfoil design is profile drag. The profile drag is equal to the boundary layer momentum loss, $\rho u_e^2 \theta$, far behind the airfoil. The von Kármán integral momentum equation represents the streamwise development of $\rho u_e^2 \theta$ in the boundary layer.

$$\frac{1}{\rho u_e^2 \theta} \frac{d(\rho u_e^2 \theta)}{d\xi} = \frac{C_f}{2\theta} - \frac{H}{u_e} \frac{du_e}{d\xi} \quad (3.13)$$

²This information was found in reference [12] but is repeated in this report for completeness and clarity reasons

This equation shows that pressure recovery in a separated flow has a strong negative effect on the drag, due to the large shape factor (in separated flow $H > 10$). Both terms on the right hand side of the equation are positive in the pressure recovery region ($\frac{du_e}{d\xi} < 0$). This means that the change in the momentum loss must also be positive due to the fact that the term $\frac{1}{\rho u_e^2 \theta}$ is positive. A small change in the velocity will be amplified by the large shape factor which results in a large jump in the momentum losses. This is clearly shown in figure 3.10. It can be seen from this figure that the edge velocity and the momentum loss gradients at the transition-reattachment region are so steep that one can consider the changes as discontinuous jumps. Integrating the von Kármán equation over the transition-reattachment region becomes possible if the skin friction term is neglected, and this is permitted in the separation bubble. This then results in the following relation between the u_e and $\rho u_e^2 \theta$ jumps:

$$\frac{\Delta(\rho u_e^2 \theta)}{\rho u_e^2 \theta} = -H \frac{\Delta u_e}{u_e} \quad (3.14)$$

,with the values of $\rho u_e^2 \theta$, u_e and H averaged over the transition-reattachment region. Equation 3.14 can be rewritten as a function of the absolute jumps in u_e and $\rho u_e^2 \theta$:

$$a(\rho u_e^2 \theta) = -\rho u_e \delta^* \Delta u_e \quad (3.15)$$

In this equation a is a amplification factor, and $\delta^* = H \cdot \theta$.

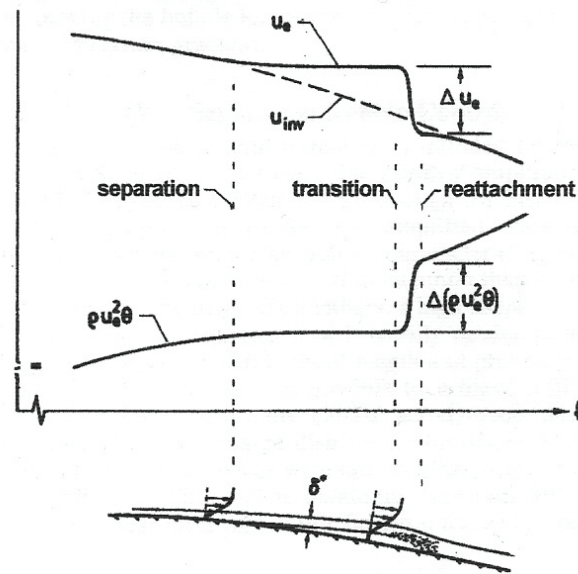


Figure 3.10: Edge velocity and momentum loss jumps at reattachment (figure copied from ref. [12] page 725).

This equation provides a handle to minimize the drag caused by a separation bubble. The increase in drag, $A(\rho u_e^2 \theta)$, over the turbulent reattachment region is thus proportional to the average mass defect, $\rho u_e \delta^*$, and the edge velocity jump, Δu_e . So keeping the mass defect small means that the loss is small. This can be achieved by keeping the distance,

at the transition position, between the free shear layer and the wall as small as possible, because the stagnant fluid under the shear layer must mix out with the turbulent boundary layer for reattachment to occur. This mixing is also the physical mechanism that converts the work done by the airfoil on the airflow, via the bubble pressure drag, into heat. The total drag increase, due to the presence of the transitional separation bubble on the airfoil, will likely be larger than the bubble momentum loss jump. This is due to the momentum loss jump being invariably amplified by the airfoil's pressure recovery region.

To keep the drag as low as possible one has to minimize the distance between the free shear layer and the wall at the transition point. But how can this be controlled? The answer can be found in the positioning of the transition point. Forcing the location of the transition farther upstream, by destabilizing the laminar boundary layer at the leading edge, makes the bubble shorter and the momentum loss lower. This destabilizing can be done by inducing an adverse pressure gradient close to the leading edge of the airfoil (see figure 3.11). But one has to be careful not to eliminate the complete bubble by positioning the transition point in front of the bubble because this would increase the drag again (see figure 3.12). This increase in drag is invoked by the higher friction drag generated by the turbulent boundary layer. Finding the optimal location of the transition point is very important, this location is mostly just aft of the laminar separation point. The optimal location also changes with the angle of attack. The goal of low drag airfoil design is thus: *Obtain transition as close as possible to that optimum point over as much of the operational range, of the airfoil, as possible.*

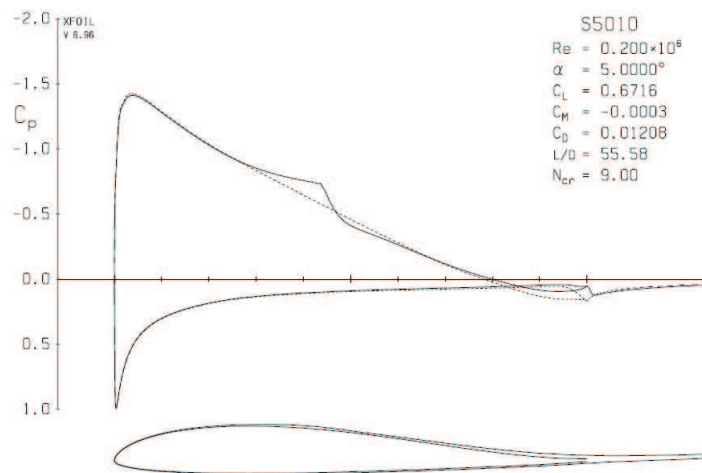


Figure 3.11: Illustration of a typical pressure gradient for Low Reynolds number airfoils.

Apart from the aerodynamic considerations, which for low Reynolds numbers lead to very thin airfoils, one always has to keep in mind that the airfoils have to provide space in the wing to locate the structure.

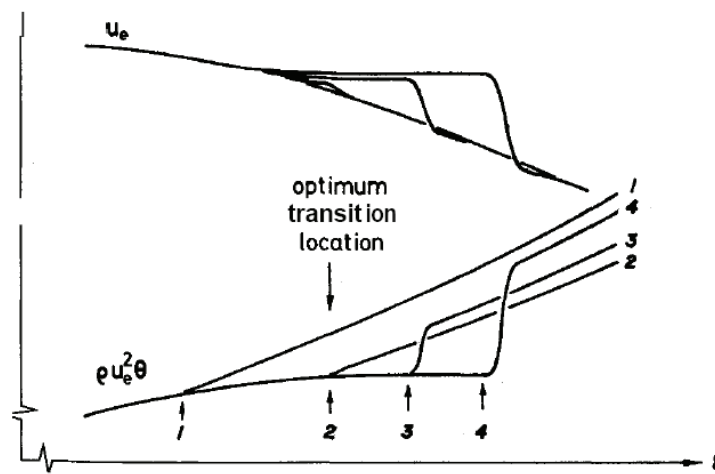


Figure 3.12: Effect of the transition location on bubble size and momentum loss (figure copied from ref. [12] page 726).

Fuselage Drag

The fuselage can be approximated by a streamlined body of revolution. A procedure for calculating the minimum fuselage drag coefficient can be found in reference [15], further referred to as the Hoerner method.

The first step in this procedure is to determine the fuselage thickness ratio, $\frac{l^*}{d^*}$, in which d^* is the fuselage maximum diameter and l^* is the fuselage length. If the fuselage has a rectangular or oval shape an equivalent thickness ratio can be defined using:

$$\frac{l^*}{d_{eq}^*} = 2 \cdot \frac{l^*}{b^* + h^*} \quad (3.16)$$

,in which b^* is the width and h^* the height of the shape at the largest cross-section. This thickness ratio can then be used in equation 3.17 to determine the minimum drag coefficient of the body.

$$\frac{C_{D_{fus}}}{C_{f_{fus}}} = 1 + 1.5 \cdot \left(\frac{d^*}{l^*}\right)^{3/2} + 7 \cdot \left(\frac{d^*}{l^*}\right)^3 \quad (3.17)$$

This equation is empirically developed and is presented in reference [15] by S.F. Hoerner. The only variable remaining to be determined in equation 3.17, is the friction coefficient. As stated on page 2-7 of reference [15], it is possible to use the friction drag coefficient for an equivalent flat plate (plane surface with the same Reynolds number). In figure 3.13 the friction drag coefficient is plotted against the Reynolds number for experiments and approximation methods. One approximation method for laminar flow and several for turbulent flow are given in reference [15].

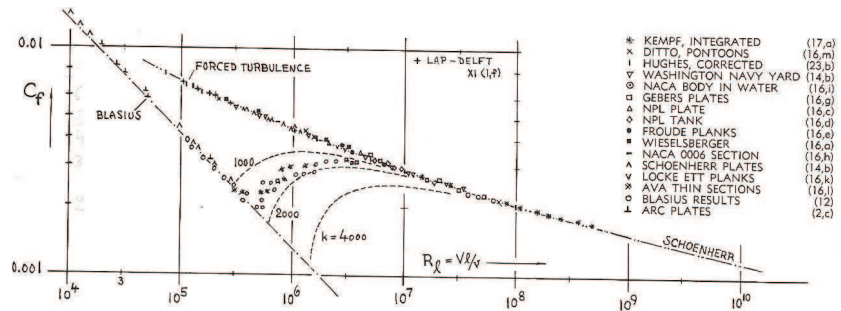


Figure 3.13: Friction drag coefficient for plane surfaces plotted against the Reynolds number (page 2-6 reference [15]).

The laminar friction drag coefficient can be calculated using:

$$C_{f_{lam}} = \frac{1.328}{(Re_{fus})^{1/2}} \quad (3.18)$$

while the turbulent one is calculated using:

$$C_{f_{turb}} = \frac{0.427}{(\log(Re_{fus}) - 0.407)^{2.64}} \quad (3.19)$$

In these equations it is important to get the right value for the Reynolds number. However in some mini-UAV's the propeller is in front of the fuselage increasing the velocity and thus the Reynolds number over it. To calculate this increase in the velocity it is necessary to resort to propulsion theory which states that the propulsive efficiency is relate to the difference between the velocity at infinity and the velocity behind the propeller. This can be seen in:

$$\eta_j = \frac{2}{2 + \frac{\Delta V}{V_\infty}} \quad (3.20)$$

Rewriting this provides the velocity increase,

$$\Delta V = \left(\frac{2}{\eta_j} - 2 \right) \cdot V_\infty \quad (3.21)$$

Based on a given propulsive efficiency, the Reynolds number corresponding to the fuselage can be calculated,

$$Re_{fus} = \frac{l^* \cdot (V_\infty + \Delta V)}{\nu} \quad (3.22)$$

,and used in equation 3.18 and 3.19.

The total friction drag of a body is then determined using a linear function between both friction coefficients with the location of the transition point, x_{tr} , as its variable.

$$C_f = C_{f_{lam}} \cdot \left(\frac{x_{tr}}{l^*} \right) + C_{f_{turb}} \cdot \left(1 - \frac{x_{tr}}{l^*} \right) \quad (3.23)$$

To use this equation x_{tr} must be provided by the user. An educated guess will probably provide a sufficiently accurate result. The real location of the transition point strongly depends on the shape and thus the pressure distribution over the fuselage. Combining the result for the friction coefficient with equation 3.17 gives an estimate for the fuselage drag coefficient.

The best method for the determination of the turbulent flow friction coefficient was selected based on comparison with measurements given in reference [32]. This comparison can be seen in table 3.1. Most micro aerial vehicles have fuselages with a thickness ratio between 5 and 8, and have a Reynolds number between $4 \cdot 10^5$ and $1.5 \cdot 10^6$. These Reynolds numbers take into account that a propeller might increase the velocity over the fuselage.

In table 3.1 one can clearly see that the calculation method developed by Young in reference [32] works extremely well. The Hoerner method³ shows larger differences, but when looking at cases with lower Reynolds numbers ($< 2 \cdot 10^6$), it is clear that this method performs equally good or even better (see the case for $Re = 1173000$). The Young method is overall better but is computationally much more complicated as it requires the pressure distribution over a body of revolution. This method might be an interesting topic to look at in the future.

³Hoerner provides two equations (see reference [15]), one calculates the drag coefficient based on the fuselage wetted area and the other on the largest cross-section. The equation used in this report is based on the largest cross section. Comparison in table 3.1 is based on the wetted area equation as the data from literature was only available for drag coefficients based on the wetted area. However both equations presented by Hoerner are expected to have the same accuracy.

Table 3.1: Comparison between calculated and experimental drag coefficients for streamlined bodies of revolution (drag coefficients are based on the fuselage wetted area).

Re	$\frac{l^*}{d^*}$	$\frac{x_{tr}}{l^*}$	C_D measured	C_D Young	Young -error [%]	C_D Hoerner	Hoerner -error [%]
840000	4.95	0.1	0.0053	0.0053	0	0.005225	-1.41
1173000	6.67	0.1	0.0045	0.0047	4.44	0.004525	0.57
1260000	5.49	0	0.005	0.005	0	0.005014	0.29
1580000	5.43	0	0.0045	0.0048	6.67	0.004807	6.81
1580000	3.00	0	0.006	0.0062	3.33	0.006398	6.63
2040000	5	0.6	0.0022	0.00236	7.27	0.002537	15.32
3060000	5	0.52	0.0022	0.00244	10.91	0.00255	15.89
2090000	5	0.22	0.00435	0.00409	-5.98	0.003876	-10.90
3130000	5	0.17	0.00415	0.00388	-6.51	0.003733	-10.05
2070000	5	0.33	0.00364	0.00361	-0.82	0.003491	-4.1
3110000	5	0.28	0.00359	0.00351	-2.23	0.003361	-6.38
2050000	5	0.15	0.0044	0.00437	-0.68	0.004142	-5.87
3070000	5	0.1	0.00421	0.00414	-1.66	0.003987	-5.29
11610000	5.88	0.065	0.0028	0.003	7.14	0.003079	9.98
3160000	3.00	0	0.005	0.0052	4	0.005597	11.94
3160000	3.00	0.04	0.0052	0.0051	-1.92	0.005419	4.21

The fuselage drag coefficient uses the largest cross-sectional area of the fuselage as a reference area, but when used to compute the aircraft drag coefficient this must be with respect to the wing area. This conversion is simple and can be done using the following equation:

$$C'_{D_{fus}} = C_{D_{fus}} \cdot \frac{S_{fus}}{S_{ref}} \quad (3.24)$$

Interference Drag

Interference drag is the drag that arises when two solid bodies touch each other or when they are positioned very close to each other such that their boundary layers interfere. This drag can thus be seen as the difference between the total drag of the configuration and the sum of the drags of the separate components constituting the configuration. It is hard to calculate these effects but they do depend on the configuration and the position of the components and might thus have a significant effect on the optimization. In reference [15] an extensive discussion is presented on this topic but little tools are presented that estimate the effects, the ones presented are only proven for higher Reynolds numbers. However in this section the same tools will be used and it is assumed that they apply on the flow regime under consideration.

The first thing to do is to figure out which components have influence on each other. For flying wings, these are the wing and the fuselage and secondly the vertical tail and the

fuselage. Interference drag exists of two components, the parasitic interference, which is caused by interaction of the boundary layers at $C_L = 0$, and the induced interference drag, due to changes in the lift.

The *parasitic interference drag* is plotted in figure 3.14 for different longitudinal locations of the wing on the fuselage. It can be seen that there is an increase in drag and that it changes for different locations of the wing, however the wing location will be determined by the stability margin. This will not be a variable for the optimization, but rather a given increase in the drag. This effect is however reduced as the wing and the fuselage both loose wetted area, and thus friction drag, when put together. This is the reason for assuming that when the wing and fuselage are joined, both effects cancel each other.

However when looking at the vertical tail, this does not lose wetted area and as this surface does not provide side forces in straight horizontal flight parasitic interference drag will be the only form of interference drag acting on it. From figure 3.14 C_{D_e} for the vertical tail is taken equal to 0.0015, it can be seen that the effect is small for wings located aft on the fuselage. To convert this drag coefficient to the wing area one can use the following formula

$$C_{D_{int_{tail}}} = C_{D_e} \cdot \frac{c^2}{S_{ref}} \quad (3.25)$$

,in which c is the root chord length of the vertical tail.

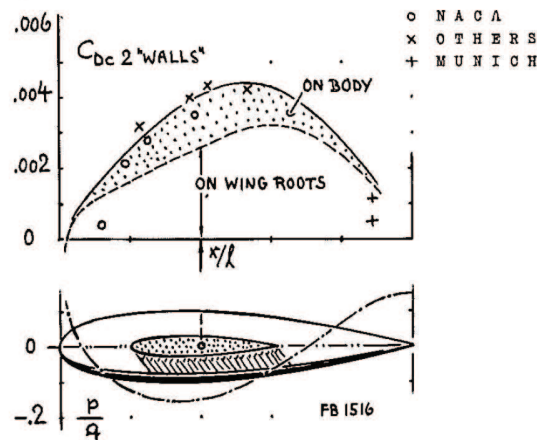


Figure 3.14: Parasitic interference drag in the corner between a wing and a fuselage for different longitudinal locations of the wing/vertical tail (page 8-15 reference [15]).

The *induced interference drag* is caused by changes in the lift distribution on the wing due to the presence of the fuselage. Reference [15] explains this in great detail. In this report the focus will be on the parts coming into play for mini-UAV's.

The presence of the fuselage at lift coefficients different from zero causes an increase in the angle of attack at the roots of the wing, this is referred to as alpha-flow. At the same time a part of the circulation of the wing roots is transferred to the fuselage and the fuselage itself also generates lift due to separation at the rear of the body. These effects might increase the lift curve slope and thus cause an increase in drag due to lift. These effects

are however hard to predict and for cruise the body will be attached to the wing at an incidence such that it has a zero angle of attack avoiding this kind of interference drag.

A second effect is that the body displacement causes the average velocity at the wing root to increase. For a low wing configuration this increases the velocity on the upper surface of the wing while in a high wing configuration this will be on the lower surface. This has its effect on the lift which will be higher in the low wing configuration and lower in the high wing configuration. For a fuselage with a diameter equal to 10% of the span this effect is in the order of $C_{L_{b1}} = +0.1$ for a low wing configuration and $C_{L_{b1}} = -0.1$ for high wing configurations. This $C_{L_{b1}}$ is based on the wing area covered by the fuselage width. This means that the effect has to be converted to the reference area using:

$$\Delta C_L = \Delta C_{L_{b1}} \cdot \frac{S_{covered}}{S_{ref}} \quad (3.26)$$

A linear variation of $C_{L_{b1}}$ will be applied for wings with a vertical location different from the high or low wing configuration, and for small changes in percentages of d^*/b .

The incidence angle of the wing with respect to the fuselage has also its effect on the lift and thus on the induced interference drag. This effect is best described with equation 3.27.

$$\Delta C_{L_{b2}} = -0.07 \cdot \alpha_{inc} \quad (3.27)$$

In this equation $\Delta\alpha$ represents the incidence angle, which is defined as the angle between the wings zero lift line and the fuselage axis (in degrees). Equation 3.28 gives a relation between the changes in the lift coefficient and the interference drag.

$$C_{D_b} = 0.035 \cdot (\Delta C_{L_b})^2 \quad (3.28)$$

In which $\Delta C_{L_b} = \Delta C_{L_{b1}} + \Delta C_{L_{b2}}$ represents the total change in lift coefficient due to interaction between the fuselage and the wing. This drag coefficient is, once again related to the covered wing area and can be converted to the reference area using equation 3.29.

$$\Delta C_D = C_{D_b} \cdot \frac{S_{covered}}{S_{ref}} \quad (3.29)$$

The previously mentioned changes in the lift coefficient will also be taken into account for the lift but were not discussed in chapter 3.1.1 because of there strong relation to the interference drag.

3.1.3 Stability

The way of treating stability for a mini-UAV is no different from large aircraft. The autopilot in mini-UAV's could provide active stability but the autopilots developed in the MAVlab work better with a inherently stable aircraft. Having an unstable aircraft would also require a high frequency of control surface deflections which stresses the servos, this in turn shortens their life span and consumes a lot of useful energy.

The focus of this section will be on the pitch stability, as this is critical for tailless aircraft configurations. The directional stability will be treated by giving an estimate for the vertical tail size. Sweep, which is required for trimming the aircraft as will be explained later in this section, will also increase the directional stability. Roll stability will be omitted as experience showed that the roll controllability is very high for mini-UAV's and can thus be easily compensated for by the autopilot.

Dynamic stability is hard to determine as the values for the stability derivatives are badly estimated using the vortex lattice method, AVL. A better way to approach this problem is to optimize the design and determine these values in a wind tunnel or with advanced CFD-methods and then make small changes to the design to ensure dynamic stability.

Pitch Stability

The static longitudinal stability is determined by the stability margin. This margin is defined by the difference between the aircraft neutral point and the location of the center of gravity. For a tailless aircraft this simplifies to the location of the wing aerodynamic center with respect to the aircrafts center of gravity. Equation 3.30 provides a mathematical description of this stability margin.

$$\sigma = \frac{x_n - x_{cg}}{c_{ref}} \quad (3.30)$$

In this equation the location of the center of gravity, x_{cg} , is determined by the location of the components inside the aircraft. When the stability margin is positive, the aircraft will be stable. The aircraft is neutrally stable when the location of the center of gravity is the same as the neutral point, which explains its name. A negative value results in an unstable aircraft. The reference chord length is taken equal to the wing mean aerodynamic chord, and can be calculated with,

$$c_{mac} = \frac{2}{S_{ref}} \int_0^{b/2} c^2(y) dy \quad (3.31)$$

, in which $c(y)$ represents the chord length at spanwise location y .

The only remaining value to be determined in equation 3.30 is the location of the neutral point. The neutral point stick fixed, is in essence the same as the aerodynamic center of a complete aircraft. The definition of this neutral point is the following:

The longitudinal location, when taken as the reference point⁴ through which the aerodynamic forces act, in which the pitching moment of the complete aircraft is independent of the angle of attack.

For a tailless aircraft configuration the determination of the neutral point location is the same problem as determining the aerodynamic center of the wing (when the fuselage influence is assumed to be small). Two methods to determine this aerodynamic center were tested and compared to experimental results. A first method is purely based on the geometry of the wing and was obtained from reference [21].

$$x_{ac} = c_{mac} \cdot \frac{A}{6} \frac{1 + 2 \cdot \lambda}{1 + \lambda} \cdot \tan(\Lambda_{0.25}) + \frac{c_{root}}{4} \quad (3.32)$$

A second method was also obtained from reference [21], and this one uses aerodynamic coefficients to determine the aerodynamic center. When assuming that the aerodynamic center is located in the plane of the wing, then one can write the pitching moment around the wing origin (leading edge of the wing root) as:

$$C_{M_{origin}} = C_{M_{acw}} - (C_L \cdot \cos(\alpha) + C_D \cdot \sin(\alpha)) \cdot \frac{x_{ac}}{c_{ref}} \quad (3.33)$$

Rewriting equation 3.33 by ignoring the drag effects and assuming small angles of attack gives:

$$C_{M_{origin}} = C_{M_{acw}} - C_L \cdot \frac{x_{ac}}{c_{ref}} \quad (3.34)$$

Differentiating this equation with respect to the angle of attack results in,

$$C_{M_{origin\alpha}} = 0 - C_{L\alpha} \cdot \frac{x_{ac}}{c_{ref}} \quad (3.35)$$

, which can then be written as

$$x_{ac} = -c_{ref} \cdot \frac{C_{M_{origin\alpha}}}{C_{L\alpha}} \quad (3.36)$$

, in which c_{ref} is equal to c_{mac} . The values of $C_{M_{origin\alpha}}$ and $C_{L\alpha}$ can be found using AVL.

To validate these methods, a comparison between calculated aerodynamic center and experimentally determined aerodynamic center is represented in table 3.2. The data in this table was obtained from reference [21] and [5]. Reference [21], referred to as Phillips in table 3.2, used CFD data combined with equation 3.36 to determine the aerodynamic center, while the data from reference [5], referred to as NACA in table 3.2, was obtained from wind tunnel measurements.

The NACA wings all have the same cambered airfoils and varying sweep and twist. The two numbers following the 24 define the sweep angle in degrees and the last two define

⁴Remember that the real point through which the aerodynamic forces act, is the point where there is no aerodynamic moment. This point is known as the center of pressure which changes location with the angle of attack

Table 3.2: Comparison between experiments/CFD and the calculated aerodynamic center using equation 3.32 and 3.36.

	x_{ac} exp/CFD	x_{ac} mth 1	Δ mth 1 [%]	$\Delta\sigma$ [%]	x_{ac} mth 2	Δ mth 2 [%]	$\Delta\sigma$ [%]	c_{mac}	x_{cg}
NACA240000	0.127	0.136	6.91	2.07	0.132	3.77	1.13	0.423	0.106
NACA241500	0.280	0.287	2.71	1.79	0.278	-0.46	-0.31	0.423	0.259
NACA243000	0.452	0.462	2.14	2.29	0.454	0.46	0.50	0.423	0.431
NACA243085	0.457	0.462	1.13	1.22	0.454	-0.53	-0.57	0.423	0.436
Phillips SW=5	0.183	0.186	1.47	0.63	0.179	-2.02	-0.87	0.423	0.162
Phillips SW=10	0.231	0.236	2.07	1.13	0.228	-1.39	-0.76	0.423	0.21
Phillips SW=15	0.280	0.287	2.49	1.65	0.278	-0.68	-0.45	0.423	0.259
Phillips SW=20	0.332	0.342	2.95	2.31	0.332	0.18	0.14	0.423	0.310
Phillips SW=30	0.441	0.462	4.69	4.88	0.454	2.97	3.09	0.423	0.420
Phillips SW=40	0.570	0.610	7.05	9.49	0.607	6.64	8.93	0.423	0.548
Phillips SW=50	0.731	0.809	10.70	18.47	0.816	11.71	20.22	0.423	0.709

the washout angle (twist) of the wing, e.g. NACA243085 has 30° quarter chord sweep and -8.5° twist. The wings from reference [21] are designated Phillips (after the author) with the quarter chord sweep angle behind it. These wings did not have any twist and symmetric airfoils were assumed. From the comparisons it is clear that the second method (eq. 3.36) is better in estimating the location of the aerodynamic center than the first method (eq. 3.32), except for the 50° sweep angle. When compared to the experimental results, the error is around $\pm 0.5\%$ for swept wings while for unswept wings the estimate has an error of 3.8%. The larger error when compared to the Phillips wings with higher sweep angles are probably due to errors in the CFD calculation because when comparing the 30° sweep from the NACA report it appears to work fine. Another cause might be the assumed symmetric airfoil, however this is unlikely to be the problem as airfoils should only have a minor influence on the location of the aerodynamic center.

For the stability of flying wings it is important to validate the impact of this error on the stability margin. That is why a $\Delta\sigma$ was presented in table 3.2, the calculation of this value is the following.

$$\Delta\sigma = \frac{x_{ac_{computed}} - x_{cg}}{c_{mac}} - 0.05 \quad (3.37)$$

Assuming an original stability margin of 5%, relative to the experimental/CFD aerodynamic center, and having the mean aerodynamic chord gives the location of the center of gravity, x_{cg} , by rewriting equation 3.30. This value of x_{cg} is then used to determine the stability margin with respect to the calculated aerodynamic center. The difference between the calculated stability margin and the original stability margin (= 5%) is represented in the table.

It is clear from table 3.2 that this error is quite high for the first method but is acceptably low for the second method. The first method also has the tendency to always overestimate the stability margin, while this is not the case for the second method. The positive values of $\Delta\sigma$ represent overestimations of the stability and are thus relatively dangerous as they can cause instability in the airplane while on paper everything looks stable. The second method seems to provide no unstable aircraft as long as the design stability margin is

higher than 2% and when the sweep angle is lower or equal to 30° . The experiments show no problems up to 30° while for the CFD problems start at this sweep angle, but as mentioned before this might be due to calculation problems in CFD or an error in the assumed airfoil. From this discussion it is clear that equation 3.36 is the one that will be used for estimating the aerodynamic center and thus the neutral point location of the tailless aircraft configuration.

Trimmed Flight at the Cruise Speed

Trimming an aircraft is to ensure that the aircraft flies level at the desired speed, the cruise speed. This speed is determined by the design lift coefficient, corresponding to $(L/D)_{max}$, when considering straight horizontal flight. The trick about trimming the aircraft is quite simple, get the right amount of aerodynamic moment to ensure that it cancels the weight induced moment around the aerodynamic center. A very clear visual presentation of this is given in figure 3.15. For our purpose the thrust is assumed to be in line with the center of gravity and is conveniently left out of the picture. Mathematically this translate into:

$$M - W \cdot (x_{ac} - x_{cg}) = 0 \quad (3.38)$$

There are two ways to get this aerodynamic moment right. The first is by simply

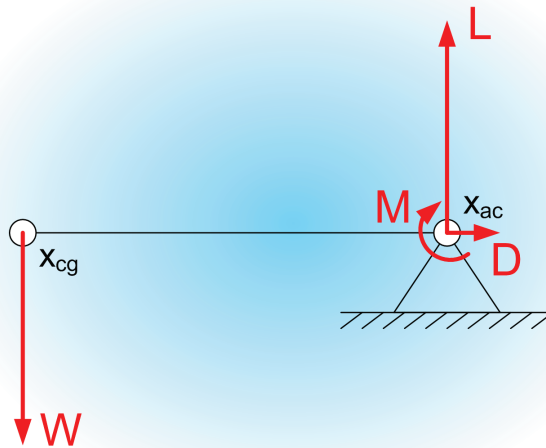


Figure 3.15: Illustration of forces and moments involved in trimming an aircraft (L = lift, D = drag, M = aerodynamic moment, W = aircraft weight).

deflecting the elevator control surfaces, this is a good approach when considering non-cruise phases of flight. The second way is by giving the horizontal tail surface, for normal configurations, a decalage angle. For flying wings one has to distinguish between swept and unswept wings. For swept wings one can change the lift distribution by applying twist (geometric and aerodynamic), while for unswept wings this has no effect as there

is no arm with respect to the aerodynamic center and it is thus obtained by using the appropriate airfoils (with the correct moment coefficient).

However the difficulty lies in getting a good estimate for the moment coefficient around the aerodynamic center. For flying wings this is a bit tricky due to the fact that the moment coefficient of the airfoils have a major impact on the overall moment coefficient around the aerodynamic center, while for a normal configuration this is dominated by the lift forces of main and horizontal tail wing. These large forces are easier to determine accurately.

Trimming a Tailless Aircraft

First one must understand the principles behind trimming a tailless aircraft. In a normal configuration the decalage angle of the horizontal tail is used to balance the moments, however a tailless aircraft is, by definition, lacking a horizontal tail surface. To trim this kind of aircraft one must make a distinction between swept and unswept wings. A zero sweep tailless aircraft, further referred to as flying plank, can not use the lift distribution, and thus not the twist, to change the moment coefficient around the aerodynamic center. It thus requires that the moment coefficient of airfoils is correctly chosen. To obtain a stable aircraft ($\sigma > 0$, center of gravity in front of the wing aerodynamic center) it is necessary to use airfoils with a slightly positive moment coefficient, around its aerodynamic center. Table 3.3 gives a list of low-Reynolds number airfoils for flying planks and their C_{mac} and α_0 . The value of the zero lift angle of attack is of less importance to the flying planks but its importance will become clear for swept flying wings.

Table 3.3: Flying plank airfoils with corresponding moment coefficients and zero lift angles of attack.

Airfoil name	C_{mac}	α_0
<i>HS130</i>	0.0157	-0.09
<i>JWL – 065</i>	0.0298	0.3
<i>CJ – 5</i>	0.02	-0.1
<i>CJ – 3309</i>	0.019	-0.58
<i>CJ – 25²09</i>	0.027	-0.13
<i>EMX – 07</i>	0.021	-0.3
<i>Phönix</i>	0.009	-0.69
<i>HS2.0/8.0</i>	0.012	-0.33

For swept wings the moment coefficient is not only determined by the airfoil moment coefficient but also by the lift distribution. This makes it possible for a swept wing to use aerodynamic and geometric twist to trim the aircraft. A way to understand this better is to make a comparison between a swept wing tailless aircraft and a normal configuration as presented in figure 3.16 from reference [19]. In this figure it is clear how a normal configuration can change into a swept wing tailless aircraft. It also shows that the function of the horizontal tail is now performed by the wingtips, and thus showing the similarities between the decalage angle for a normal configuration and the twist for a swept wing tailless aircraft.

The next step is of course to determine the wing moment coefficient around the aerodynamic center. Once this moment coefficient has been calculated it is possible to determine

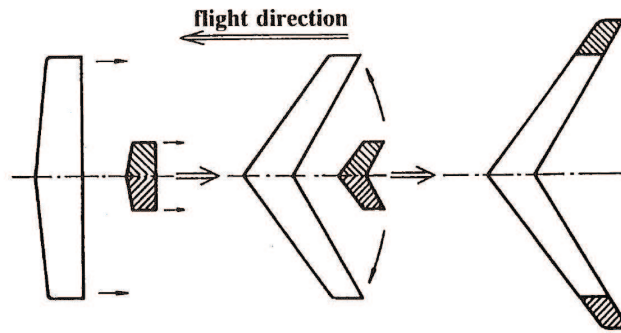


Figure 3.16: Evolution from a normal configuration to a swept tailless aircraft.

the required amount of twist such that the aircraft is trimmed, for a certain stability margin, at the cruise speed without deflecting the elevators.

The method to calculate the wing moment coefficient was developed by the author and a small correction was made from information in reference [10]. From figure 3.17 it can be seen that the moment coefficient consists of two parts: one is due to the integration over the span of C_{mac} and the other one is due to the integration of the lift distribution times its arm to the aerodynamic center over the wing. A strip method will be used to calculate these integrals.

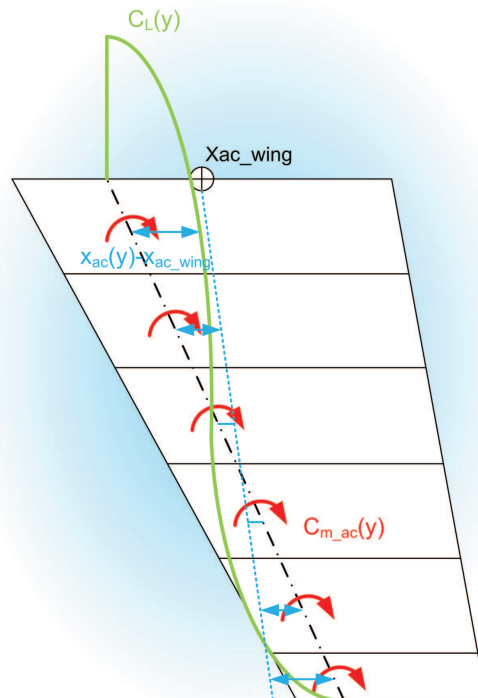


Figure 3.17: Forces and moments contributing to the wing moment coefficient.

Mathematically this looks as follows:

$$C_{M_{ac_w}} = C_{M_1} + C_{M_2} \quad (3.39)$$

, in which

$$C_{M_1} = 2 \cdot f \cdot \sum_{i=1}^N \frac{C_{m_{ac_i}} \cdot c_i \cdot (c_i \cdot \Delta y_i)}{S_{ref} \cdot c_{ref}} \quad (3.40)$$

and

$$C_{M_2} = 2 \cdot \sum_{i=1}^N \frac{C_{L_i} \cdot (c_i \cdot \Delta y_i) \cdot (x_{ac_w} - x_{ac_i})}{S_{ref} \cdot c_{ref}} \quad (3.41)$$

The equations are multiplied by two to obtain the moment for the complete wing, as the equations are developed for half wing span. All subscripts i define the strip number going from 1 to N . In equation 3.40 an empirical correction factor f was used to correct for planform effects (see reference [10]), and can be found using:

$$f = \frac{2 \cdot A}{2 \cdot A + 1} \cdot \cos(\Lambda_{0.5}) \quad (3.42)$$

For this method AVL is used to determine the lift distribution, while Xfoil is used to determine the airfoil average moment coefficient around its aerodynamic center. This averaging is done over the attached flow α -range of the airfoils.

Directional Stability

Directional stability is handled by the vertical tailplane. A simple equation was used to estimate the required vertical tail surface. This equation is often used in the design of RC-planes and has proven to work well.

$$\frac{S_v \cdot (x_{ac_v} - x_{cg})}{S \cdot b} = 0.2 \sim 0.4 \quad (3.43)$$

In this equation x_{ac_v} is the location of the vertical tail aerodynamic center. For more directional stability it is better to be close to 0.4 however 0.3 is usually sufficient.

3.2 Optimization

In this section an introduction will be provided into the algorithm used for the optimization. The algorithm is required to handle non-linear behaviour as the objective and some of the constraints will be non-linear. Based on a comparison between two candidate algorithms one is selected and explained. This is followed by an insight into the variables used for the optimization and the constraints imposed on them. The last part will provide an insight into the different objective functions for range and endurance of electrically powered aircraft.

3.2.1 The Optimization Algorithm

The objective function and some of the constraints applied to the optimization are non-linear and thus require a nonlinear optimization algorithm. Several algorithms are available to tackle these problems. However for this research the two algorithms of interest are the sequential quadratic programming algorithm, and the genetic algorithm. These two options are selected because they exist in Matlab and provide the capability to handle all types of constraints. They are also state of the art algorithms when dealing with complex optimization problems.

Algorithm Selection

The selection is based on their capabilities and limitations in handling the objective function and its constraints. An overview of both algorithms is presented to create a base for the selection process.

- Sequential quadratic programming algorithm
 - Can get stuck in local minima
 - Able to handle strong nonlinear objective functions
 - Efficient use of objective function evaluations
 - Can handle all types of constraints (nonlinear, equality, inequality, bounds)
- Genetic algorithm
 - Unlikely to get stuck in local minima, when the settings for the algorithm are correct
 - Able to handle strong nonlinear objective functions
 - Inefficient use of objective function evaluations
 - Can handle all types of constraints (nonlinear, equality, inequality, bounds)

From this overview it is clear that the differences are in the efficiency of the algorithm and the capability to handle local minima. The conclusion is thus that it is preferred to use the sequential quadratic programming algorithm when it is proven that the objective function together with its constraints, contain no local minima.

For a sequential quadratic program, the necessary and sufficient condition for a nonlinear minimization problem, is that the objective function and the constraints are convex. Determining the convexity of the objective function is impossible, as the objective function for performance optimizations, is dependent on 5 variables and the calculation of the aerodynamic forces is based on a numerical approach. The linear constraints are always convex but the nonlinear constraints are also dependent on the aerodynamic calculations imposing the same problem as for the objective function. The conclusion of this is that the use of sequential quadratic programming is not guaranteed to find a global minimum. However the efficiency of this algorithm is much larger and is thus preferred. One way of testing if it could still be used is by applying it with different initial points and then determining if it always finds the same result. Another option is using the genetic algorithm to find a global optimum and then verifying if the sequential quadratic programming algorithm results in the same solution to the problem.

Sequential Quadratic Programming

The sequential quadratic programming algorithm exists of two steps in which a quasi-Newton method and a line search are used iteratively to find the best possible solution. The quasi-Newton method is used to locally, around the current location, approximate the real problem with a quadratic function. The line connecting the solution to this quadratic problem and the current location, is then used to determine the new-current location, and is referred to as the line search.

Karush-Khun-Tucker Equations

The Karush-Khun-Tucker (KKT) equations are used to formulate the necessary conditions for a general constraint optimization problem. These conditions are also sufficient conditions if the objective function and the constraint functions are convex. A general optimization problem,

$$\min_{\mathbf{x}} f(\mathbf{x}) \quad (3.44)$$

subject to,

$$\begin{aligned} G_i(\mathbf{x}) &= 0, & i &= 1, \dots, m_e \\ G_i(\mathbf{x}) &\leq 0, & i &= m_e + 1, \dots, m \end{aligned}$$

is converted into the KKT equations,

$$\begin{aligned} \nabla f(\mathbf{x}^*) + \sum_{i=1}^m \lambda_i \cdot \nabla G_i(\mathbf{x}^*) &= 0 \\ \lambda_i \cdot G_i(\mathbf{x}^*) &= 0, & i &= 1, \dots, m \\ \lambda_i &\geq 0, & i &= m_e + 1, \dots, m \end{aligned}$$

these constraints are in addition to the original constraints. In these equations $f(\mathbf{x}) : \mathbb{R}^n \rightarrow \mathbb{R}$ represents the objective function, $G(\mathbf{x}) : \mathbb{R}^n \rightarrow \mathbb{R}$ the constraint equations and \mathbf{x}^* represents the solution to the minimization problem. The first equation of the KKT-equations represents the canceling of the gradients when $\mathbf{x} = \mathbf{x}^*$. The λ 's represent

the Lagrange multipliers which are used to scale the gradients of the constraints such that they balance with the objective gradients. The last two equations implicitly ensure that only the active constraints are included by setting the Lagrange multipliers of non-active constraints equal to 0. Further details about the Karush-Kuhn-Tucker conditions can be found in [18] and [1].

Quadratic Programming Subproblem

The first part of the sequential quadratic programming problem is solving the quadratic programming subproblem. This subproblem forms the basis for the approximation of the Lagrangian function that looks like equation 3.45 when formulated for the general problem (equation 3.44).

$$L(\mathbf{x}, \lambda) = f(\mathbf{x}) + \sum_{i=1}^m \lambda_i G_i(\mathbf{x}) \quad (3.45)$$

Truncating the Taylor series after the second derivative will serve as the approximating quadratic function while the nonlinear constraints are linearized. After some simplifications the following quadratic minimization problem arises,

$$\min_{\mathbf{d} \in \mathbb{R}^n} \frac{1}{2} \mathbf{d}^T \mathbf{H}_k \mathbf{d} + \nabla f(\mathbf{x}_k)^T \mathbf{d} \quad (3.46)$$

$$\begin{aligned} \nabla G_i(\mathbf{x}_k)^T \mathbf{d} + G_i(\mathbf{x}_k) &= 0, & i = 1, \dots, m_e \\ \nabla G_i(\mathbf{x}_k)^T \mathbf{d} + G_i(\mathbf{x}_k) &\leq 0, & i = m_e + 1, \dots, m \end{aligned}$$

In these equations the \mathbf{d} represents the difference between the current location (subscript k) and the solution to the quadratic subproblem. The \mathbf{H}_k represents the Hessian approximation of the Lagrangian. The approximation of this Hessian is obtained with a quasi-Newtonian approach, namely with the BFGS (Broyden, Fletcher, Goldfarb, Shanno) method. Further details are not provided but can be found in literature [18],[24] and from reference [1].

Line Search

The solution, \mathbf{d}_k , of the above mentioned quadratic subproblem provides a direction for the line search which will provide a new current location. In equation 3.47 one can see a linear function with a single variable ξ , which is changed such that the required decrease in the merit function 3.48 is obtained.

$$\mathbf{x}_{k+1} = \mathbf{x}_k + \xi \mathbf{d}_k \quad (3.47)$$

$$\psi(\mathbf{x}) = f(\mathbf{x}) + \sum_{i=1}^{m_e} r_i \cdot g_i(\mathbf{x}) + \sum_{i=m_e+1}^m r_i \cdot \max[0, g_i(\mathbf{x})] \quad (3.48)$$

In which r_i is a penalty parameter defined as,

$$\begin{aligned} r_i = (r_{k+1})_i &= \max_i \left\{ \lambda_i, \frac{(r_k)_i + \lambda_i}{2} \right\}, & i = 1, \dots, m, \quad k > 1 \\ r_i &= \frac{\|\nabla f(\mathbf{x})\|}{\|\nabla g(\mathbf{x})\|}, & i = 1, \dots, m, \quad k = 1 \end{aligned}$$

In this last equation $\| \cdot \|$ represents the Euclidean norm.

3.2.2 Variables and Constraints

One of the first steps in setting up an optimization tool is to determine the variables. For the problem at hand two sets of variables are needed, geometric variables which define the wing geometry and variables that define the flow around the aircraft, like there are the velocity and the altitude. After the definition of the variables it is important to recognize and define the linear and non-linear constraints.

Variables

As already mentioned, there are two sets of variables. The first set, the geometric variables, is used to unambiguously define the wing geometry. The approach will be to use multiple linear wing sections. This is the same convention as used in AVL and makes it possible to define the geometry with a limited amount of variables. The assumption is made that the wing is symmetric with respect to the aircraft longitudinal plane, and the variables thus define one side of the wing while the other side is mirrored. The variables to define a trapezoidal wing section are:

- Section span, $\frac{b}{2}$
- Root chord, c_{root}
- Quarter chord sweep, $\Lambda_{0.25}$
- Taper ratio, λ

In this list the twist is missing, this is because of the fact that this variable depends on all other variables. The twist for a tailless aircraft is varied such that the wing generates the required amount of moment around the aerodynamic center to trim the aircraft at its design lift coefficient. When defining multiple wing sections these variables become vectors. A more detailed insight into these variables will be provided in section 4.1.1. Up until this point one variable has not been discussed, namely the airfoil. At each wing section an airfoil has to be defined, however defining multiple airfoil options for each section causes discontinues jumps in the objective domain. These discontinues jumps in the domain will cause problems for a sequential quadratic optimizer. The solution to this problem will be discussed in chapter 4.

Now that the geometry has been defined the only variables left for discussion are the flow variables. The two variables for the flow are the aircraft velocity and the altitude. The velocity is used to determine the design lift coefficient and the required moment coefficient, which in turn relates to the wing twist. The altitude is important to determine values like the air-density and the dynamic viscosity. However the altitude has been left out of the picture because of two reasons. First of all, mini-UAV's are limited to a maximum altitude of 300 meters, to avoid interference with normal aircraft traffic. This altitude limitation also has its effect on the second reason. The temperature, which strongly influences the

air density and dynamic viscosity, at these low altitudes changes drastically with time of the day, season, location on the earth, altitude, etc. . It would therefore not be practical to take this into account during an optimization. However it would be wise to take it into account during mission planning.

Constraints

To limit the search field of the optimizer and to ensure a feasible design it is important to apply different kinds of constraints. A large distinction must be made between linear and non-linear constraints. In the wing optimizer these two types of constraints will be used. The only linear constraints are inequality constraints, two for each variable, to define a lower and upper bound for the variables.

The non-linear constraints serve the main purpose of providing a feasible design and ensuring the quality of the aerodynamic calculation. All non-linear constraints used will be inequality constraints, to set an upper limit to the stall speed, ensure that the twist is not too large, set an upper bound on the design lift coefficient and to apply a lower bound on the Reynolds number. The first three ensure a feasible design and the bound on the Reynolds number is to ensure the credibility of Xfoil-results.

3.2.3 The Optimization Objective

In this section the value used to optimize for will be discussed and further referred to as the objective. In this section some interesting findings will be discussed for different situations. First of all the fact that the aircraft under consideration are using electric power, needs some extra attention. Apart from this it is interesting to observe the effect the subsystems, excluding the propulsive subsystem, have on the definition of the objective.

Range Objective for Electrically Powered Propeller aircraft

A distinction will be made in this section between the case in which energy from the batteries is used only for propulsion and the case where energy is drained from the batteries to supply all subsystems.

Battery only used for Propulsion

First of all it must be noted that electrically powered aircraft are quite similar to fuel powered aircraft. The similarity becomes clear when the electrical current is seen as the fuel flow and the battery capacity is treated as the fuel weight. Following the same derivation technique used by Breguet, and applying some assumptions one finds the electrical equivalent of the Breguet formula.

$$\begin{aligned} \frac{dC}{dR} &= \frac{\frac{dC}{dt}}{\frac{dR}{dt}} \\ \Downarrow \quad I_{el} &= -\frac{dC}{dt}, V_{\infty} = \frac{dR}{dt} \\ dR &= -\frac{V_{\infty}}{I_{el}} dC \end{aligned} \tag{3.49}$$

In this derivation C represents the electrical capacity and I_{el} represents the electrical current, while R and V are respectively the range and velocity. Integrating equation 3.49 will result in the overall range flown for a certain capacity consumption.

$$\begin{aligned} R &= \int_{C_1}^{C_2} -\frac{V_\infty}{I_{el}} dC \\ &\Downarrow \\ R &= \int_{C_2}^{C_1} \frac{V_\infty}{I_{el}} dC \end{aligned} \quad (3.50)$$

In this part C_1 is the start capacity and C_2 is the end capacity. The next step is to get the electrical current out of the picture by looking at the power required and the electrical power.

$$\begin{aligned} P_r &= D \cdot V_\infty \quad , \quad P_r = \eta_{tot} P_{el} \\ &\Downarrow \\ P_{el} &= \frac{D V_\infty}{\eta_{tot}} \\ &\Downarrow \quad P_{el} = U_{el} \cdot I_{el} \\ I_{el} &= \frac{D V_\infty}{\eta_{tot} U_{el}} \end{aligned} \quad (3.51)$$

,in which η_{tot} represents the total power efficiency from battery to propeller. Substituting equation 3.51 into equation 3.50 results in,

$$\begin{aligned} R &= \int_{C_2}^{C_1} \frac{\eta_{tot} U_{el}}{D} dC \\ &\Downarrow \\ R &= \frac{\eta_{tot} U_{el}}{D} \int_{C_2}^{C_1} dC \\ &\Downarrow \\ R &= \frac{\eta_{tot} U_{el}}{D} (C_1 - C_2) \end{aligned} \quad (3.52)$$

In this part the assumption is made that the electrical tension remains constant over time which is true for most of the discharge time except for the beginning and end of the discharge phase. The last step in the derivation is to rewrite the drag by using $D = \frac{C_D}{C_L} \cdot W$, resulting in the electrical range equation.

$$R = \eta_{tot} \frac{C_L}{C_D} \frac{1}{W} U_{el} (C_1 - C_2) \quad (3.53)$$

The capacity in this equation has the units ‘‘Ampère second’’, however in real life this unit is mostly expressed in ‘‘Ampère Hour’’, changing equation 3.53 into,

$$R = 3600 \cdot \eta_{tot} \frac{C_L}{C_D} \frac{1}{W} U_{el} (C_1 - C_2) \quad (3.54)$$

From this equation it is clear that the aerodynamic objective, to maximize range, is the maximization of the lift over drag ratio, the same as for fuel powered propeller aircraft.

This maximization of the lift over drag ratio can be simplified to an other ratio when optimizing the wing geometry with aspect ratios larger than 3.5, resulting in a new objective. The constraint on the aspect ratio is due to the non-linear behavior invoked by the influence of the tip-vortices on the lift and drag forces, rendering the conclusion from equation 3.55 invalid. The maximum lift over drag for a certain geometry can be found when the induced drag equals the zero lift drag, as can be seen in the following derivation:

$$\begin{aligned}
\frac{d\left(\frac{C_L}{C_D}\right)}{dC_L} &= 0 \\
&\Downarrow \\
\frac{d\left(\frac{C_L}{C_{D_0} + \frac{C_L^2}{\pi Ae}}\right)}{dC_L} &= \frac{\pi Ae(C_{D_0}\pi Ae + C_L^2) - 2C_L^2\pi Ae}{(C_{D_0}\pi Ae + C_L^2)^2} \\
&= \frac{C_{D_0}(\pi Ae)^2 - C_L^2\pi Ae}{(C_{D_0}\pi Ae + C_L^2)^2} = \frac{C_{D_0} - \frac{C_L^2}{\pi Ae}}{\left(\frac{C_{D_0}\pi Ae + C_L^2}{\pi Ae}\right)^2} = 0 \\
&\Downarrow \\
C_{D_i} &= C_{D_0} \\
&\Downarrow \\
C_D &= C_{D_0} + C_{D_i} = 2 \cdot C_{D_0} \tag{3.55}
\end{aligned}$$

From equation 3.55 it can be deduced that the maximum lift over drag ratio is found when the drag is equal to twice the zero lift drag and the lift corresponding to this drag is found to be,

$$C_L = \sqrt{C_{D_0}\pi Ae} \tag{3.56}$$

Substituting this into the maximum lift over drag ratio results in,

$$\left(\frac{C_L}{C_D}\right)_{max} = \frac{\sqrt{C_{D_0}\pi Ae}}{2 \cdot C_{D_0}} = \frac{\sqrt{\pi}}{2} \sqrt{\frac{Ae}{C_{D_0}}} \tag{3.57}$$

From equation 3.57 it becomes clear that the optimization objective, for an aircraft with aspect ratio higher than 3.5 and when energy is only used for propulsion, changes to the maximization of $\frac{Ae}{C_{D_0}}$. The constraint of the energy consumption is based on the validity of maximization of lift over drag which becomes invalid when other subsystems start to drain energy from the same source.

Some interesting sidemarks can be made by looking at this new objective. At first glance it might be obvious to maximize the aspect ratio, however when there is a constraint on the span, as is the case for most planes, the chord will decrease and thus the surface area. This increases C_{D_0} due to indirect consequences as there are:

- The decrease in surface area increases the relative impact of the fuselage & tail drag coefficient (see equation 3.24).
- The reduced size of the wing will result in components, like batteries, being moved from the wing to the fuselage increasing its size and thus its drag.

- The reduction in chord results in a slightly higher speed, to maintain the lift coefficient corresponding to $(\frac{C_L}{C_D})_{max}$. This increase in the speed, however, is not compensating the reduction in chord length thus reducing the Reynolds number. This might drastically increase the profile drag when Reynolds numbers become lower than $2 \cdot 10^5$.

Battery used for Propulsion and Subsystems

When all subsystems use energy from the same source as the propulsion system the objective will be different. To optimize the range, the speed will be higher than the one expected at maximum lift over drag, this is to minimize the time the other subsystems can drain energy. However a balance will be found between the minimization of the flight time and the power required for the increase in speed. The derivation of this range equation is the same up until equation 3.50 from this point on a distinction will be made between the power consumed by the propulsive system and the other systems.

$$\begin{aligned}
 R &= \int_{C_2}^{C_1} \frac{V_\infty}{I_{el}} dC \\
 &\Downarrow I_{el} = I_{el_{prop}} + I_{el_{sub}} \\
 R &= \int_{C_2}^{C_1} \frac{V_\infty}{I_{el_{prop}} + I_{el_{sub}}} dC \tag{3.58}
 \end{aligned}$$

In this equation $I_{el_{prop}}$ and $I_{el_{sub}}$ represent the electrical current for the propulsive subsystem and for all the other subsystems, respectively. The current used for the propulsion can now be rewritten using equation 3.51 resulting in,

$$\begin{aligned}
 R &= \int_{C_2}^{C_1} \frac{V_\infty}{\frac{DV_\infty}{\eta_{tot}U_{el}} + I_{el_{sub}}} dC \\
 &\Downarrow \\
 R &= \frac{V_\infty \eta_{tot} U_{el}}{DV_\infty + I_{el_{sub}} U_{el} \eta_{tot}} (C_1 - C_2) \\
 &\Downarrow \\
 R &= \frac{\eta_{tot} U_{el}}{\frac{C_D}{C_L} W + \frac{I_{el_{sub}} U_{el} \eta_{tot}}{V_\infty}} (C_1 - C_2) \\
 &\Downarrow \\
 R &= \frac{C_1 - C_2}{\frac{C_D}{C_L} \frac{W}{\eta_{tot} U_{el}} + \frac{I_{el_{sub}}}{V_\infty}} \tag{3.59}
 \end{aligned}$$

From this equation it becomes obvious that the maximization of the range is accomplished by the minimization of the denominator. In this denominator the first term demands for the minimization of $\frac{C_D}{C_L}$, similar to the original maximization of $\frac{C_L}{C_D}$, but at the same time the velocity must be as high as possible to minimize the second term. This means that the denominator will become the new objective to be minimized. In this equation the electrical tension is assumed to be constant as in equation 3.54. The conversion of units for the battery capacity also holds for equation 3.59 resulting in.

$$R = 3600 \frac{C_1 - C_2}{\frac{C_D}{C_L} \frac{W}{\eta_{tot} U_{el}} + \frac{I_{el_{sub}}}{V_\infty}} \tag{3.60}$$

Endurance Objective for Electrically Powered Propeller Aircraft

The electrical endurance equation will be derived here for completeness reasons, however it will not be used in this project, but will be interesting to future work. The distinction made, in the range equation, between the case for which power was consumed by the propulsive system only or by all subsystems, will not be interesting for the endurance case. The endurance will only be reduced by the consumption of energy by the other systems, and has no further influence on the speed nor the aerodynamic objective. The equation to calculate the endurance in the case were all systems consume energy from the same source will be given at the end of this section.

The derivation of the electrical endurance equation is the following,

$$\begin{aligned}
 E &= \int_{t_1}^{t_2} dt \\
 &\Downarrow I_{el} = -\frac{dC}{dt} \\
 E &= \int_{C_1}^{C_2} -\frac{dC}{I_{el}} \\
 &\Downarrow \\
 E &= \int_{C_2}^{C_1} \frac{dC}{I_{el}} \tag{3.61}
 \end{aligned}$$

Using equation 3.51 it is possible to get the electrical current out of the picture.

$$\begin{aligned}
 E &= \int_{C_2}^{C_1} \frac{\eta_{tot} U_{el}}{DV_{\infty}} dC \\
 &\Downarrow \\
 E &= \frac{\eta_{tot} U_{el}}{DV_{\infty}} (C_1 - C_2) \\
 &\Downarrow D = \frac{C_D}{C_L} W, V_{\infty} = \sqrt{\frac{2W}{\rho S C_L}} \\
 E &= \frac{\eta_{tot} U_{el}}{\frac{C_D}{C_L} W \sqrt{\frac{2W}{\rho S C_L}}} (C_1 - C_2) \\
 &\Downarrow \\
 E &= \sqrt{\frac{C_L^3}{C_D^2}} \sqrt{\frac{S\rho}{2W^3}} \eta_{tot} U_{el} (C_1 - C_2) \tag{3.62}
 \end{aligned}$$

From this equation it is obvious that the maximization of $\frac{C_L^3}{C_D^2}$ remains the endurance objective, even when dealing with electrically powered propeller aircraft.

The units for the capacity must be adapted to Ampère hour, resulting in,

$$E = 3600 \cdot \sqrt{\frac{C_L^3}{C_D^2}} \sqrt{\frac{S\rho}{2W^3}} \eta_{tot} U_{el} (C_1 - C_2) \tag{3.63}$$

To include the power consumed by the non propulsive subsystems one can use the same technique, as for the range equation, of distinguishing between electrical current used by the propulsive system and by the other systems. The resulting formula is the following,

$$E = 3600 \cdot \frac{\eta_{tot} U_{el}}{\sqrt{\frac{C_D^2}{C_L^3} \frac{2W^3}{S\rho} + \eta_{tot} U_{el} I_{el_{sub}}}} (C_1 - C_2) \quad (3.64)$$

From this equation it is obvious that the only ratio influenced by the aerodynamics is $\frac{C_D}{C_L}$ which has to be minimized or, as before, $\frac{C_L^3}{C_D^2}$ has to be maximized.

As for the range, the $\frac{C_L^3}{C_D^2}$ changes into a new objective function when optimizing the wing geometry. The only constraint for this change is that the aspect ratio of the wing is larger than 3.5. The non-linearities in the forces, due to the tip-vortices at lower aspect ratios, prevents the derivation of equation 3.65. The same technique as in equation 3.55 will be used to state,

$$\begin{aligned} \frac{d\left(\frac{C_L}{C_D}\right)}{dC_L} &= 0 \\ \Downarrow \\ C_{D_i} &= 3C_{D_0} \end{aligned} \quad (3.65)$$

Substituting this into the ratio, $\frac{C_L^3}{C_D^2}$, results into,

$$\left(\frac{C_L^3}{C_D^2}\right)_{max} = \frac{(3C_{D_0} \pi A e)^{\frac{3}{2}}}{(4 \cdot C_{D_0})^2} = \frac{(3\pi)^{\frac{3}{2}} \sqrt{(Ae)^3}}{16 (C_{D_0})^2} \quad (3.66)$$

Thus to optimize the wing geometry for endurance, including the case where the subsystems consume power from the same source as the propulsion, the ratio $\frac{\sqrt{(Ae)^3}}{(C_{D_0})^2}$, must be used as the objective function.

Implementation of the Theory

The construction of the optimization program will be the topic for this chapter. The theory explained before will be implemented in a program which has the purpose to find the best wing for a certain aircraft weight. This program exist out of an optimization algorithm that uses a newly developed program to determine the objective value. This new program is a quasi-3D method for determining the aerodynamics of a wing.

Section 4.1 will provide an insight into the program setup with a detailed description of every step taken during the optimization process. This is followed by section 4.2, with an overview of the differences between the theory and the actual implementation. An extensive validation of the new quasi-3D method will be provided in section 4.3, by comparing it to CFD results and experimental results. The wings for the validation process were carefully selected to provide a broad validation basis. At the end of the chapter, in section 4.4, the reasons for developing this quasi-3D method are repeated and checked against its performance.

4.1 Program Setup

The idea behind an optimization is to start with an initial design which is iteratively changed to obtain the final design. The iterative loop for the wing optimization can be seen in figure 4.1. This flow diagram will be used as a guideline through the following discussion, every block in the diagram will correspond to a subsection. Figure 4.2 provides an insight in all the functions used in the program and shows there relation to each other. From this figure it becomes clear that all aerodynamic data, two dimensional or three dimensional, are obtained from external programs, like Xfoil and AVL. The airfoil data obtained from Xfoil is stored in a structured way, with the idea to reduce calculation time. The way this data is stored will be explained in 4.1.7.

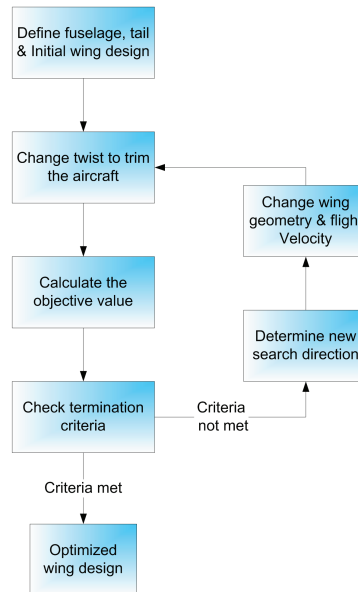


Figure 4.1: Program flow diagram.

4.1.1 Program Initialization

The program initialization serves the purpose to provide the information needed by the program to start the optimization. Several inputs are required to define some constant design values and to define the boundaries and initial values of the optimization variables. An overview of these parameters can be found below.

Fixed Parameters

The fixed parameters are used to define some specific aircraft details, that are constant during the optimization.

- General parameters
 - Aircraft mass [kg]: Required to determine the design lift coefficient.
 - Stability margin [%]: This value is required to define the wing twist.
- Wing parameters
 - Wing transition point for the upper and lower surface at each section: This is used to force transition at a certain chord wise location on the wing. The values vary from 0 to 1. Set to 0, transition is forced at the leading edge and 1 is used for free transition. This parameter is a vector of length equal to the number of wing sections. In between the sections the forced transition is linearly varied from one section to the other.
- Fuselage parameters

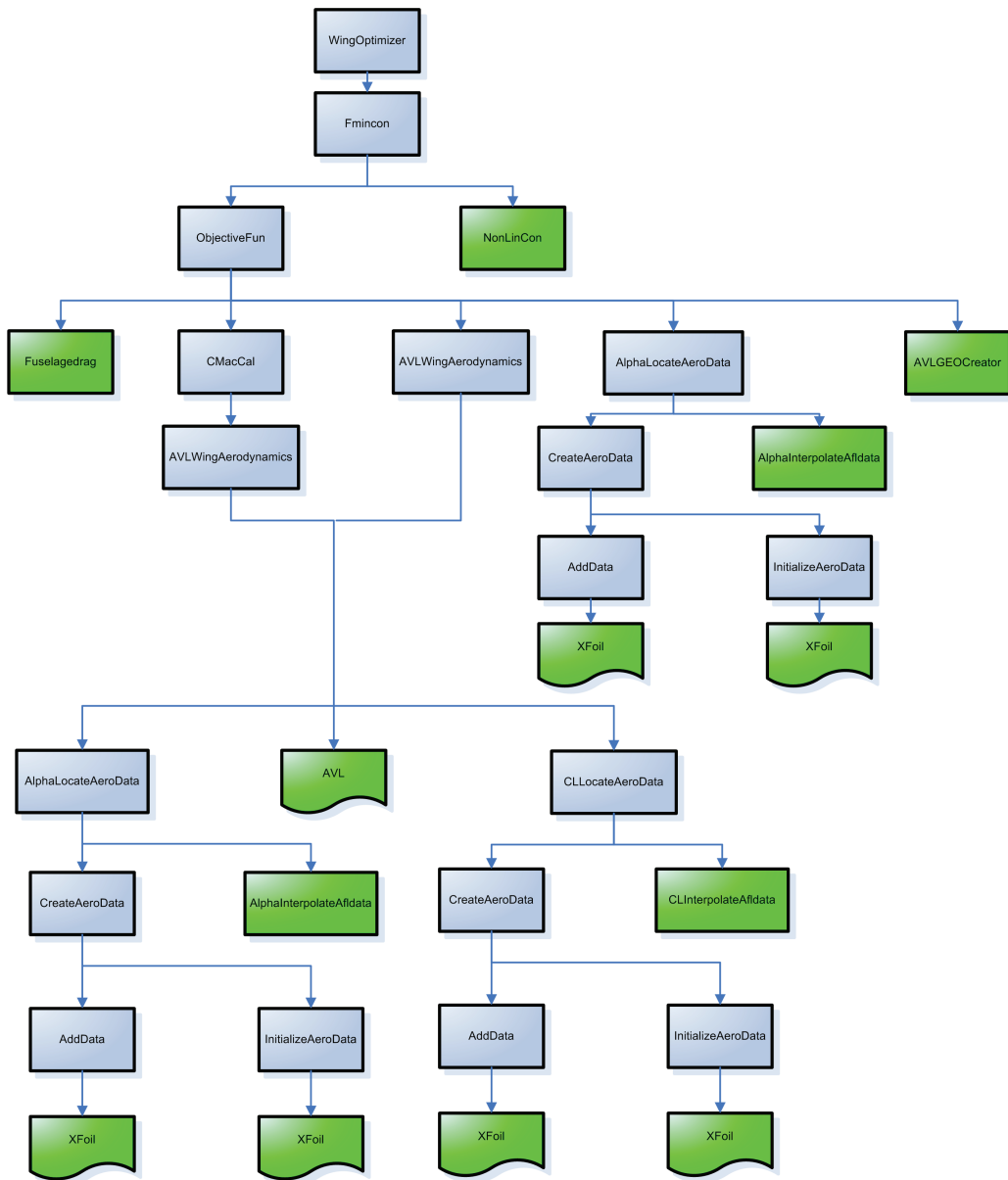


Figure 4.2: Overview of the program structure, in which it is visualized how functions relate to each other.

- Fuselage cross-section: This parameter can have three values, 'circular', 'rectangular' or 'none', according to the fuselage cross-sectional shape.
- Fuselage length: The fuselage length is used to determine the thickness ratio and the fuselage Reynolds number
- Propeller efficiency: The velocity increase over the fuselage, due to the propeller, can be determined using this efficiency. This velocity increase is needed to establish the fuselage Reynolds number which in turn effects the fuselage

- drag. When the propeller is not in front of the fuselage this value must be set to 1. The parameter range is $]0, 1]$.
- Fuselage transition point: This value is used to determine the fuselage friction drag. It is hard to determine an accurate value but an educated guess will provide sufficient accuracy. It is advised to set this value to zero when a prop is present in front of the fuselage. The values range is $[0, 1]$.
 - Fuselage diameter [m]: When the fuselage cross-section is set to 'circular' it is required to provide the fuselage diameter at the largest cross-section.
 - Fuselage height [m]: When the fuselage cross-section is set to 'rectangular' one has to provide the height at the largest cross-section.
 - Fuselage width [m]: When the fuselage cross-section is set to 'rectangular' one has to provide the width at the largest cross-section.
- Tail parameters
 - Number of tail surfaces: Indicates the number of vertical tail surfaces
 - Tail root chord [m]: Defines the root chord length of the vertical tail. This parameter is a vector of length equal to the number of tail surfaces.
 - Tail tip chord [m]: Defines the tip chord length of the vertical tail. This parameter is a vector of length equal to the number of tail surfaces.
 - Tail span [m]: Defines the span of the vertical tail. This parameter is a vector of length equal to the number of tail surfaces.
 - Tail airfoil: Defines the airfoil of the vertical tail. This parameter is a vector of length equal to the number of tail surfaces.

Optimization Variables

The optimization variables require constraints and initial values before starting the optimization. The variables were already discussed in chapter 3.2.2 however a more in dept discussion will be presented to avoid any ambiguities.

The only flow variable, the airspeed, requires no further explanation, this is a single value defining the flow velocity at infinity. This variable is bound by an upper and a lower limit, and, like all variables, requires an initial value. There are also three nonlinear constraint acting on this variable as will be explained later on.

The geometric variables can be seen in figure 4.3 in which an example is presented of a wing with three sections (two surfaces). Most of the variables, to define the geometry for this example, will be vectors with two elements, except for the root chord.

All geometric variables require an upper and a lower bound and an initial value to start the optimization. The vectors of the bounds for the sweep and taper must have the same length as for the variables themselves such that different bounds can be applied to them for every surface or section. The upper and lower bounds for the span only requires one value. The sum of all section spans will then be limited by these bounds. This is to enable the user to specify a minimum and maximum total wing span. The upper and lower bound vector, for the root chord, naturally contain only one element constraining its domain.

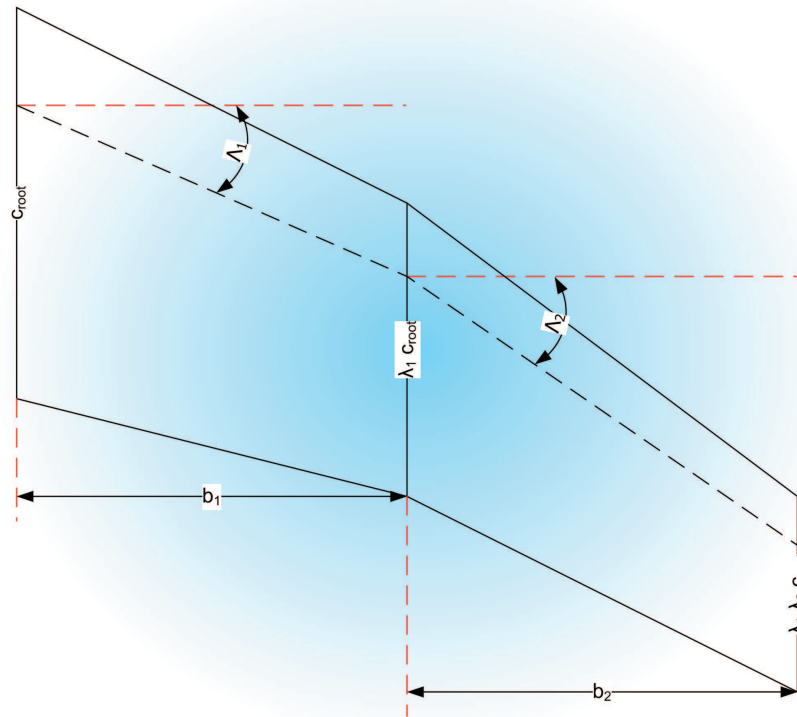


Figure 4.3: Example of the geometric variables for a wing with three sections (the subscripts define the vector element).

As mentioned earlier, the bounds are implemented as linear inequality constraints. This is because inequality constraints are incorporated into the optimization problem while bounds have to be checked which decreases the efficiency.

Apart from the bounds, the initial values of the variables need to be provided. It is obvious that these initial values are contained within the specified bounds and that they preferably also meet the non-linear constraints. A good initial guess is not necessary but will most likely shorten the time it takes to find the optimum.

The other geometric variables, not represented in the figure, are the twist, dihedral and the airfoils. The twist will be explained in the following section as it is dependent on the other variables. For now, the dihedral is not considered as a variable, as it mainly influences the lateral stability and not so much the range performance. As mentioned earlier, from experience it was noted that the aileron efficiency of these small aircraft is really high providing the autopilot with great controllability in the lateral direction. This was the reason to only consider wings without dihedral.

The airfoils have to be defined at all sections. The variables defined this far have been continuous variables, meaning that they can have any value within the constraints. The airfoils, however, are implemented as discrete variables, which means that different options must be specified which all have to be evaluated separately. Having a lot of different airfoil combinations will increase the calculation time dramatically. The user has to provide all

airfoil combinations that he/she wants to evaluate. Every airfoil combination then requires a separate optimization of the continuous variables, as having the airfoils changed in the same process as the continuous variables will result in an objective domain with local minima. As mentioned before, the sequential quadratic algorithm does not handle local minima to well. The best airfoil combination is selected at the end of all optimizations. This however is probably not the fastest way of optimizing and thus requires further investigation.

4.1.2 Changing the Wing Twist

Once the optimization is initialized, the iterative loop of looking for the best wing can be entered. The first step in this loop is determining the wing twist such that a trimmed straight horizontal flight is achieved. This in itself requires an iterative loop which, regrettably, increases the optimization time drastically¹. In figure 4.4 an overview of this iterative process can be seen.

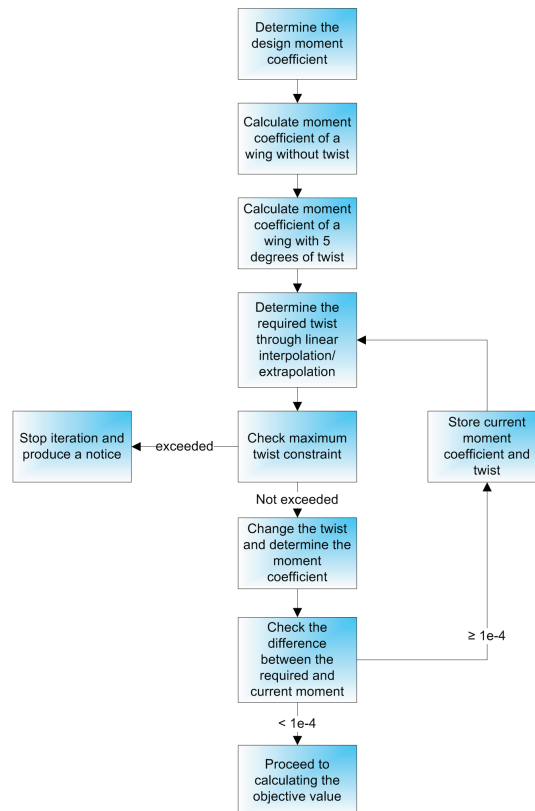


Figure 4.4: Illustration of the iterative loop to determine the required twist.

The determination of the required moment coefficient is done with the help of equation

¹For normal configurations (wing-fuselage-tail-configurations) this iterative process can be skipped by fixing the twist and thus reducing the calculation time.

3.38. From the figure it is also clear that the moment coefficient around the aerodynamic center needs to be determined at least 3 times. The longitudinal location of the aerodynamic center needs to be established every time the moment coefficient is evaluated. This involves evaluating equation 3.36 which requires a double quasi-3D aerodynamic evaluation of the wing to determine the C_{M_α} and C_{L_α} . Resulting in at least 6 quasi-3D aerodynamic calculations only to determine the twist, drastically increasing the calculation time.

4.1.3 Evaluating the Objective Function

At this point the complete wing geometry is defined, and thus can the process of determining the objective value start.

The first part in determining the objective value, is estimating the drag at the lift coefficient for straight horizontal flight at the requested velocity. This drag is the sum of the wing, fuselage and tail drag. The aircraft is first trimmed at the required angle of attack such that the lift equals the weight. This is done using the quasi-3D method, which also provides information on the wing drag.

The tail drag is determined using a very simplified version of the quasi-3D method. The vertical tail, in a non-slipping flight, is not producing lift so a good approximation is to determine the profile drag of the vertical tail airfoil at the Reynolds number corresponding to the tail mean aerodynamic chord. The following step is to determine the fuselage drag which is easily obtained using equations 3.16 to 3.24.

Once these values are in place it is only a matter of substituting them into the equation suiting the aircraft purpose and its power usage, as explained in chapter 3.2.3.

4.1.4 Checking Termination Criteria and Non-linear Constraints

Termination Criteria

Once the optimization is running it must know when it is close enough to the optimum to stop. This is done by the termination criteria. There are two types of termination criteria, the ones that limit the number of iterations or function evaluations and the ones that put constraints on the variation of certain values.

The limitations on the number of iterations and function evaluations are set such that they are almost never the termination criteria. This is because they can stop the optimization before the actual optimum is found. However they become active in case the optimization is taking too long or an optimum is hard to find.

The other criteria take into account the variation of the objective function, the variation of the variables and the tolerance on the non-linear constraint violation. Once these criteria are met the optimization will break out of the iterative loop and assume that the obtained result is the optimum. These termination criteria are better for determining the end of the optimization as they are directly linked to the result.

Non-linear Constraints

Apart from the bounds on the variables, some non-linear constraints are imposed on the variables. These non-linear constraints are:

- A lower limit on the Reynolds number
- A upper limit on the stall speed
- A upper limit on the maximum twist
- A upper limit on the design lift coefficient

The lower limit on the Reynolds number is to ensure that the results obtained from Xfoil are still correct. A major problem for Xfoil is to predict bubble bursting which arises at very low Reynolds numbers. This bubble bursting can be seen in figure 4.5, where experimental results are compared to Xfoil. Once the adverse pressure gradient, increases with increasing angle of attack, even the turbulent boundary layer is not able to reattach to the surface any more. This results in a large separated flow region over the airfoil and appears as if the laminar separation bubble suddenly bursts. This effect can be seen in the force coefficients as a sudden drop in the lift coefficient and a strong increase in the drag (see figure 4.5). However predicting this bubble burst is very hard and is a result of a combination of the adverse pressure gradient and the Reynolds number. Limiting the Reynolds number to a lower bound should, at least partially, avoid this problem. The lowest Reynolds number for the wing is calculated using,

$$Re_{min} = \frac{c_{tip} \cdot V_{\infty}}{\nu} \quad (4.1)$$

A limit on the stall speed has more to do with the practical side of using mini-UAV's than with the performance itself. Without this limit the optimizer might look for high aspect ratio wings to reduce the induced drag, however together with a limit on the span this might result in a very small wing surface area. This in case of flying wings, with their reflexed (read less cambered) airfoils and thus lower $C_{L_{max}}$ values, will result in rather high stall speeds. High stall speeds imply that the operator can't throw the airplane anymore but must use a launching system for the take-off. Launching systems add weight to the overall system and, when kept small, put a very large force on the aircraft. However controlling this stall speed limit provides the user with the option to optimize the design with a certain take-off in mind. The stall speed is determined using

$$V_{stall} = \sqrt{\frac{2 \cdot W}{\rho S C_{L_{max}}}} \quad (4.2)$$

In this equation $C_{L_{max}}$ has to be supplied by the user. In the future the quasi-3D method must be validated for its capability to determine the maximum lift coefficient. At this point it can not be assured that the maximum lift coefficient obtained with this method is correct as its stall is predicted from Xfoil airfoil data, which become less accurate when

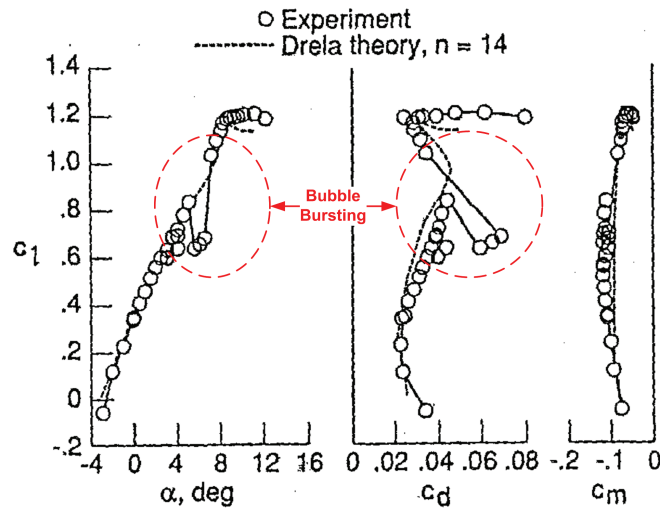


Figure 4.5: Effects of bubble bursting and the comparison with Xfoil results (figure obtained from reference [8]).

dealing with separated flow. Next to that, the spreading of the separated flow over the wing is a three dimensional phenomena not predicted with the vortex lattice method. Further investigation is required and might result into a good prediction of the maximum lift coefficient.

The maximum twist constraint and the design lift coefficient is to avoid that the optimizer starts looking for a wing that is just not feasible and that it does not waste time in calculating the aerodynamics for them.

4.1.5 Determining the New Search Direction

When the termination criteria are not met the algorithm starts with establishing a new geometry and speed for the following iteration. This is part of the constraint optimization algorithm available in Matlab. As explained earlier it resorts to the sequential quadratic programming algorithm to establish a new search direction and uses the line search to establish the distance it will travel in that direction.

4.1.6 Changing the Wing Geometry and the Flight Speed

Once the new direction and distance is established, a new geometry and speed are determined. Those values will then be used to repeat the twisting of the wing, objective function evaluation and checking the termination criteria. This process keeps repeating itself until the termination criteria are met.

4.1.7 Airfoil Data Storage and Retrieval

The Xfoil calculations on the airfoils form the backbone of the complete quasi-3D method. As this data will be accessed quite a lot it is of importance that the retrieval of the required data is fast. Based on this argument it was decided to store the data in a structured way rather than running Xfoil for every strip and for every wing as this would be too slow and inefficient.

Storage

Storing the data requires a structured set-up such that the data is easy to find and retrieve when needed. The database is contained under one single folder in which the Matlab structures, with the airfoil name as filename, are saved. Such a structure is set up in layers, as is presented in figure 4.6.

From this figure it is clear that storage of the viscous data is always with a Reynolds number step of $2 \cdot 10^4$ and with a forced transition step of 0.05 (ranging from 0.05 to 1). Forced transition is only applied if the transition is aft of the forced transition location and will be free once it moves in front of the specified location, for higher angles of attack.

When running the quasi-3D method an automatic check of the database will be performed to establish that the required data is present. The database will automatically be created or expanded when the requested data is not present. The way this checking algorithm works can be seen in figure 4.7. From this figure it can be seen that the lowest Reynolds number available in the database will be $6 \cdot 10^4$.

Figure 4.7 also shows that when the airfoil is used for the first time a basic database is created. This includes the basic information of the airfoil and a start of the aerodynamic database. The basic airfoil and aerodynamic information includes:

- Airfoil x and y coordinates
- Inviscid aerodynamic data
- Inviscid aerodynamic data for the airfoil reduced to 1% thickness
- Viscous aerodynamic data from Reynolds number $6 \cdot 10^4$ to $1.3 \cdot 10^6$ with steps of $2 \cdot 10^4$ and free transition
- Viscous aerodynamic data from Reynolds number $6 \cdot 10^4$ to $1.3 \cdot 10^6$ with steps of $2 \cdot 10^4$ and transition forced at 5% chord on the lower and upper surfaces

The inviscid data is saved for angles of attack ranging from -10° to 20° in steps of 0.1° , while the viscous data is stored from -5° to 20° in steps of 0.1° . The viscous data is prone to Xfoil not being able to converge for certain angles of attack. These angles are automatically skipped as they are not passed to Matlab. This database will be expanded automatically once different Reynolds numbers or different tripping locations are required.

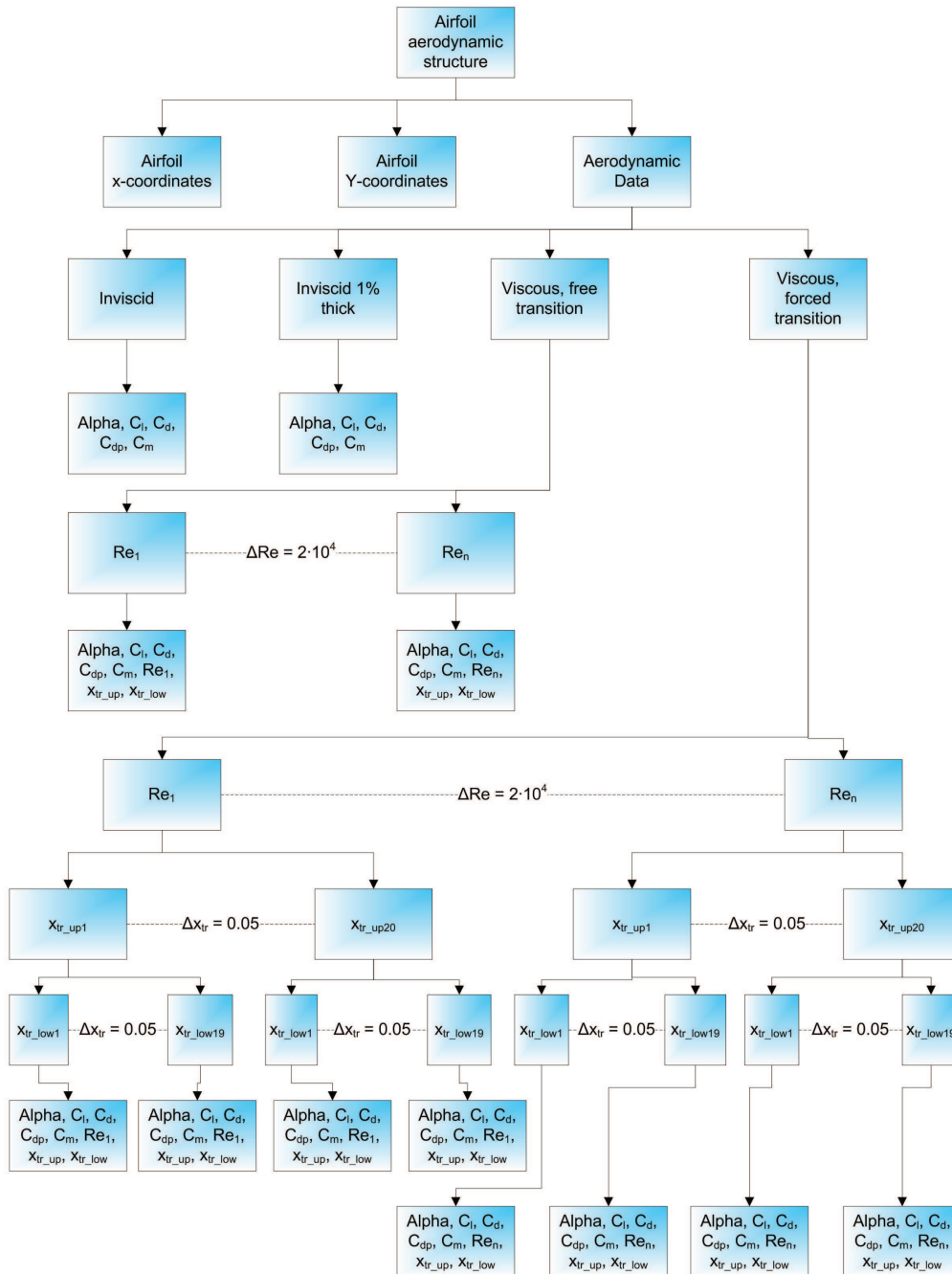


Figure 4.6: Overview of how the airfoil aerodynamic data is stored in a structured way.

Retrieval

The retrieval of the airfoil data is preceded by an evaluation of the database, as can be seen in figure 4.7. This evaluation is necessary to ensure that the required data is present.

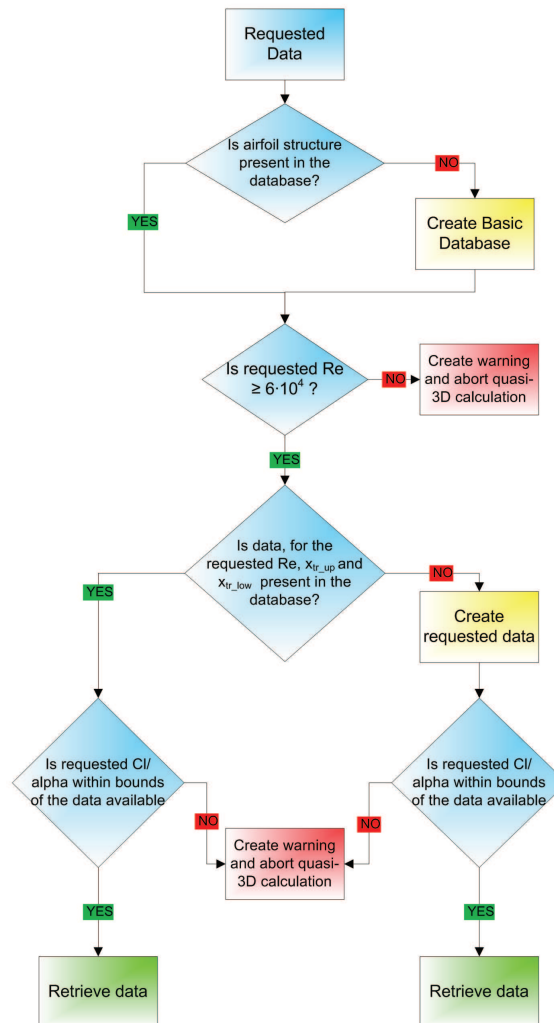


Figure 4.7: Overview of how the airfoil aerodynamic data is created and retrieved.

Once ensured that the data is present a search algorithm starts looking for the required data. For that it needs information on several values to establish the location in the database, these values are:

1. Airfoil name
2. Inviscid or viscous
3. Inviscid: normal or 1% thick
4. Viscous: Reynolds number
5. Viscous: Upper and lower surface transition locations

6. Depending on the search algorithm: α or C_l

To clarify how the retrieval works an example of a viscous forced transition data retrieval will be shown. Assume that the data required is the following

- Airfoil name: S5010
- Viscous: $Re = 212000$, $x_{tr_up} = 1$, $x_{tr_low} = 0.82$
- Alpha-search: $\alpha = 0.32$

The algorithm knows to start looking in the “viscous-forced transition” database, as one of the forced transition values is lower than one. It then looks for the data surrounding the requested Reynolds number, in this case data with Reynolds numbers $2 \cdot 10^5$ and $2.2 \cdot 10^5$ (remember stored data is available for $\Delta Re = 2 \cdot 10^4$). Next, it determines the data closest to the forced transition point locations, or for the example, $x_{tr_up} = 1$ and $x_{tr_low} = 0.8$ (remember stored data is available for $\Delta x_{tr} = 0.05$). This leads directly to two vectors with angle of attack information. If these vectors are empty it will automatically request Xfoil to generate the airfoil aerodynamic data, after which it is checked and stored at this location in the database. Then the two angles of attack surrounding the requested angle of attack are selected, $\alpha = 0.3$ and $\alpha = 0.4$. This provides 4 data locations, two for each Reynolds number. The last step is to linearly interpolate the corresponding aerodynamic coefficients, C_l and C_d , for the right angle of attack and for the requested Reynolds number (see figure 4.8 for the case of a C_l -interpolation)

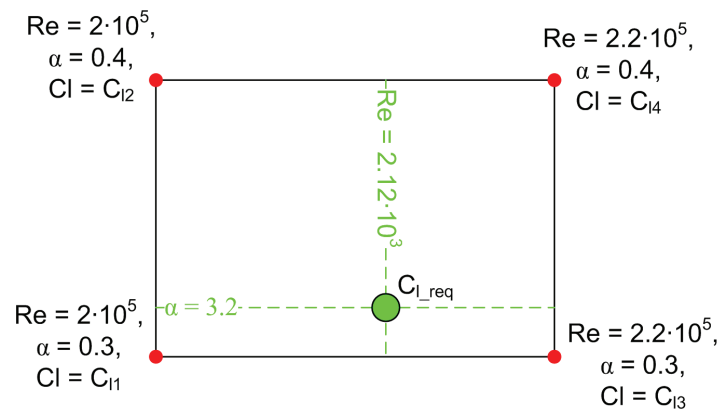


Figure 4.8: Interpolation for airfoil aerodynamic data retrieval.

The interpolation is only performed for the Reynolds number and angle of attack, while the forced transition is located to the closest value. Interpolating for the forced transition point is a recommended improvement for future versions of the program. It was omitted as the closest forced transition was good enough for this research.

4.1.8 AVL and Xfoil Settings

Xfoil Settings

The amount of panels defined in the airfoil files, that will be loaded into Xfoil, might differ substantially. To remove this discrepancy an option in Xfoil is called upon to rearrange the airfoil paneling before calculating the aerodynamics. With this option the number of panels and its distribution can be changed. The number of panels for the quasi-3D calculations is set to 240 while the remaining options, for defining the distribution, are left at their default values. A clear illustration of this panel rearrangement can be seen in figure 4.9. It is clearly visible that the leading edge has a way higher panel density and that it also increases a bit towards the trailing edge.

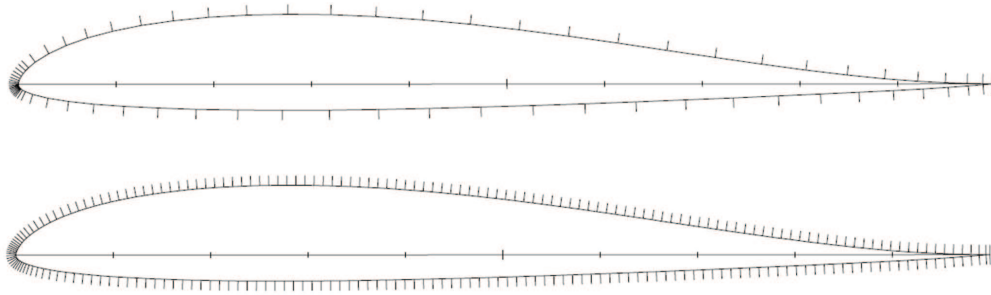


Figure 4.9: Comparison between original paneling (upper airfoil) with 77 panels and the rearranged paneling with 240 elements (lower airfoil).

Another important feature in Xfoil is the prediction of the transition point on the airfoil, which is dependent on the ambient turbulence level. The theory behind this is rather complicated, however more information can be found in reference [7]. In Xfoil the ambient turbulence can be controlled with the critical amplification ratio, n_{crit} . The higher this value the lower the ambient turbulence. This n_{crit} is left at the default value of 9, which corresponds to a turbulence level of 0.07%. The value has a rather significant impact on the drag when changed between the extreme of high ambient turbulence ($n_{crit} = 6$, turbulence level = 0.245%) and a very low one ($n_{crit} = 14$, turbulence level = 0.009%) as can be seen in figure 4.10.

The normal procedure is to test the airfoil in a wind tunnel and based on those results a convenient n_{crit} is selected. However the wind tunnel turbulence level (LST turbulence level at 20m/s is 0.015% see reference [3]) is different from the atmospheric turbulence level, which in turn depends on the weather when considering low altitudes. As this research deals with the optimization of low flying mini-UAV's, an intermediate value of $n_{crit} = 9$ is selected for the optimizer. On a clear day without too much wind this value will probably be too low, but at the same time too high for a very gusty day.

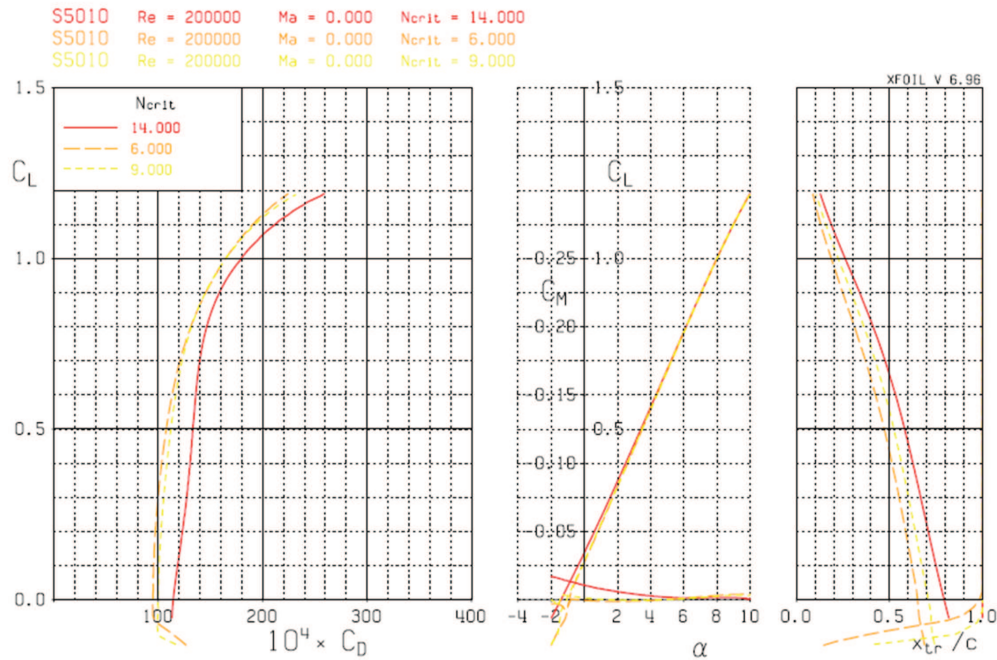


Figure 4.10: Comparison between Xfoil calculations at different turbulence levels.

AVL Settings

The only setting of importance for the vortex lattice method is the grid layout. The grid is defined for half the wing and AVL is notified of the fact that it is symmetric. The wing, independently of the number of sections, will have 40 elements in spanwise and 20 in chordwise direction. Resulting in a total of 800 elements for half the wing. The distribution of these panels is such that they are more concentrated towards the edges and the root, as the pressure gradients are higher at these locations. However the density for the tip and the leading edge are the highest. A typical grid layout for the vortex lattice method can be seen in figure 4.11.

4.2 Differences between the Quasi-3D Method and the Theory

Two empirical corrections have been made to the quasi-3D method such that better results are obtained. A correction is introduced for the problem with the induced drag estimation discussed in section 3.1.2. While the other one is to better estimate the zero lift angle of attack (see section 3.1.1)

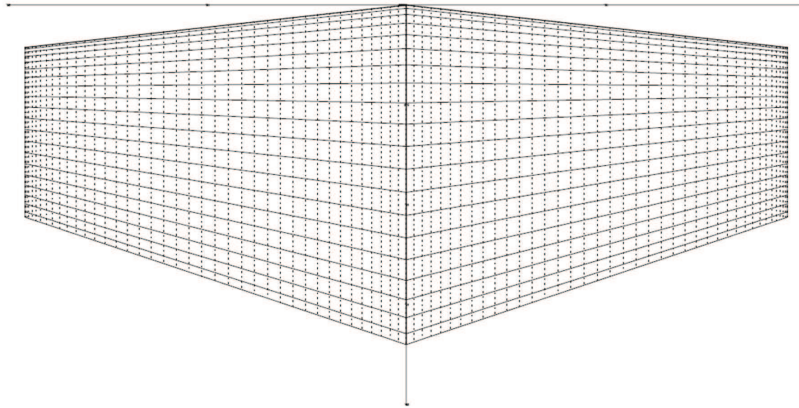


Figure 4.11: Typical AVL grid.

4.2.1 Problems with the Induced Drag

As mentioned earlier, the induced drag is overestimated by the quasi-3D method. This problem arises as there might be a difference between the induced angle of attack required for the determination of the correct lift coefficient and the one for tilting the lift vector backward. In reference [15] it is mentioned that there is a difference in these angles, however it is not explained why there is a difference nor how to calculate it.

The solution to this problem proved to be simpler than expected. Using the generally accepted formula for estimating the induced drag:

$$C_{D_i} = k \frac{C_L^2}{\pi A} \quad (4.3)$$

In this formula the value of k is kept constant at 1 which is not entirely correct but proves to work rather well as will be shown in the validation of the code. However this definitely needs more attention as it is not what the author had in mind for calculating the induced drag.

To clarify, the quasi-3D method is used to establish the profile drag and its variation with the lift coefficient, while the induced drag is calculated using equation 4.3.

4.2.2 Improved Estimation of the Zero Lift Angle of Attack

The vortex lattice method proved to underestimate the lift coefficient. This was mainly due to the difference in the zero lift angle of attack, as explained earlier, caused by the assumptions made in the vortex lattice method. A method to correct for this, that seemed to work extremely well, was to shift the zero lift angle of attack of the wing towards the zero lift angle of attack of the viscous airfoil data. Without twist in the wing the zero lift angle of the wing and the airfoil should be the same. This is due to the fact that there is no lift and thus no downwash angle present.

Equation 3.8, used to determine the effective angle of attack, was accordingly changed to use the α_0 and C_{l_α} from the viscous airfoil data. This equation then became:

$$\alpha_{eff} = \frac{C_l}{C_{l_{\alpha_{visc}}}} + \alpha_{0_{visc}} \quad (4.4)$$

The improvement suggested here can be seen in figure 4.12 and 4.13. The results presented in figure 4.12 are found using the quasi-3D method with equation 3.8 used to determine the effective angle of attack. Figure 4.13 shows results for the quasi-3D method with the above mentioned improvements, resulting in equation 4.4 to determine the effective angle of attack. The difference in the lift curve of figure 4.12(A) have completely disappeared in figure 4.13(A) while the estimation of the maximum lift over drag ratio maintained its accuracy.

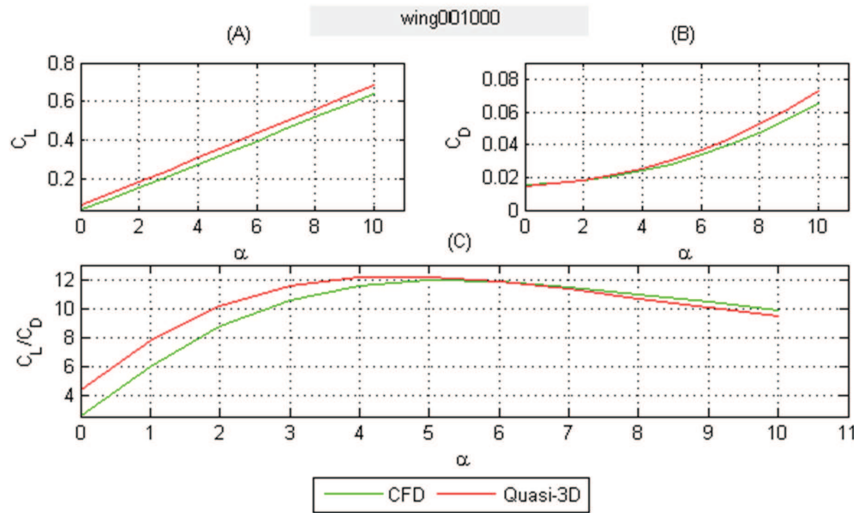


Figure 4.12: Inviscid, thin definition of α_0 .

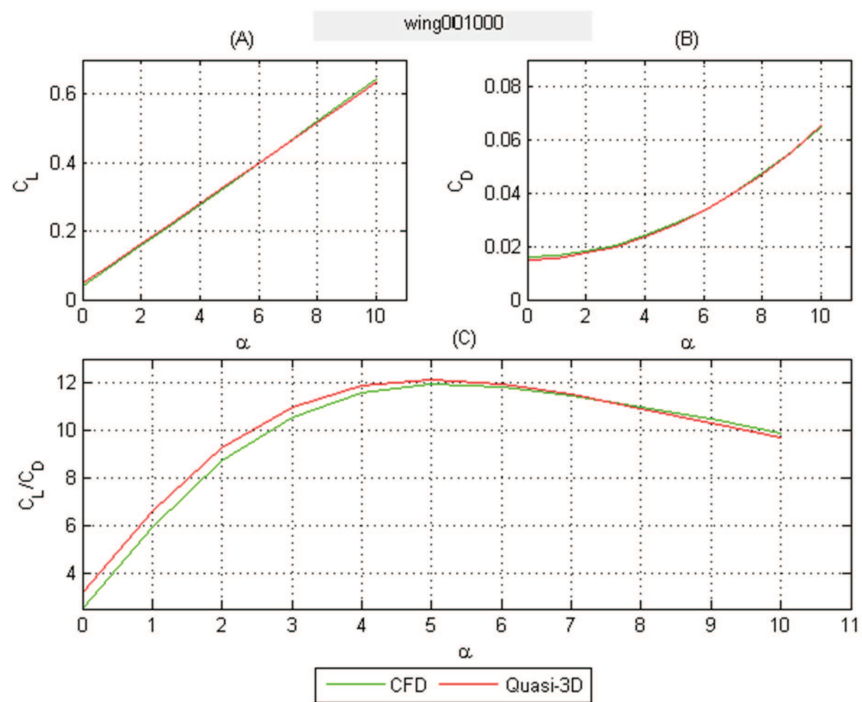


Figure 4.13: Viscous definition of α_0 .

4.3 Quantitative Validation of the Quasi-3D Method

The validation of the quasi-3D method is performed using CFD results and wind tunnel data. The CFD calculations are obtained during this research and their purpose is to define the gradient in the maximum lift over drag ratio for wings with varying sweep and taper. The validation with wind tunnel data was done by comparing the results obtained with the quasi-3D method to wind tunnel data found in literature (reference [5] and [6]).

The selection of the wing shapes for the CFD calculations were such that they complement the wind tunnel results found in literature. Those wind tunnel results are however obtained at a high Reynolds number ($Re = 3.2 \cdot 10^6$) when considering mini-UAV's, and have a higher than expected aspect ratio. However validation for different Reynolds numbers and aspect ratios only proves the capabilities and limits of the quasi-3D method.

4.3.1 Validation with CFD

The CFD-results for the validation were obtained using Fluent 6.3 and Gambit was used to create the grid.

The first step in obtaining CFD results, is the tedious work of generating a grid and providing the appropriate Fluent settings. In reference [20] an extensive investigation was presented into a good grid size and on the preferred Fluent settings, for low Reynolds number wings. The results obtained with CFD assume a fully turbulent flow which is approximated in the quasi-3D method by using airfoil data with a forced transition point at 5% of the chord².

The Grid

The dependency of the results on the grid were determined in reference [20] and will not be investigated further. Having a similar grid and the same Fluent settings as reference [20] was used to ensure good results.

The domain around the wing is a C-grid with the dimensions shown in figure 4.14. The grid itself is constructed out of $\sim 1 \cdot 10^6$ hexahedral elements with a boundary layer around the wing and the grid density decreases towards the outside of the domain. The grid is refined towards the leading and trailing edge of the wing and the tip, clearly illustrated in figure 4.15. This is to capture the large pressure gradients at those edges. Hexahedral cells were selected as they can have a higher aspect ratio in the direction of the flow reducing numerical diffusion. However this results in a higher density of the cells at positions where it is not necessarily needed, which might increase the calculation time.

Boundary Conditions and Fluent Settings

The boundary conditions for the C-grid are rather straight forward. The front side is defined as a velocity inlet for which only the velocity magnitude and the direction must

²Forced transition at 0% of the chord is not possible in Xfoil. 5% is the closest to fully turbulent in the quasi-3D method

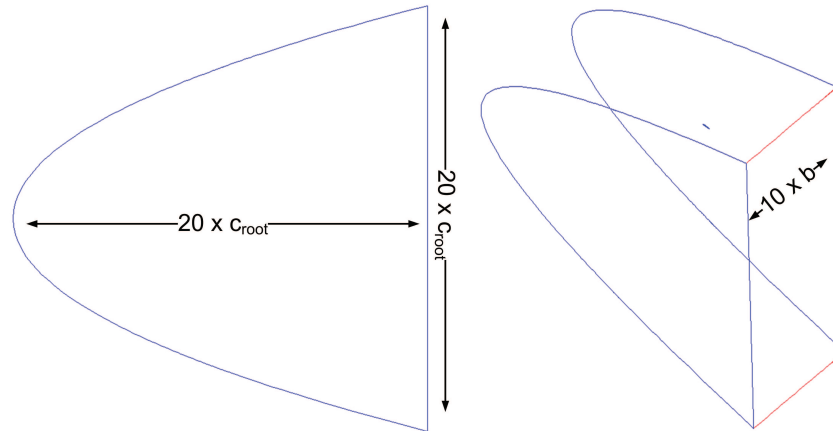


Figure 4.14: Outer dimensions of the domain around the wing.

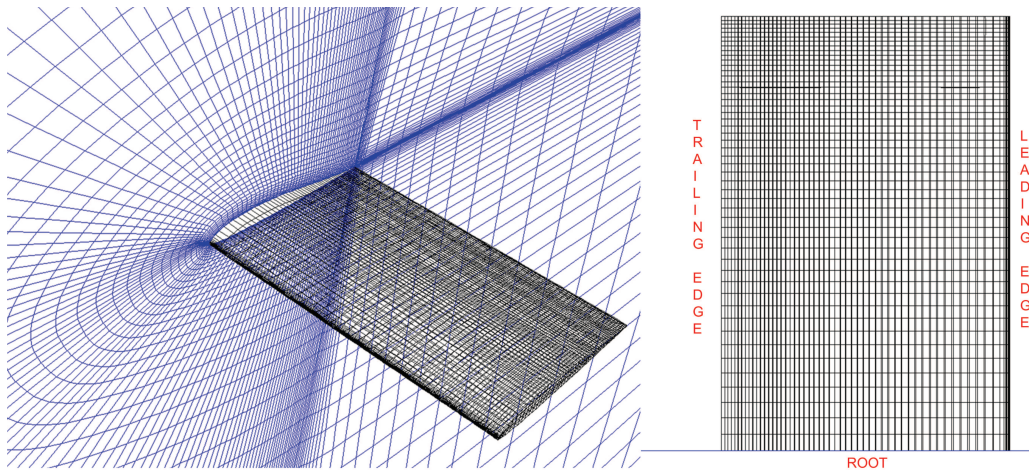


Figure 4.15: Refinement of the grid around the wing. The denser grid to capture the boundary layer is clearly visible in the left picture. The refinement of the grid near the edges (leading edge, trailing edge and the tip) can be seen in the top view of the wing in the right picture.

be specified. The magnitude corresponds to the free stream velocity and the direction is defined by the angle of attack. The outlet is a pressure outlet in which the gauge pressure is set to zero (thus setting the boundary condition equal to the static pressure) and the direction is specified by the angle of attack. The symmetry-plane only requires the indication of being a symmetry-plane. The opposite side, from the symmetry plane was also defined as a symmetry plane. However defining it as a pressure outlet would have been better, but this has no influence on the results as it is far away from the wing. The wing itself is defined as a wall with a no slip condition, with the roughness height set to zero and the roughness constant equal to 0.5. This ensures a smooth surface.

The settings used in reference [20] are copied for the CFD-calculations. A steady, coupled, pressure based solver was selected with an absolute velocity formulation and a Green-

Gauss node based gradient option. Steady flow was selected due to the time independence of the flow. A pressure based solver was used because this solver is better in handling incompressible or mildly-compressible flows. As the problem at hand only involves very low speeds ($< 35m/s$ at sea level), compressibility effects are not expected. Under the pressure based solver one can specify the option of a segregated or a coupled algorithm for the pressure-velocity calculation. The coupled algorithm has the advantage of better convergence compared to the segregated algorithm, but this comes at the cost of more memory usage. The Courant number for this coupled algorithm is set to 10 and serves the purpose of stabilizing the calculation. This is a rather small Courant number, meaning that the calculation does not require a lot of implicit relaxation to establish a converging calculation.

Another option for the calculation is the velocity formulation. The purpose of this option is to minimize the numerical diffusion by selecting a relative or absolute velocity formulation. For the problem at hand the absolute formulation was selected as most of the flow in the domain is not rotating. The Green-Gauss node based gradient option was used because of its increased accuracy.

A second-order discretization was selected for the pressure, as this provides less numerical discretization errors, in the form of numerical diffusion, and thus better results for hexahedral grids. This however decreases the convergence but is compensated for by selecting the coupled algorithm. For the momentum and the turbulent viscosity, the discretization scheme was set to second order upwind both with an explicit relaxation factor of 0.75, to stabilize the calculation. In case of unstable calculations this number can be lowered to 0.5.

The Spalart-Allmaras model was used for the turbulence model. This is a RANS-based turbulence model with a single equation linear eddy viscosity model. It was because it has several advantages for the calculations under consideration:

1. It is designed for aerospace applications, involving wall bounded flows.
2. It is a one-equation model which does not require a lot of computational effort.
3. Has proven to work very well for wings, as clearly shown in reference [20].

The turbulence specification method for the boundary conditions was set to the turbulence viscosity ratio, whose value was set to 40. The value of this ratio has a small effect on the drag and no effect on the lift. The difference in the drag coefficient between a viscosity ratio of 1 and 40, was only 0.001. Results obtained with a turbulence viscosity ratio of 40 appeared to be better compared to reference [20] and was thus selected.

Comparison

Several single tapered wings with carefully selected shapes were processed using Fluent. The names of the wings relate back to their shape, e.g. wing201000, refers to a wing with 20 degree sweep, a taper ratio of 1 and a twist of 0 degrees. So the first two numbers refer to the sweep angle, the following to define the taper ratio times 10, and the last two are the linear twist angle, between the root chord and the tip chord, times 10.

The wing shapes tested using CFD are:

- wing001000: $\Lambda = 0^\circ$, $\lambda = 1$, $\delta = 0^\circ$, $A = 3$
- wing000500: $\Lambda = 0^\circ$, $\lambda = 0.5$, $\delta = 0^\circ$, $A = 3$
- wing000300: $\Lambda = 0^\circ$, $\lambda = 0.3$, $\delta = 0^\circ$, $A = 3$
- wing201000: $\Lambda = 20^\circ$, $\lambda = 1$, $\delta = 0^\circ$, $A = 3$
- wing401000: $\Lambda = 40^\circ$, $\lambda = 1$, $\delta = 0^\circ$, $A = 3$

See appendix B for detailed geometry descriptions. The CFD calculations were performed at a constant velocity of $20m/s$, corresponding to a root Reynolds number of 232000. The aspect ratio was taken constant such that only the viscous effects on the drag could be observed. The induced drag would change significantly with changing taper due to the change in aspect ratio. The span was reduced to compensate for the loss in surface area, while the root chord remained the same.

The first quasi-3D validation is its capability of estimating the maximum lift over drag ratio and its corresponding lift coefficient.

Table 4.1: Comparison of $(C_L/C_D)_{max}$ and its corresponding lift coefficient, between CFD and the quasi-3D method.

	CFD		Quasi-3D		$(C_L/C_D)_{max}$ - error [%]
	$(C_L/C_D)_{max}$	at C_L	$(C_L/C_D)_{max}$	at C_L	
Wing001000	11.91	0.336	12.11	0.338	1.68
Wing000500	11.48	0.333	11.82	0.34	2.96
Wing000300	11.23	0.328	11.66	0.396	3.83
Wing201000	12.07	0.338	12.08	0.331	0.08
Wing401000	12.17	0.319	11.93	0.305	-1.97

From table 4.1 it is clear that the absolute value of the maximum lift over drag ratio, is accurate within 4%. The error increases with decreasing taper ratio, but the gradient of the maximum lift over drag ratio with respect to the taper is pointing in the correct direction (see figure 4.16). The gradient for the quasi-3D method is not as large as for the CFD-calculations. The decrease in the $(\frac{C_L}{C_D})_{max}$ with decreasing taper ratio is caused by the decrease in the overall wing Reynolds number. This causes the profile drag to increase as the boundary layer around the wing thickens.

The absolute values of $(\frac{C_L}{C_D})_{max}$ for wings with varying sweep and no taper show results closely resembling the CFD-results. The gradient however proves to be a problem, as they are opposite to each other. The CFD-results suggest an increasing $(\frac{C_L}{C_D})_{max}$ with increasing sweep while this is not the case for the quasi-3D calculations (see figure 4.17). The gradient in both cases is very small. Dealing with flying wings will nevertheless require some sweep to establish the correct moment coefficient through twisting. Future research might focus on this to improve the gradient such that non-flying wing optimizations are not effected too much by this problem.

In the following sections results for every wing under consideration, will be discussed in detail.

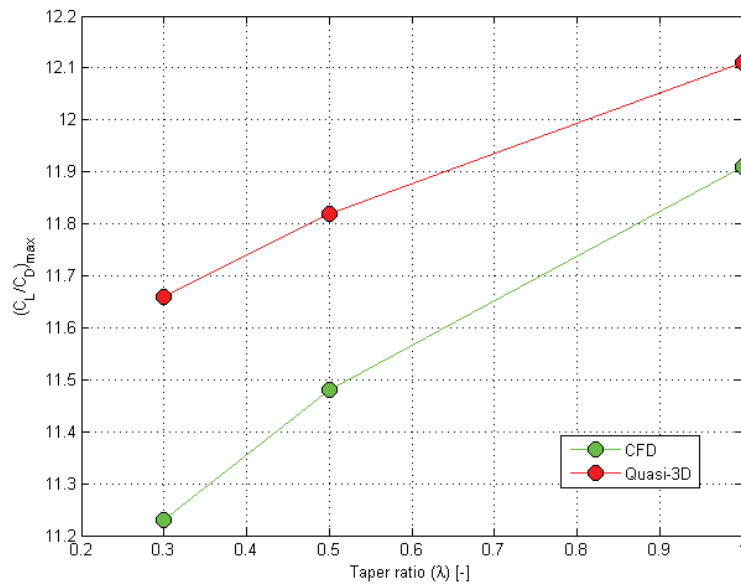


Figure 4.16: Variation of $(\frac{C_L}{C_D})_{max}$ against the taper ratio.

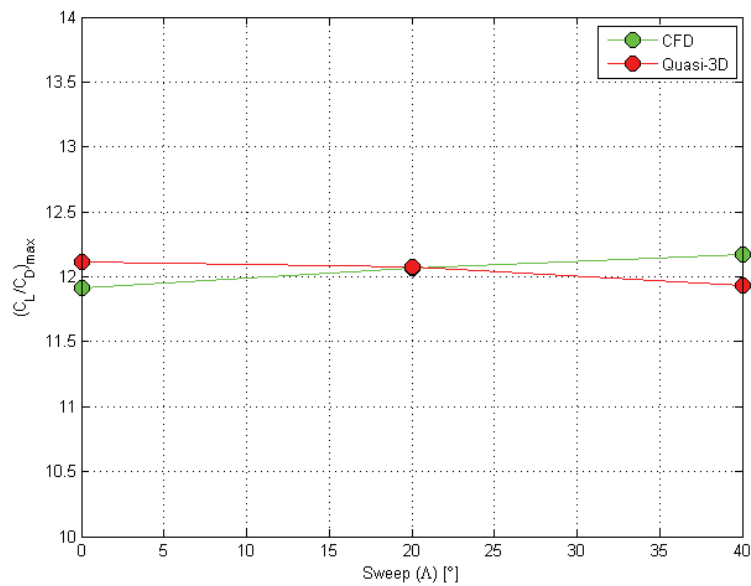


Figure 4.17: Variation of $(\frac{C_L}{C_D})_{max}$ against the sweep.

Wing001000

There is a close fit between the CFD and the quasi-3D results as can be seen in figure 4.18. At $\alpha = 0$, there is a small difference in the lift ($\Delta C_L = 0.0067$) and in the drag ($\Delta C_D = -0.0011$). The differences in the lift and drag graphs are clearly visible in the lift over drag ratio of graph (C). The overestimated lift and the underestimated drag amplify each other in the lower regions of the graph. However the underestimated lift gradient and the overestimated drag gradient, in graph (A) and (B), causes the lift over drag ratio to be slightly underestimated for $\alpha > 7.5$. From graph D it can be seen that the induced drag is slightly overestimated. The $(\frac{C_L}{C_D})_{max}$ however is very close to the one predicted by Fluent and is located at about the same lift coefficient (see plot (D) and table 4.1)

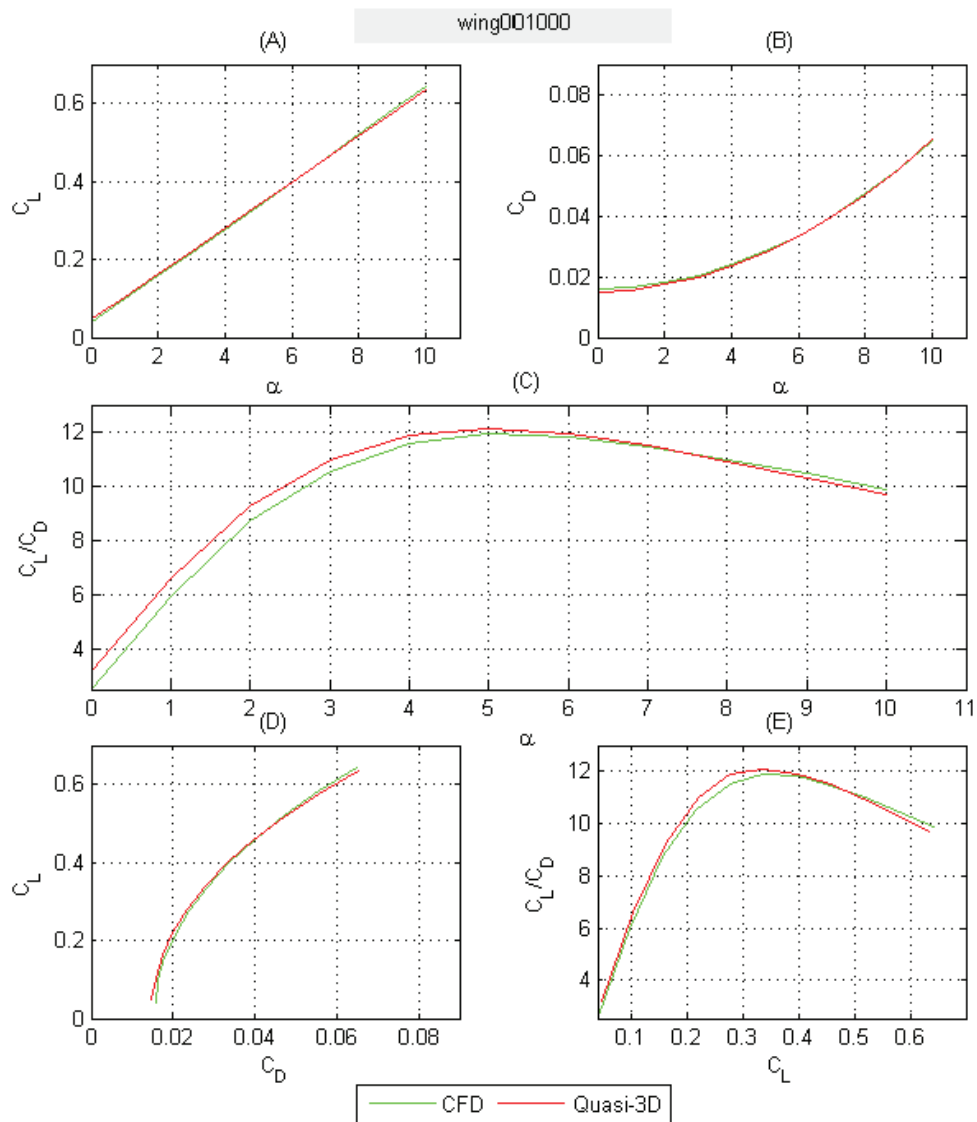


Figure 4.18: Validation plot for wing001000.

Wing000500

This wing shows the same difference as for wing001000 concerning the lift curve, namely the lift curve slope is less steep and the lift is a bit higher at $\alpha = 0$ for the quasi-3D calculation. The drag curve in figure 4.19(B) shows that at $\alpha = 0$ the drag coefficient is exactly the same while the gradient is a bit underestimated. These differences cause the lift to drag ratio in graph (C) to be overestimated in the complete alpha range. The drag however seems to increase nicely with the lift coefficient (see graph (D)).

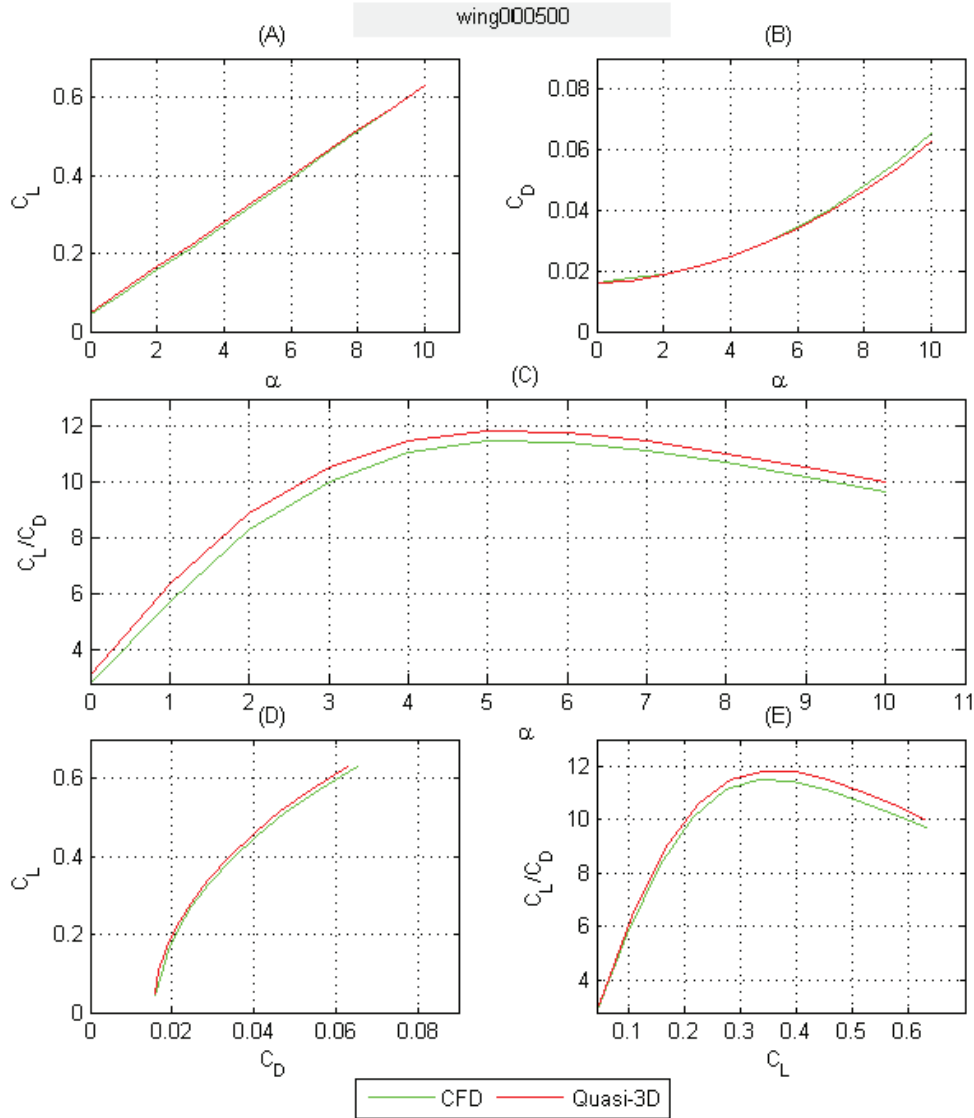


Figure 4.19: Validation plot for wing000500.

Wing000300

The estimated lift curve slope appears to be the same as for the CFD results. The dissimilarity in lift coefficient at $\alpha = 0$ is almost negligible ($\Delta C_L = 0.003$). The trend of a increasing underestimation of the drag curve slope with decreasing taper ratios is also observed for this wing, as can be seen in figure 4.20(B) and (D). At the same time, the drag at $\alpha = 0$ is also a bit to low ($\Delta C_D = 8 \cdot 10^{-4}$). These two differences cause the lift over drag ratio to be overestimated with a growing error towards larger angles of attack. From graph (D) it can be seen that the induced drag is underestimated. The maximum lift over drag ratio also appears to be estimated a slightly higher lift coefficient, as can be observed in table 4.1 and graph (E).

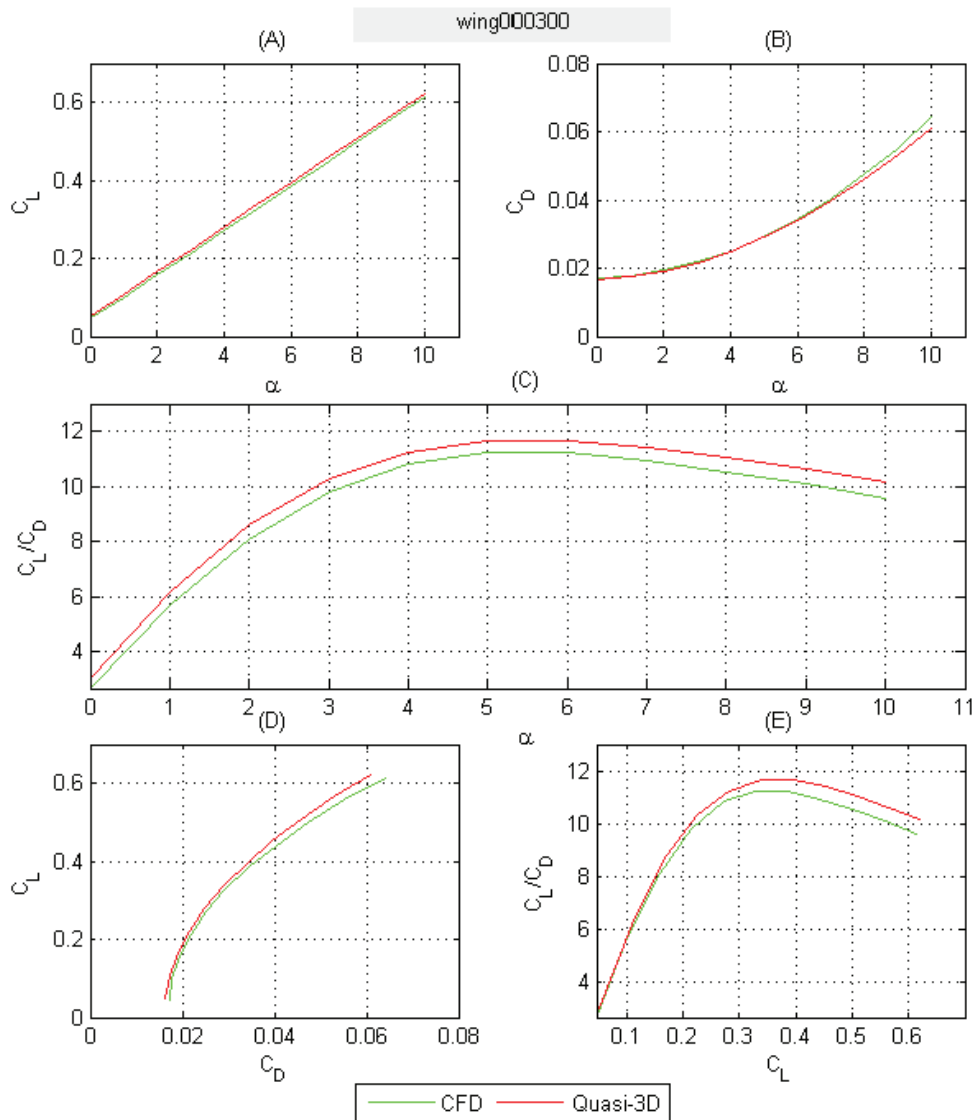


Figure 4.20: Validation plot for wing000300.

Wing201000

As for wing001000 the lift gradient is underestimated, but the lift coefficient at $\alpha = 0$ is only slightly overestimated ($\Delta C_L = 0.0027$). The drag slope in figure (B) seems to follow the CFD results quite nicely however when looking at plot (D) it can be seen that the induced drag is slightly overestimated. The lift over drag curve in graph (C) shows an extremely nice fit at and around the maximum $(\frac{C_L}{C_D})_{max}$. The C_L location of this maximum $(\frac{C_L}{C_D})_{max}$ is very close, as can be seen in graph (E) and table 4.1.

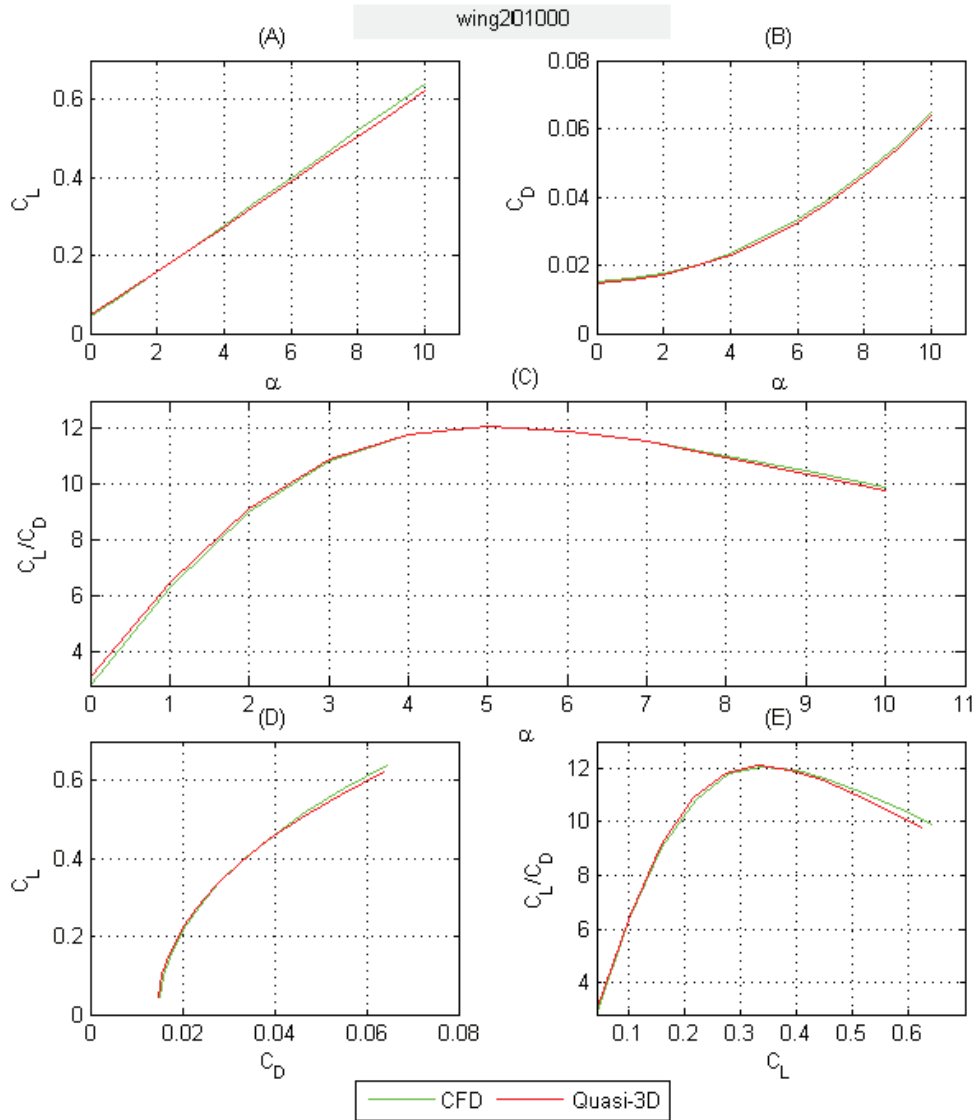


Figure 4.21: Validation plot for wing201000.

Wing401000

As for the other wings with taper ratio 1, the lift curve slope is underestimated. With increasing sweep a decreasing trend in the lift coefficient at α_0 , with respect to the one obtained from CFD, can be observed. The drag curve slope in graph (B) is too low which is a consequence of the lower lift at the same angle of attack. The induced drag however shows a nice fit in figure (D). The overall underestimation of the lift and the overestimation of the drag in the lower α -range cause an underestimation of the lift over drag ratio. The error decreases at higher angles of attack (see graph (C)) as both the lift and the drag are underestimated at these angles. Graph (E) shows a more constant difference in $(\frac{C_L}{C_D})$, and it can be seen that the C_L location of $(\frac{C_L}{C_D})_{max}$ is predicted accurately.

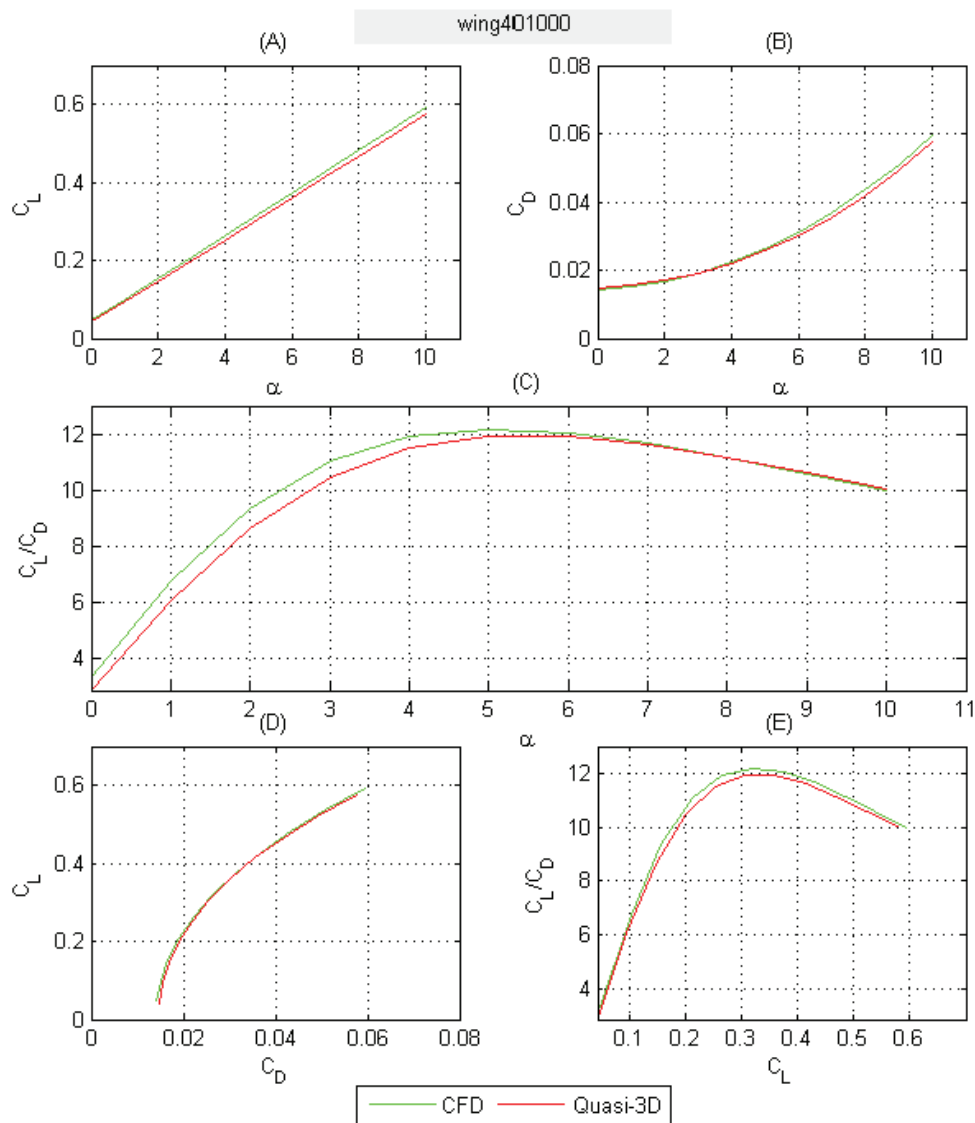


Figure 4.22: Validation plot for wing401000.

4.3.2 Validation with Wind Tunnel Results

The wind tunnel measurements for validation were retrieved from old NACA reports, reference [5] and [6]. Again several wings were selected to define the gradient of $(\frac{C_L}{C_D})_{max}$ with respect to the sweep and to establish the accuracy for higher aspect ratios. The wings all have aspect ratios higher than the once defined for the CFD-validation. Like in the previous section, the name of the wing reveals information about the geometry:

- NACA2400: $\Lambda = 0^\circ$, $\lambda = 0.5$, $\delta = 0^\circ$, $A = 6$
- NACA24150: $\Lambda = 15^\circ$, $\lambda = 0.5$, $\delta = 0^\circ$, $A = 6$
- NACA24300: $\Lambda = 30^\circ$, $\lambda = 0.5$, $\delta = 0^\circ$, $A = 6$
- NACA243085: $\Lambda = 30^\circ$, $\lambda = 0.5$, $\delta = 8.5^\circ$, $A = 6$
- NACA3-10-18: $\Lambda = 0^\circ$, $\lambda = \frac{1}{3}$, $\delta = 0^\circ$, $A = 10$

The first four wings start their name number with 24 which refers to the airfoil used, namely a NACA2415 for the root and a NACA2409 for the tip. The taper ratio of these wings remains unchanged, while the sweep (referred to by the following number(s)) and twist (referred to by the last number(s)) are the only geometric variables. The first number in the NACA3-10-18, refers to the inverse of the taper ratio while the second number indicates the aspect ratio. The last number refers to the root airfoil thickness. This root airfoil is a NACA23018 and the tip airfoil for this wing is the NACA23009. Detailed dimensions of these wings can be found in appendix B.

The NACA wind tunnel results date back to the end of the thirties of the previous century, during which the subsonic NACA tunnels had a high turbulence level. This is why, like for the comparison to CFD, the boundary layer is forced to transition at 5% of the airfoil chord. The velocity for the quasi-3D simulation was set at $272m/s$ such that the root Reynolds number was about $3.2 \cdot 10^6$, the same as for the wind tunnel data.

Lets first take a look at the performance of the quasi-3D method in estimating the $(C_L/C_D)_{max}$ and its corresponding C_L .

Table 4.2: Comparison of $(C_L/C_D)_{max}$ and its corresponding lift coefficient, between experimental results and the quasi-3D method.

	Experimental		quasi-3D		$(C_L/C_D)_{max}$ -error [%]
	$(C_L/C_D)_{max}$	at C_L	$(C_L/C_D)_{max}$	at C_L	
NACA2400	22.31	0.4023	21.97	0.394	-1.52
NACA24150	22.52	0.437	21.96	0.389	-2.49
NACA24300	22.67	0.4221	21.95	0.437	-3.18
NACA243085	22.3	0.3869	21.97	0.399	-1.48
NACA3-10-18	26.15	0.51	26.48	0.543	1.26

It is clear, from table 4.2, that the errors for $(C_L/C_D)_{max}$ are rather small ($< 3.5\%$), however for the swept cases they are bigger than when compared to CFD. Another interesting point is that the $(C_L/C_D)_{max}$ -gradient, against the sweep, is very close to

zero for the quasi-3D method, while the experimental gradient compares closely to the CFD results. The comparison of the quasi-3D results to the experimental results of $(C_L/C_D)_{max}$ for varying sweep can be seen in figure 4.23.

Table 4.2 also shows that the quasi-3D method works fine for higher aspect ratios and wings with a significant twist. The error remains in the same order of magnitude.

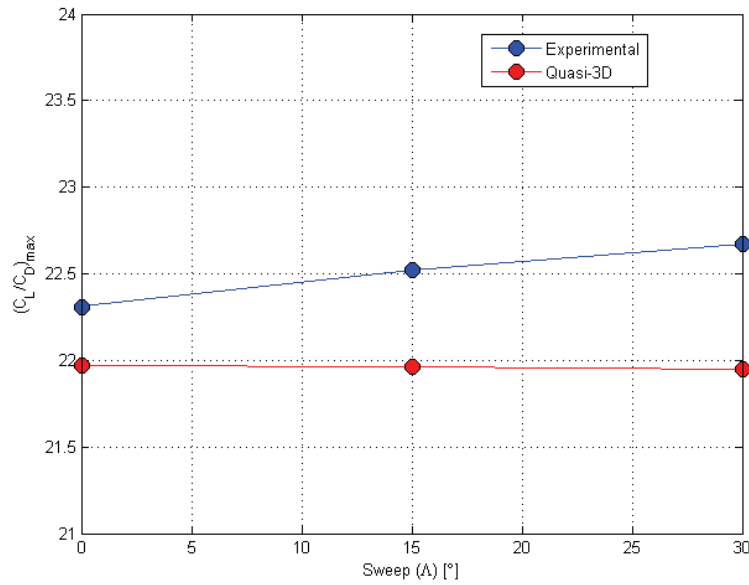
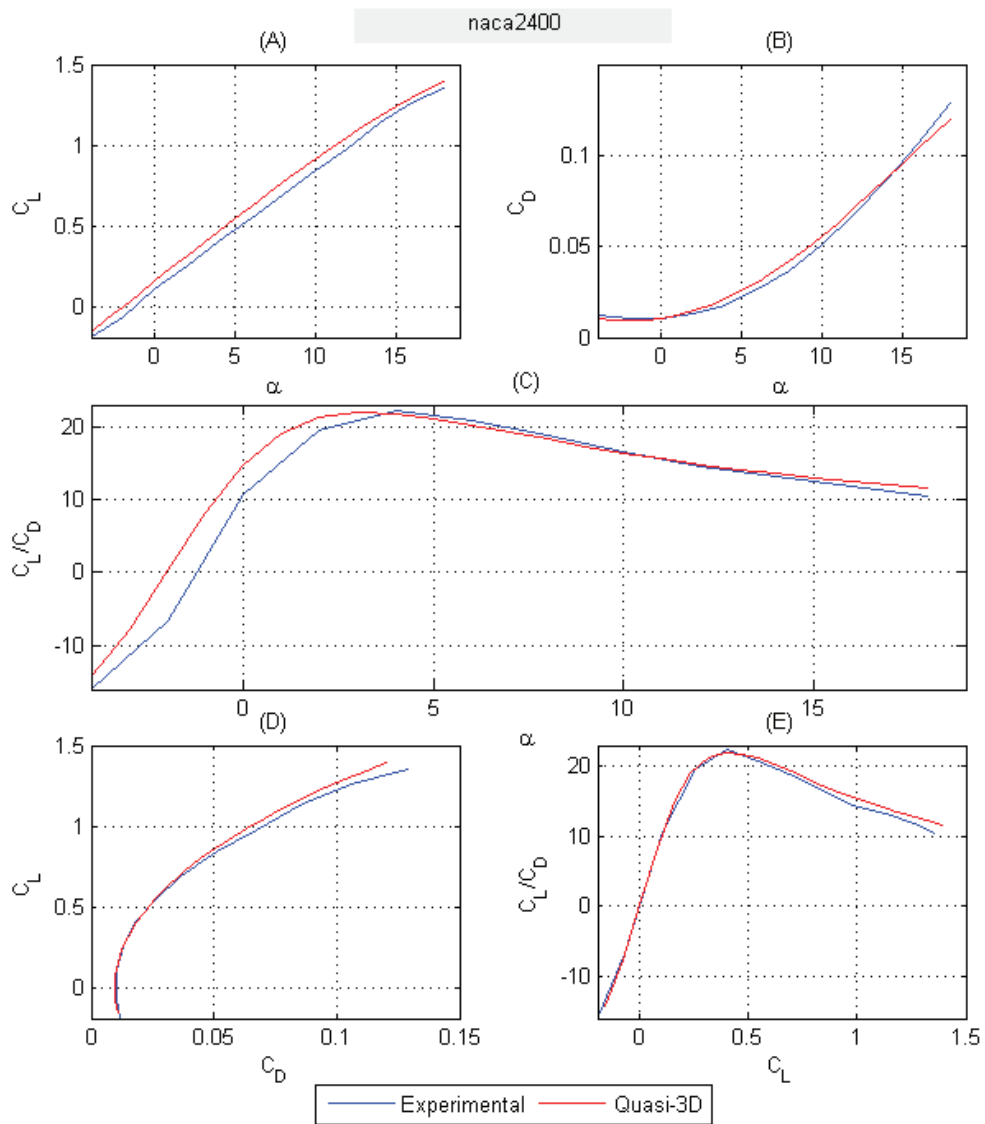


Figure 4.23: Variation of $(\frac{C_L}{C_D})_{max}$ against the sweep.

In subsequent sections, results for all wings under consideration will be discussed in more detail.

NACA2400

The lift curve, for this wing, has a slightly lower zero lift angle of attack ($\Delta\alpha_0 = 0.80^\circ$) which expresses itself through the complete curve. In figure 4.24(B) it can be seen that there is a shift in the minimum drag angle of attack. This is probably due to the shift observed in the lift coefficient as the difference is not seen in graph (D). In this same graph it can be seen that the induced drag is slightly underestimated. The shift in lift and drag, with respect to the angle of attack, is even better seen in plot (C) which is also shifted towards lower angles of attack. However when the lift over drag ratio is plotted against the lift coefficient, in plot (E), a nice fit is observed for the lower lift coefficients. Due to the underestimated induced drag, a slight overestimation is observed for the higher lift coefficients.

**Figure 4.24:** Validation plot for NACA2400.

NACA24150

The lift curve in figure 4.25(A) nicely fits the wind tunnel results only a minor shift in α_0 can be observed ($\Delta\alpha_0 = -0.21^\circ$). The difference in the CD-alpha curve is composed of a difference in the zero lift drag of $\Delta C_{D_0} = 8 \cdot 10^{-4}$, and an underestimated induced drag, as can be seen in graph (B) and (D). The lift over drag curves in figure (C) and (E) fit very nicely over the complete domain with only a minor underestimation of $(C_L/C_D)_{max}$, as can also be seen in table 4.2.

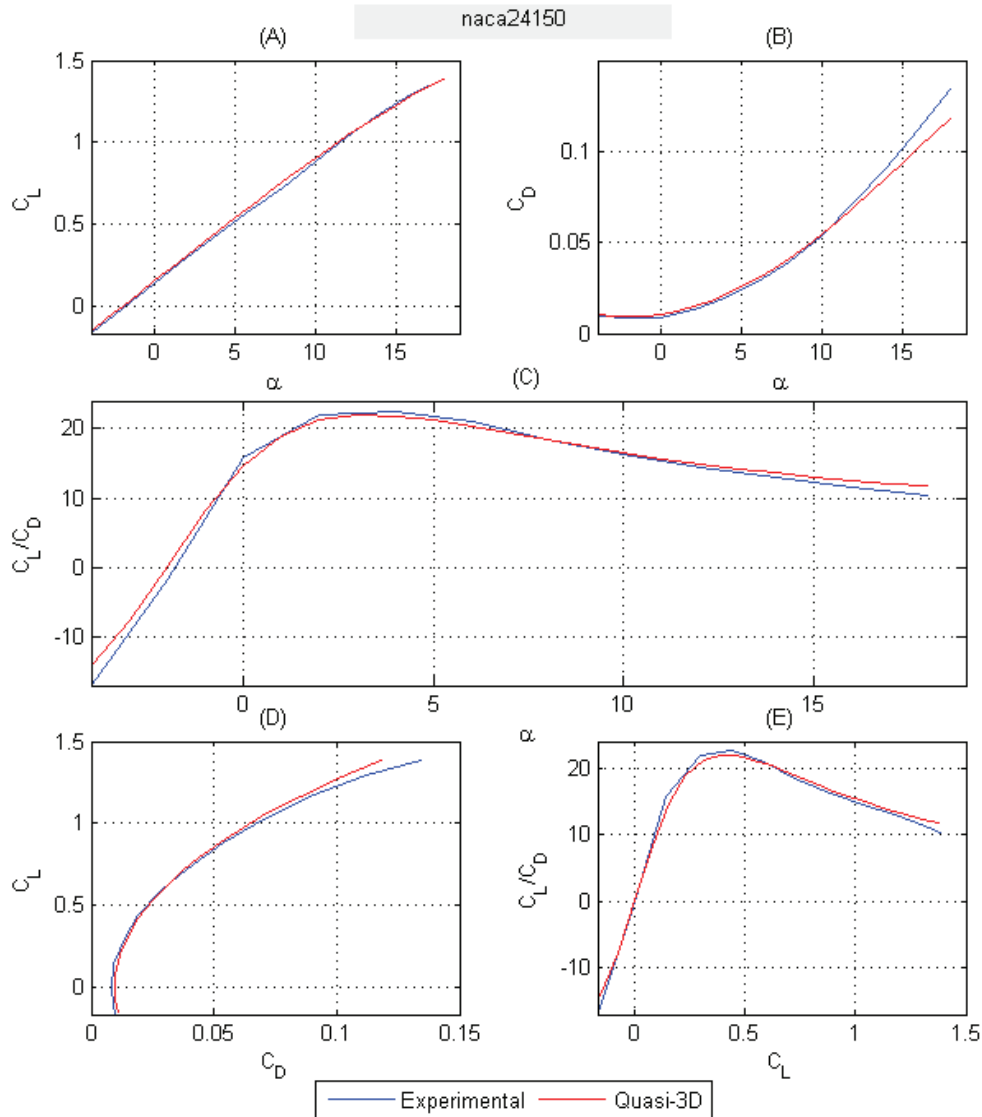


Figure 4.25: Validation plot for NACA24150.

NACA24300

The same conclusions as for NACA24150 can be drawn for this wing. A nice fit for the lift curve slope, but a slight shift in the zero lift angle of attack can be observed in graph (A). The drag is slightly overestimated at the point of no lift and the induced drag is slightly underestimated (see graph (B) and (D)). The lift over drag graphs in plot (C) and (E) are a bit too low at their maximum point and are slightly overestimated at higher angles of attack/lift coefficients.

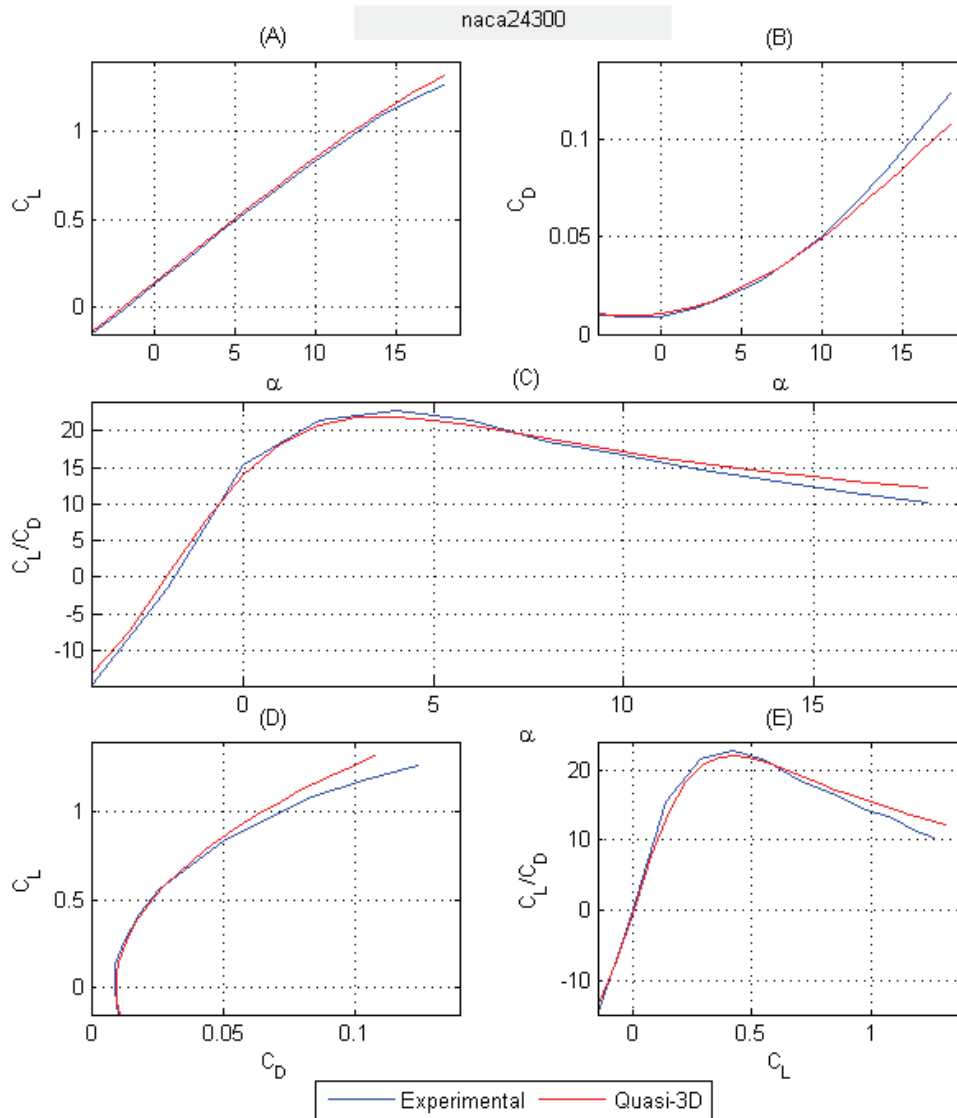


Figure 4.26: Validation plot for NACA24300.

NACA243085

This wing shows a very good fit in all graphs up to about $\alpha = 13^\circ$, after which the lift curve from the wind tunnel results shows a decrease in the lift curve slope. This is probably due to partially separated flow on the wing. The induced drag for this wing is nicely estimated as can be seen in graph (D). This shows that the aerodynamics for wings with a large amount of twist are nicely estimated using the quasi-3D method.

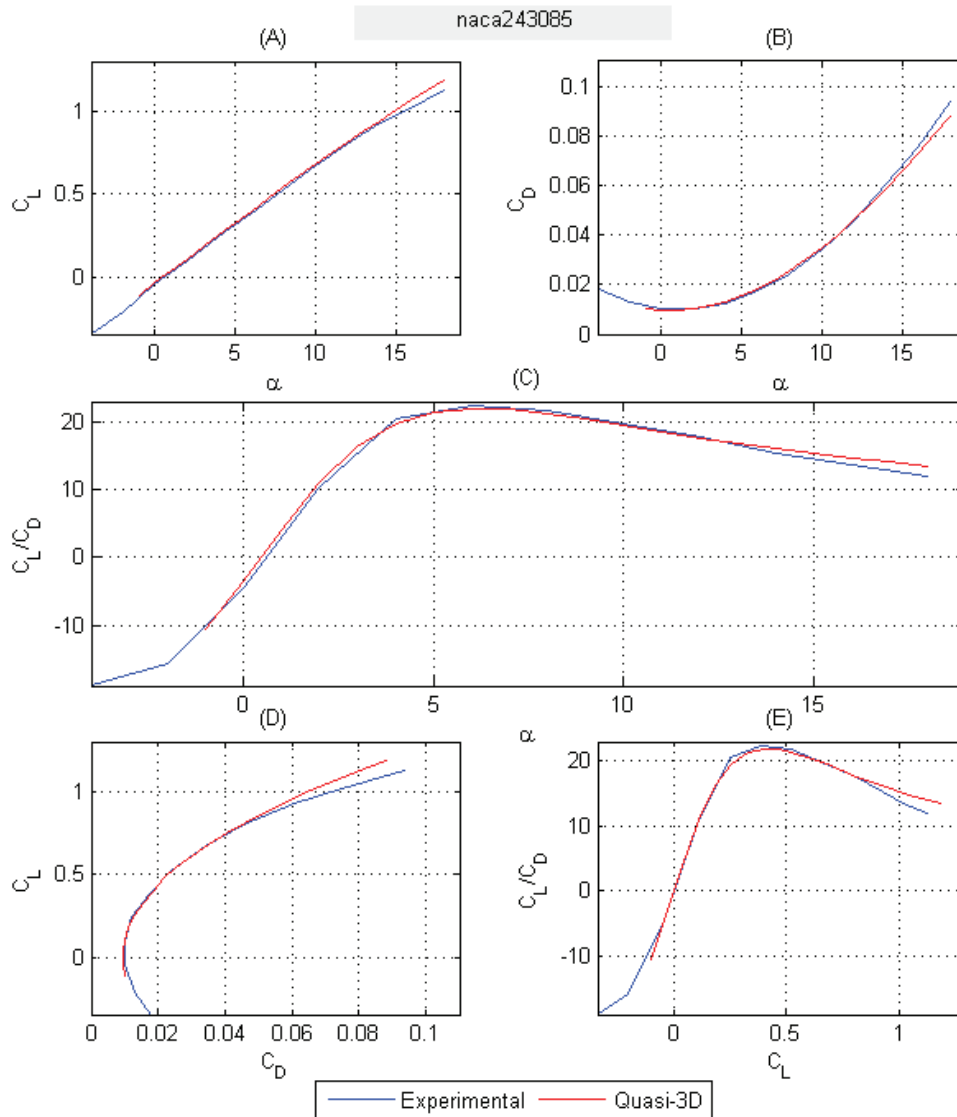


Figure 4.27: Validation plot for NACA243085.

NACA3-10-18

Up until this point, the wings used in the validation had a rather low aspect ratio (CFD validation $A = 3$, Experimental validation $A = 6$). The NACA3-10-18 was selected because of its higher aspect ratio ($A = 10$). The results for this wing, as seen in figure 4.28, show no larger errors as for the other wings. The only difference with respect to the other NACA-wings, is that the maximum lift over drag ratio is slightly overestimated instead of underestimated. The induced drag for this wing also shows a slight underestimation as can be seen in graph (D).

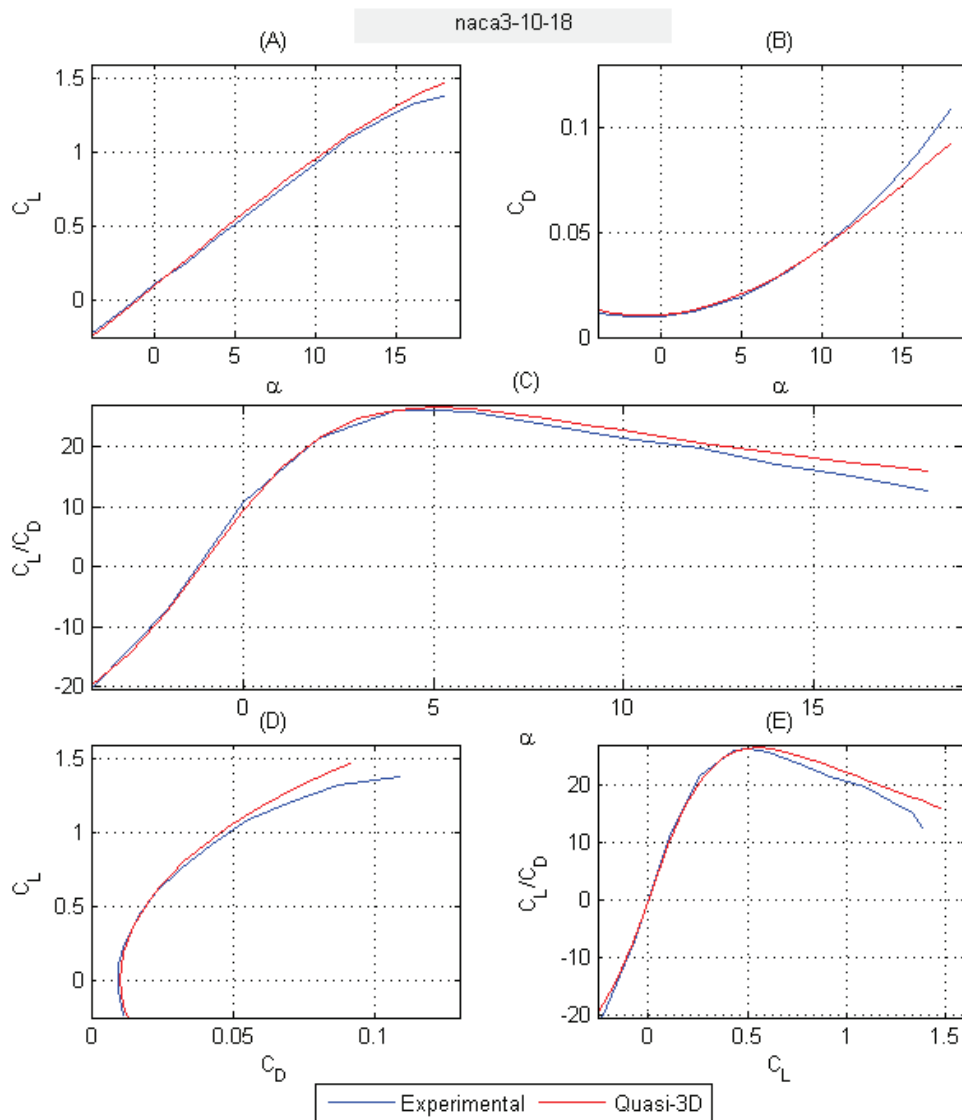


Figure 4.28: Validation plot for NACA3-10-18.

4.3.3 General Validation Conclusions

Some general remarks after the comparison of the quasi-3D method to CFD and wind tunnel results are in place.

It was noted that the maximum lift over drag ratio is estimated within a bound of 4% accuracy. This is very acceptable knowing that a small difference in the hard to determine drag coefficient, makes a large difference in the lift over drag ratio.

In general it can be seen that the error in $(\frac{C_L}{C_D})_{max}$ is increasing with decreasing taper ratio. This is mostly caused by an under prediction of the induced drag. However the gradient of the maximum lift over drag ratio against the taper is estimated rather good and are unlikely to produce problems when using the optimizer.

The error for the sweep has the tendency to increase for increasing sweep, but remains within a bound of 3.5% even for a sweep of 40°. When looking at the CFD-comparison the induced drag seems to be overestimated, while when compared to wind tunnel results, the induced drag is underestimated by the quasi-3D method. This difference might be caused by the difference in aspect ratio. The wings used for the CFD-validation have an aspect ratio of three, requiring a correction for tip-vortex effects on the wing. This is not the case for the NACA-wings.

A point of concern is the gradient of $(\frac{C_L}{C_D})_{max}$ against the sweep. The quasi-3D method does not match the gradients of the CFD and wind tunnel Results, which in turn compare very well to each other. This will be a problem when optimizing with an optimization algorithm that relies on gradient information. The tailless aircraft under consideration are not as prone to this problem as they require a combination of sweep and twist to trim the aircraft. The higher the sweep the less twist required, which will push the gradient into the correct direction. On top of this the gradient observed in the validation data is rather small, as can be seen in figure 4.17 and 4.23.

A final remark is the fact that the accuracy of the quasi-3D method is not affected by larger aspect ratios nor by a lot of twist.

4.4 Qualitative Comparison of the Quasi-3D Method to Fluent

The reasons for developing the quasi-3D method, as mentioned in the beginning of this thesis, are:

- Reducing the time required for an aerodynamic evaluation of a wing.
- Having the ability to predict the viscous effects at low Reynolds numbers.
- Easy to generate a computational domain in the form of a mesh.

Now it is interesting to verify if these requirements are met, and to see if and how much they have improved.

4.4.1 Time Required for an Aerodynamic Evaluation

The comparison made here will be between the time it takes for Fluent and the quasi-3D method to present their results. Both calculations were performed on a HP dv 9700 Notebook PC, with a Intel(R) Core(TM)2 Duo CPU T7250 Processor, 3GB RAM, and a Vista 32-bit operating system.

The time for an aerodynamic evaluation will be defined as follows: *The time passed between the start of the aerodynamic calculation and the presentation of the aerodynamic coefficients, for a single angle of attack.*

This definition excludes the construction and validation of the computational domain in the form of a mesh, and the time it takes to get the settings right in the tool used for the aerodynamic evaluation.

A Fluent evaluation with the grid and settings described in section 4.3.1, consumes on average 2 hours and 15 minutes. For the quasi-3D method this is about 1 minute.

A single objective evaluation, during the optimization, takes at least 9 aerodynamic evaluations. These are required to get trimmed and level flight. The optimization requires about 200 objective evaluations. This results in an optimization time of at least:

- Using Fluent: 168 days, 18 hours
- Using quasi-3D method: 1 day, 6 hours

This illustrates the fact that Fluent is very impractical to use for the optimization of the EMAN2009 aircraft, it would just require too much time. However one has to keep in mind that when new airfoils are used in the quasi-3D method an addition of about 3 hours is required to create the basic airfoil database. The optimizer is developed for low Reynolds numbers, whenever high Reynolds numbers are used the data needs to be added to the database increasing the time required to evaluate the aerodynamics with the quasi-3D method.

The reduction in time is definitely illustrated. It can even be stated that the quasi-3D method makes an optimization a practical option.

4.4.2 Low Reynolds Number Viscous Effects

Low Reynolds number effects in this report mainly refer to the laminar separation bubble and its influence on the aerodynamic forces. As the maximum lift over drag ratio is mostly obtained at lower lift coefficients one does not have to bother too much about viscous effects, like large areas of separated flow, that normally occur in the near stall region.

Using Fluent the easiest and fastest way to account for viscous effects is using RANS-models. They however do not predict the location of the transition point nor the effects of the laminar separation bubble. It would not be correct to state that the quasi-3D fully captures these effects, as they are influenced by the 3-dimensional flow, but it does at least take them into consideration through the viscous airfoil data.

4.4.3 Easy Generation of the Mesh

For Fluent the computational domain consists out of a volume mesh. This requires that a volume is defined around the wing which is then cut into smaller volumes creating the mesh. Producing a good mesh is important to obtain good results, requiring a denser mesh in certain parts of the volume. This, however, requires a lot of time and experience. Doing this automatically is rather difficult and does not ensure good meshes.

The quasi-3D method requires two meshes, one for the vortex lattice method and one for the airfoil calculations in Xfoil. The advantage of these meshes is the fact that they are surface meshes meaning that only the surface of the wing or airfoil needs to be meshed. Refining these meshes in the critical areas does not require a lot of experience. The construction of these meshes only need a limited amount of input. Changing these variables and validating the results, provides a feel for what kind of meshes work well and what inputs should be avoided. This experience can then be translated into a program that creates these meshes automatically while ensuring good results.

Wind Tunnel Experiments

The second part of the thesis work was to design, build and analyze the TU Delft competitor in the EMAV2009 endurance competition. This required a lot of practical work for which the author was assisted by a group of students performing their DAR-exercise on different parts of this practical work. The subjects of these different DAR-exercises are:

- Design and construction of the master molds for the EMAV2009 mini-UAV
- Building the production molds and the prototype model for the EMAV2009 mini-UAV
- Designing and building a wind tunnel force balance for mini-UAV wind tunnel force measurements
- Design of the propulsive system and selection of the energy source for the EMAV2009 mini-UAV

These exercises were closely monitored, such that they could neatly fit into this research. All these topics will be addressed in this chapter¹ to a level of detail suited for this report. Some later stage changes in the designs, produced during these exercises, will be explained. Reference will be made to the DAR-exercise reports for more detailed information on their topic.

Wind tunnel experiments were performed in the scope of analyzing the aircraft for the EMAV2009 and to validate the quasi-3D method. Two different kinds of tests are required for this purpose. They consist out of aerodynamic force measurements and boundary layer visualizations. These visualizations are required to see and understand what is happening inside the boundary layer at low Reynolds numbers. The wind tunnel experimental setup will be discussed first in section 5.1 after which the results of the experiments will be presented in section 5.2.

¹Except for the design of the propulsion system which is explained in section 6.2.2

5.1 Wind Tunnel Measurement Setup

Two wind tunnel campaigns were performed for this research. During these campaigns the two prototypes for the competition aircraft were tested. One of them had a manually designed wing while the second one was created with a first version of the optimization program.

The experiments were performed in the low speed low turbulence wind tunnel of the TU Delft. This facility is equipped with a six degree balance system. The resolution of this system is very high, but not high enough to measure the small forces experienced by mini-UAV's. This was the reason for designing and building a new balance dedicated to measurements on mini-UAV's.

The wind tunnel models were created at the MAVLab using the same techniques as for the competition aircraft, such that experience was gained in building mini-UAV's before building the competition aircraft.

The complete wind tunnel setup can be seen in figure 5.1.



Figure 5.1: Wind tunnel measurement setup.

5.1.1 The Low Speed Low Turbulence Wind Tunnel²

The TU Delft low speed low turbulence Tunnel (LTT) is a closed-throat single-return atmospheric wind tunnel. It achieves the low free stream turbulence levels through a large contraction ratio of 17.8. Its turbulence level is only 0.015% at 20m/s and 0.07% at 75m/s. The top speed of this tunnel is about 120m/s which it obtains with its six bladed fan and a 535 kW DC motor.

²Information obtained from reference [3]

The test section of the tunnel is interchangeable such that test preparations can be performed while the tunnel is running. The size of these test sections is 1.8m wide, 1.25m high and 2.6m long.

The measurement equipment, available at the LTT, consists of an electronic pressure scanner, a electronically read multi manometer, a six component balance and an infra-red visualization system. This infra-red system is the only one of interest to this work as it will be used for boundary layer visualizations. Force measurements will be performed using a newly created balance system explained in the following section.

5.1.2 Balance

As mentioned before, a new force measurement system was required for mini-UAV's as they experience far smaller forces than the average model tested in the LTT. The most critical of all forces is the drag force. The LTT force balance has a resolution of about $4 \sim 5gr$ which is not nearly high enough to accurately measure the lowest drag force on the prototype aircraft, which is about $27gr$. This was the reason to resort to a new force measurement system.

Hardware

The design and construction of the new force balance was performed during a DAR-exercise. The details of this design are presented in reference [33].

The balance hardware consists of two different parts, one is the force sensor and the other one is the yaw-pitch system. An of-the-shelf force sensor was selected based on several criteria.

- Maximum force and moment range
- Resolution
- Size
- Flexibility to use for several types of measurements

These criteria were all checked and it was decided to use the 6 axis “ATI Nano 17 SI-25-0.25” force transducer. This sensor has a resolution of $1/160N = 0.637gr$ for the 3 forces. This is considerably better for accurate drag and lift measurements than the available LTT-balance. A picture of the complete sensor system can be seen in figure 5.2. This figure shows the sensor, signal conditioner and the data acquisition card. Details on the Nano 17 sensor and its selection process can be found in reference [14] and [33]. A data sheet on the sensor can be found in appendix C.

The yaw-pitch system can be seen in figure 5.3. The purpose of this system is to set the angle of attack and the yaw angle during the wind tunnel measurements. Two digital servos were used to set the angles. However, this system has no feedback loop between the servo setting and the yaw/pitch-angle and thus requires a calibration before the tunnel tests start. During the calibration a table has to be created that couples the servo setting to a certain angle.

A pictures of the finished balance can be seen in figure 5.4.

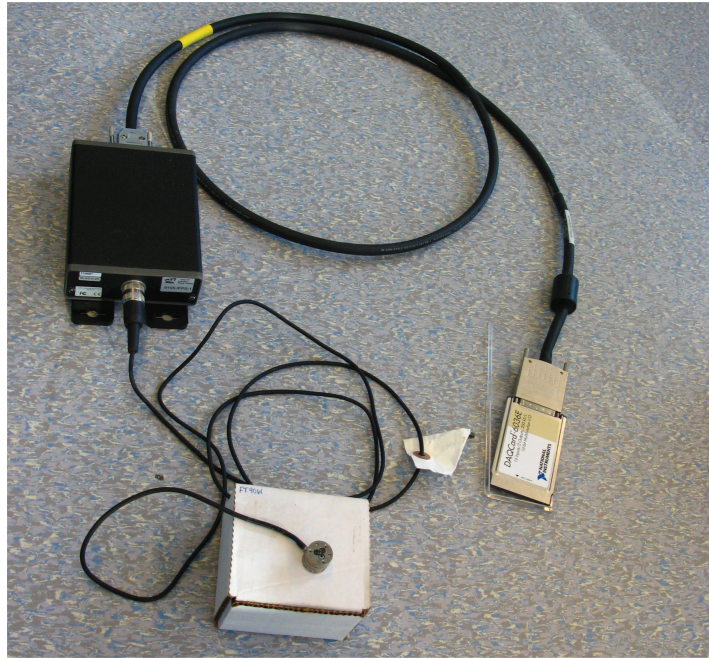


Figure 5.2: Nano 17 force/torque sensor system with data logging card.

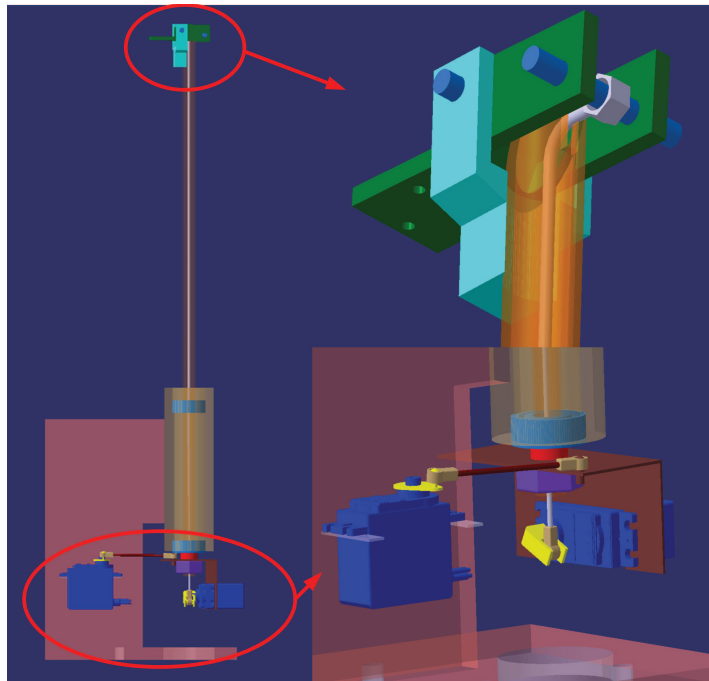


Figure 5.3: Wind tunnel balance yaw and pitch system.

Problems with the Force Balance

Some problems with the balance were discovered during the angle calibration process, and while performing the wind tunnel tests. These problems are only due to imperfections

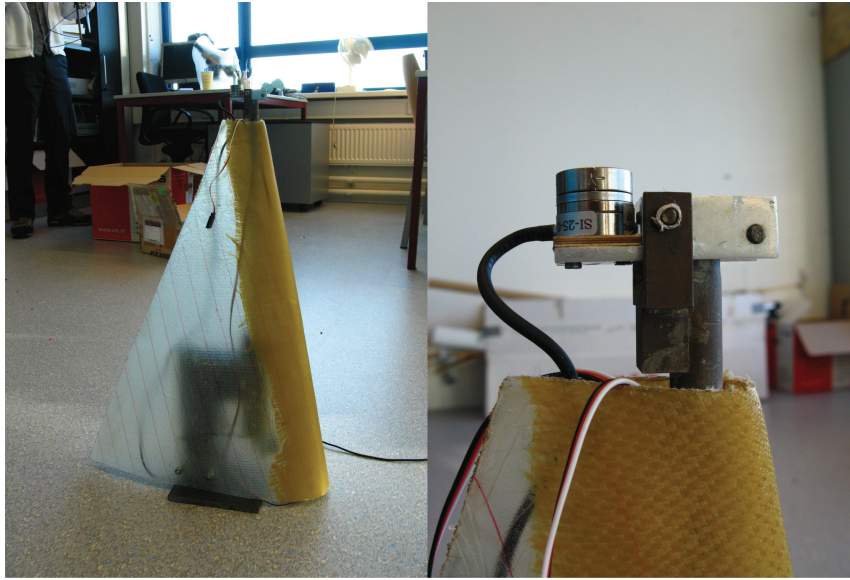


Figure 5.4: Finished yaw-pitch system with the sensor connected on top.

in the yaw-pitch system, the sensor was found to produce very good results. Setting the angles correctly proved to be hard due to several causes, summarized here:

- There was some mechanical play combined with friction on the connections between the servos and the rotating head of the balance.
- The digital servo potentiometer, which produces the feedback between the servo input and output, was located on the second to last gear. This results in the play between the last two gears, not being eliminated.
- No clear pitch and yaw angle indication was present nor a zero angle indication.
- During the wind tunnel tests the forces put on the system cause strain and thus misalignment with respect to the calibration (performed without forces on it).
- At high angles of attack the pitch servo was not strong enough.
- Construction of the balance was rushed in the final stages resulting in less accurate finishing.

However a simple solution to most of these problems would be a feedback-loop between the servo input and the angles at the head of the balance. This can be achieved by moving the potentiometer from within the servo to the pitch and yaw rotation axes. This way any discrepancy between the input and the output can be removed. These improvements are recommendations for future work and were not in place at the moment of the wind tunnel tests.

At this moment the servos in the balance are fast and medium strong, but it would be better to change them for slower servos with a higher hold force, or adding a servo gear box. An example of a servo gearbox option would be the SPG785A-BM (see figure 5.5).



Figure 5.5: SPG785A-BM servo gearbox.

The electronic-board connecting the computer to the yaw and pitch servo is a stripped down versions of an autopilot, which in essence is developed for controlling servos. The link between the computer and the servos is the only part that remained on it. The attitude sensors and GPS-receiver were removed as they served no purpose in the balance.

Software

Two software tools were developed for the wind tunnel measurements. One is used to log all data and to control the yaw-pitch servos on the balance, while the other one is used for post processing the measurements. At this point, real-time evaluation of the coefficients is not possible as both programs are not yet linked to each other, this is a recommendation for future work.

Balance control and data logging software

The DAR-exercise for the design of the propulsion system (see section 6.2.2) was expanded with the programming of the data-logging and yaw-pitch control of the balance. This resulted in a nice and easy to use program. Reference [14] should be consulted for a detailed discussion on the functioning of the program. A summary of this will be presented here.

The balance control and data logging software allows the user to control the servos for the balance, the aircraft servos for the elevons, and the aircraft motor. At the same time it provides the user with the ability to change the number of data sets logged at every measurement point, and the frequency of collecting data. The data is logged in a csv-file and contains information on:

- Sensor force and moment readouts
- Balance servo settings
- Aircraft servo settings
- Aircraft motor settings
- Motor current and voltage readouts

- Wind tunnel settings
- Atmospheric information

Some of the data are automatically extracted while others have to be manually provided by the user. An improvement for the future would be the automatic readout of the wind tunnel settings and atmospheric information, which at this point have to be manually entered for every measurement point.

Measurement Post-processing Tool

The sensor rotates together with the head of the balance and is thus always oriented in the aircraft body reference system. This must then be rotated back to the aerodynamic reference system. This is done using the post processing tool which was created by the author and will thus be explained here in more detail.

The input for this program exists of:

- Wind tunnel measurement file.
- A zero-run file. This is a file that contains sensor measurements for all angles, pitch and yaw, with the wind tunnel off. Subtracting these measurements from the “wind tunnel on” measurements ensures that the weight effects are taken removed and thus only aerodynamic forces are presented.
- A file with aircraft geometry information.
- The sensor pitch offset. This is the angle between the sensor horizontal and the zero angle of attack of the aircraft. (see figure 5.6)
- Servo calibration information. This information relates the servo input, saved in the wind tunnel measurement file, to an angle of attack and yaw angle.

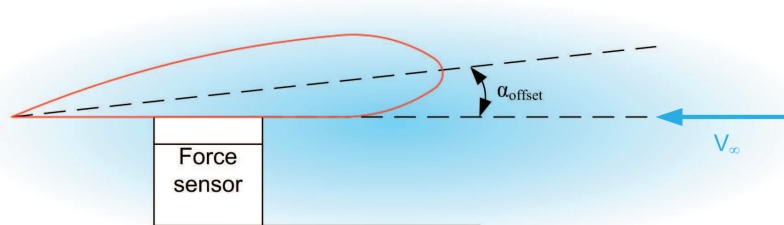


Figure 5.6: Definition of the pitch-offset angle.

The first step is to read the measurement and zero-run file, followed by averaging of the available data at each measurement point. The servo inputs for the zero-run file and the measurement file are then converted into angles. These angles are used to subtract the corresponding zero-run data from the measurement data. Once this is finished the data must be rotated from the sensor reference system, which is only rotated over α_{offset} with

respect to the aircraft body reference frame, towards the aerodynamic reference frame. Figure 5.7 visualizes the rotation between the two references systems. In matrix form this can be formulated as:

$$\begin{bmatrix} L \\ D \\ S^* \end{bmatrix} = \begin{bmatrix} \sin(\alpha - \alpha_{offset}) & 0 & \cos(\alpha - \alpha_{offset}) \\ -\cos(\alpha - \alpha_{offset}) \cos(\beta) & \sin(\beta) & \sin(\alpha - \alpha_{offset}) \cos(\beta) \\ -\cos(\alpha - \alpha_{offset}) \sin(\beta) & -\cos(\beta) & \sin(\alpha - \alpha_{offset}) \sin(\beta) \end{bmatrix} \begin{bmatrix} F_x \\ F_y \\ F_z \end{bmatrix} \quad (5.1)$$

$$\begin{bmatrix} N \\ L^* \\ M \end{bmatrix} = \begin{bmatrix} \sin(\alpha - \alpha_{offset}) & 0 & \cos(\alpha - \alpha_{offset}) \\ -\cos(\alpha - \alpha_{offset}) \cos(\beta) & \sin(\beta) & \sin(\alpha - \alpha_{offset}) \cos(\beta) \\ -\cos(\alpha - \alpha_{offset}) \sin(\beta) & -\cos(\beta) & \sin(\alpha - \alpha_{offset}) \sin(\beta) \end{bmatrix} \begin{bmatrix} T_x \\ T_y \\ T_z \end{bmatrix} \quad (5.2)$$

These aerodynamic forces are then converted into coefficients based on the velocity, wing surface and the atmospheric density.

These coefficients need to be corrected for solid and wake blockage, the 3D lift interference for small wings and the buoyancy effect. These corrections are however expected to be small as the model and the forces acting on it are small. Information for the wind tunnel corrections was obtained from reference [23],[31],[30] and [13].

The wind tunnel *blockage* creates an increase in the dynamic pressure as the mass flow through the tunnel must be constant while the presence of the model, balance and their wakes blocks part of the cross section. To calculate this effect one must determine the value of:

$$\epsilon_{SB} = \Delta V/V_\infty = \epsilon_{SB_w} + \epsilon_{SB_{fus}} + \epsilon_{SB_{bal}} + \epsilon_{SB_{wake}} \quad (5.3)$$

The velocity increase due to the wing and the balance can be calculated using the following equations (obtained from [23]):

$$\epsilon_{SB_w} = \frac{K_1 \tau_1 V_{wing}}{C'^{\frac{3}{2}}} \quad (5.4)$$

$$\epsilon_{SB_{bal}} = \frac{K_1 \tau_1 V_{bal}}{C'^{\frac{3}{2}}} \quad (5.5)$$

In these equation K_1 and τ_1 can be obtained from figure 5.8 and figure 5.9. The C' represents the wind tunnel cross-sectional area in the test section and V_{wing} and V_{bal} , are the wing volume and balance volume. The equation for the velocity increase for the fuselage is the following:

$$\epsilon_{SB_{fus}} = \frac{K_3 \tau_1 V_{fus}}{C'^{\frac{3}{2}}} \quad (5.6)$$

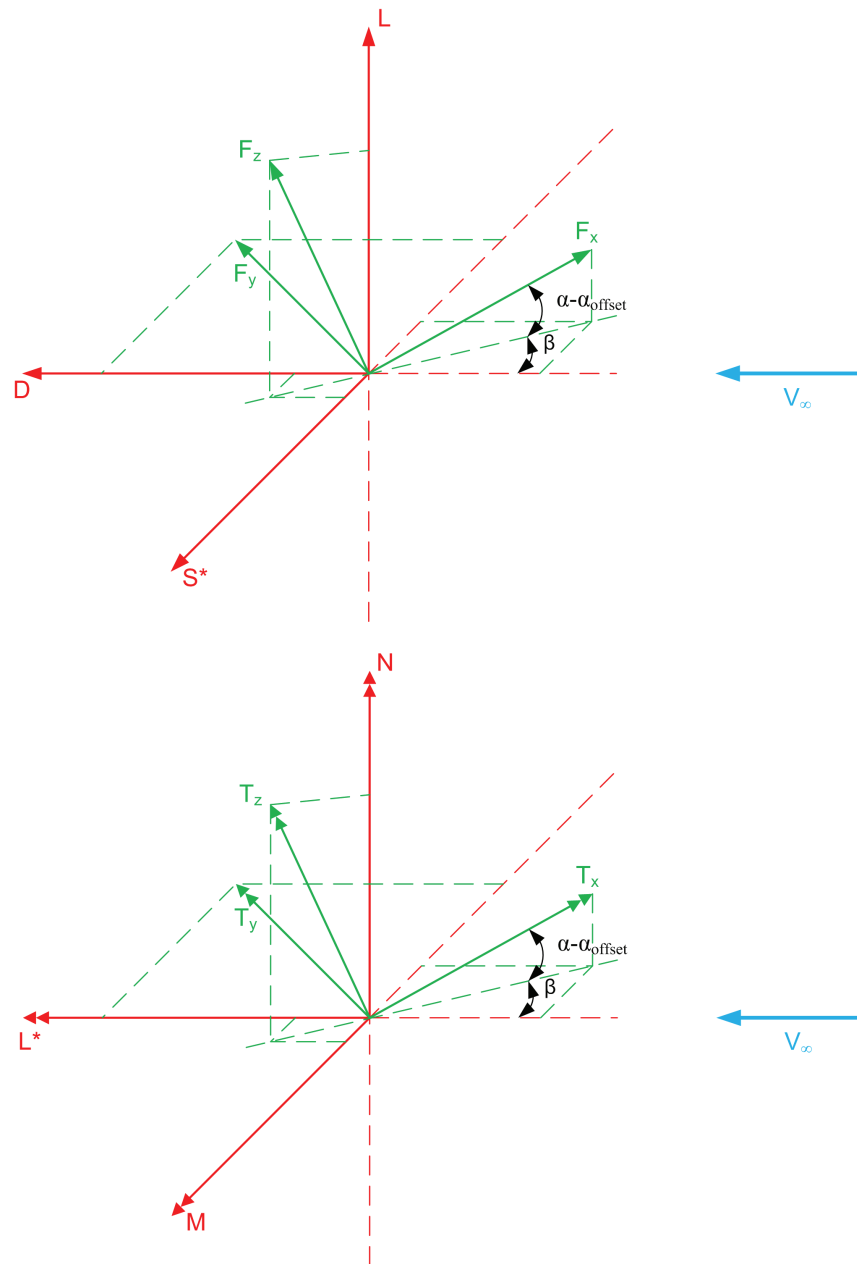


Figure 5.7: Visualization of the rotation between the sensor reference system and the aerodynamic reference system.

The wind tunnel cross-sectional area is once again represented by C' and K_1 and τ_1 are obtained from figure 5.8 and 5.9, respectively. The fuselage volume is represented by V_{fus} .

The wake blockage is the only value that still needs to be determined. For this equation

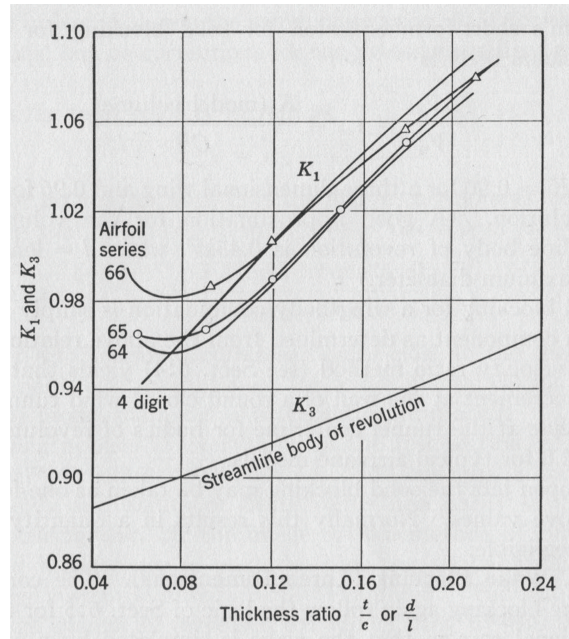


Figure 5.8: Values of K_1 and K_3 for a number of bodies (figure obtained from reference [23]).

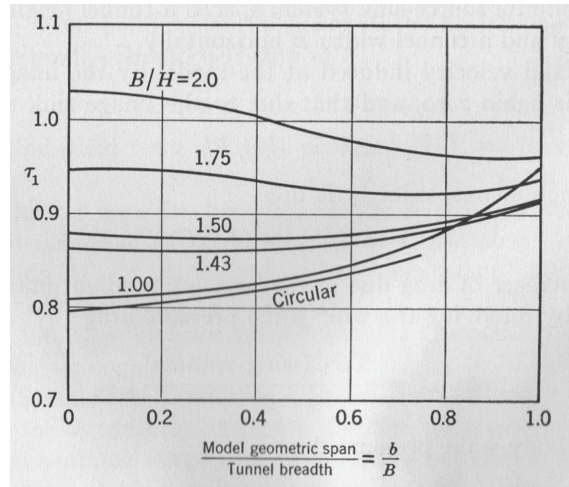


Figure 5.9: Values of τ_1 for a number of tunnel types. Use $b/B = 0$ for bodies of revolution (figure obtained from reference [23]).

5.7, obtained from reference [30], is used.

$$\epsilon_{SB_{wake}} = \frac{2}{4C'} C_{D_0} + \frac{1}{2} \frac{S}{C'} (2.8 - 0.068 \cdot A) (C_D - C_{D_i} - C_{D_0}) \quad (5.7)$$

In this equation C_D represents the uncorrected measured value of the drag coefficient. The C_{D_i} and C_{D_0} in this equation are determined by approximating the attached flow

part of the measured data with a full second order polynomial and can be calculated using equations 5.8 and 5.9. The A and S are the wing aspect ratio and the wing surface respectively. As before, C is the cross-sectional area of the wind tunnel test section.

$$C_{D_i} = a \cdot \left(C_L + \frac{b}{2a}\right)^2 \quad (5.8)$$

$$C_{D_0} = c - \frac{b^2}{4a} \quad (5.9)$$

In these equations a , b and c represent the coefficients of the second order polynomial approximation of the attached flow C_D ($C_D = a \cdot C_L^2 + b \cdot C_L + c$).

The velocity increases are then corrected for compressibility effects using:

$$\epsilon_{SB} = \frac{\epsilon_{SB_w} + \epsilon_{SB_{fus}} + \epsilon_{SB_{bal}}}{\beta^3} + \frac{\epsilon_{SB_{wake}}}{\beta'^2} \quad (5.10)$$

In this equation β' is determined with:

$$\beta' = \sqrt{1 - M'^2} \quad (5.11)$$

and M' is the mach number.

The last step is to apply the blockage effects to the force and moment coefficients, resulting in:

$$\begin{aligned} q_c &= q(1 + 2\epsilon_{SB}) \\ C_{D_{c_1}} &= C_D(1 - 2\epsilon_{SB}) \\ C_{L_{c_1}} &= C_L(1 - 2\epsilon_{SB}) \\ C_{S_{c_1}^*} &= C_{S^*}(1 - 2\epsilon_{SB}) \\ C_{N_{c_1}} &= C_N(1 - 2\epsilon_{SB}) \\ C_{L_{c_1}^*} &= C_{L^*}(1 - 2\epsilon_{SB}) \\ C_{M_{c_1}} &= C_M(1 - 2\epsilon_{SB}) \end{aligned}$$

The second correction is for the *3D lift interference* with the wind tunnel walls. The flow field around the aircraft has changed due to the presence of the wind tunnel walls. This can be modeled by mirroring the horseshoe vortices with respect to the wind tunnel walls and evaluating their effect on the flow around the model. A visual representation of this mirroring can be seen in figure 5.10.

This correction only has effect on the angle of attack and the aircraft moment coefficient and is modeled using equation 5.12 and 5.13 which are obtained from reference [30].

$$\Delta\alpha = \left(\delta_0 + \frac{c_{mac}\delta_1}{2\beta'h}\right) \cdot \frac{S}{C'} \cdot C_L \quad (5.12)$$

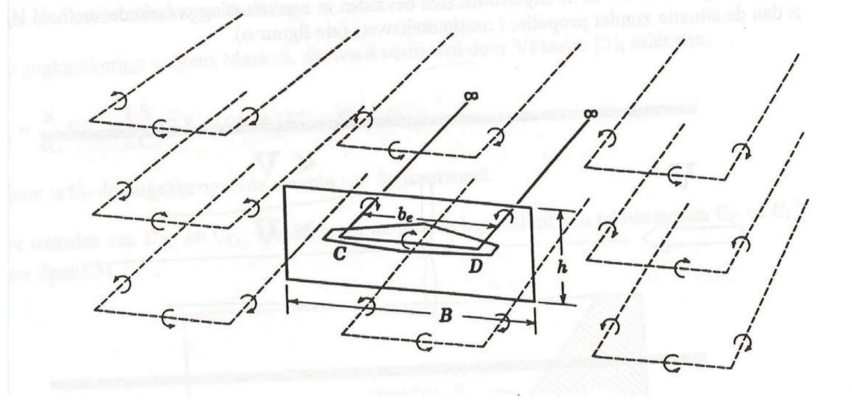


Figure 5.10: Principle of modeling the lift interference effect through mirroring horseshoe vortices with respect to the wind tunnel walls (figure obtained from reference [30]).

$$\Delta C_M = \frac{c_{mac} \delta_1}{16\beta' h} \cdot \left(\left(\frac{c_{avg}}{c_{mac}} \right)^2 + \frac{1}{3} (A \tan(\Lambda_{0.5}))^2 \left(2 - \frac{c_{avg}}{c_{mac}} \right) \right) \cdot C_{L_\alpha} \cdot \frac{S}{C'} \quad (5.13)$$

In these equations:

- c_{mac} is the wing mean aerodynamic chord
- β' is determined using equation 5.11
- h is the height of the wind tunnel
- S is the wing surface
- C' is the wind tunnel cross-sectional area
- C_L is the lift coefficient corrected for the solid blockage
- c_{avg} is the geometric average wing chord
- A is the wing aspect ratio
- $\Lambda_{0.5}$ is the the sweep at 50% of the chord
- C_{L_α} is the lift coefficient gradient against the angle of attack for the solid blockage corrected lift curve slope

The remaining two values to be determined are δ_0 and δ_1 , using:

$$\delta_0 = \frac{A_{tun}}{8\pi} \sum_{n=-\infty}^{n=\infty} \sum_{m=-\infty}^{m=\infty} (-1)^n \frac{m^2 A_{tun}^2 - n^2}{(m^2 A_{tun}^2 + n^2)^2}, \text{ excluding } n = m = 0 \quad (5.14)$$

$$\delta_1 = \frac{A_{tun}}{8\pi} \sum_{n=-\infty}^{n=\infty} \sum_{m=-\infty}^{m=\infty} (-1)^n \frac{m^2 A_{tun}^2 - 2n^2}{(m^2 A_{tun}^2 + n^2)^{\frac{5}{2}}}, \text{ excluding } n = m = 0 \quad (5.15)$$

In these equations A_{tun} represents the wind tunnel aspect ratio, defined as the tunnel width over height ratio. Equation 5.14 and 5.15 are obtained from reference [13].

These last two equations are the mathematical representation of the vortex mirroring and are obtained from reference [13], which should be consulted for further details.

The last correction that needs to be applied is the buoyancy effect, which only results in a change of the drag coefficient. This difference can be calculated using,

$$\Delta C_D = -(\epsilon_{SB_w} + \epsilon_{SB_{fus}} + \epsilon_{SB_{bat}})(1 + 0.4M^2) \left(C_D - \frac{C_L}{\pi A} \right) \quad (5.16)$$

, in which C_L and C_D are the measured lift and drag coefficient corrected for the solid blockage.

Applying the lift interference and buoyancy correction to the coefficients (which are already corrected for the solid blockage) and the angle of attack gives,

$$\begin{aligned} \alpha_c &= \alpha + \Delta\alpha \\ C_{D_{c2}} &= C_{D_{c1}} + \Delta C_D \\ C_{M_{c2}} &= C_{M_{c1}} + \Delta C_M \end{aligned}$$

After the corrections have been applied the measured forces have been properly converted into aerodynamic coefficients.

5.1.3 Wind Tunnel Model Construction

The model construction was divided over two DAR-exercises, one with the focus on the creation of the master molds while the other looked at the construction of the production molds and the wind tunnel model.³ The reports on these DAR-exercises, reference [9] and [11], were written such that they can be used as manuals for future projects. It was decided to use the same production technique for the wind tunnel models as for the airworthy aircraft. This decision was based on:

1. Knowledge and experience could be gained from construction of the wind tunnel models before producing the competition aircraft.
2. Costs would be lower if the molds for the competition aircraft could also be used for the wind tunnel models.
3. Using the same technique makes the wind tunnel results more representative.

³A master mold is used to make production molds. This way the expensive milled master mold does not get damaged during the production process.

Four molds were required for the construction of the prototype, two master molds for the wing and two production molds for the fuselage. These molds were milled out of Sieca block. This material is especially suited for making molds through a milling process. The creation of these molds required several steps:

1. Making a 3-dimensional CAD-drawing
2. Selecting the milling tools
3. Extracting a G-code from the CAD-drawing
4. Milling the molds

A very detailed description of the complete process is provided in reference [9].

The second part of the construction process is the production of the wind tunnel model itself. The first step was extracting production molds from the wing master molds. This proved to be a rather time-consuming task as the production molds are built up in layers which all require a certain time to dry. The lessons learned from this was that for small aircraft with small production volumes it is better to directly mill production molds. The time it takes to extract production molds from master molds is more expensive than the cost of milling a production mold when a cnc-milling machine is available.

The construction of the wing and fuselage can be started, after the preparation of the molds with the required sealer and release agent (see figure 5.11). Both the fuselage and the wing were made from composite materials using wet hand layup and vacuum-bagging. The wing was built up out of several layers, starting with a coating, then a $36\text{gr}/\text{m}^2$ Kevlar fiber on the outside, followed by a 1mm thick Rohacell core for skin stiffness and the inside layer was a $50\text{gr}/\text{m}^2$ glass fiber. The two wing shells were then joined together with a single spar for bending stiffness. The torsional stiffness was established through the torsion box created by the wing leading edge, the wing upper and lower skin and the spar.



Figure 5.11: Wing, upper and lower surface, production molds in the process of being prepared for production.

The fuselage and tail were joint together in one mold but required two steps to make. The first one was the construction of the tail which consisted of 3 layers, an outside $50gr/m^2$ glass fiber layer, followed by a $1mm$ thick Rohacell core and the inside was finished with another layer of glass fibers. Once the tail was ready the fuselage could be created in 1 step using the technique of inflating a bladder inside the mold. The fuselage was constructed from $110gr/m^2$ Kevlar skin with a second layer of the same material as reinforcements in the nose and in lengthwise direction of the fuselage.

For further details on the wind tunnel model construction, see reference [11].

The construction of the fuselage would not change throughout the project as it proved to be a fast and easy production which did not require improvements. The wing construction however did change. Several reasons for this are:

- Several components needed to be fitted inside the wing which was hard with a shell structure
- The Rohacell structure protruded trough the wing skin
- The outgassing of the coating created trapped air between the coating and the Kevlar
- The coating was rather heavy ($\pm 70gr$)

The first two problems were solved by having a foam core in the wing and the last two problems were solved by removing the coating. The outer shells would be constructed the same way as before, however this time without the Rohacell core in between the fiber layers. Then a cnc-hotwire cut foam core would be inserted in each of the shells (see figure 5.12). The core would then be sanded flush with the production molds resulting in a wing that was exactly cut in a upper and lower half. Holes for the servo system, batteries and spar are then cut in the foam core enabling the components to be nicely fixed in the wing. This is followed by gluing the upper and lower half of the wing together with a paste of epoxy and glass bubbles.

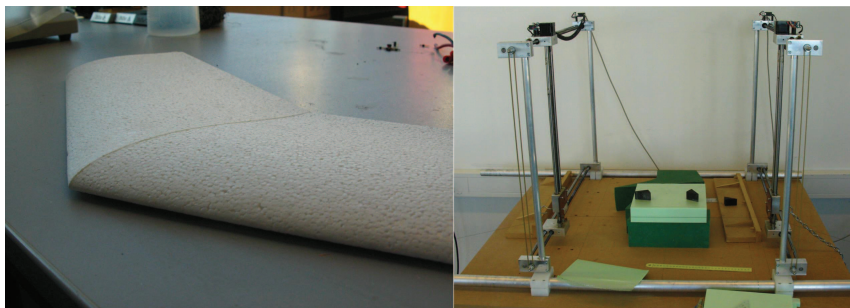


Figure 5.12: Foam core, of which two are needed during the construction of the wing, and the CNC-hotwire foam cutter.

The total weight of the wing, without the components inside, lowered from $205gr$ for the first wind tunnel model to $85gr$ for the competition model(see figure 5.13). This illustrates the gain in experience with building lightweight constructions. However future

research into this topic is required as building mini-UAV's requires very light and delicate fibers, and very thin structures. The building process explained here is a first step into this research. The author strongly suggests a close cooperation between the MAVLab, the structures department and the materials department, to obtain better construction methods and thus better mini-UAV's.

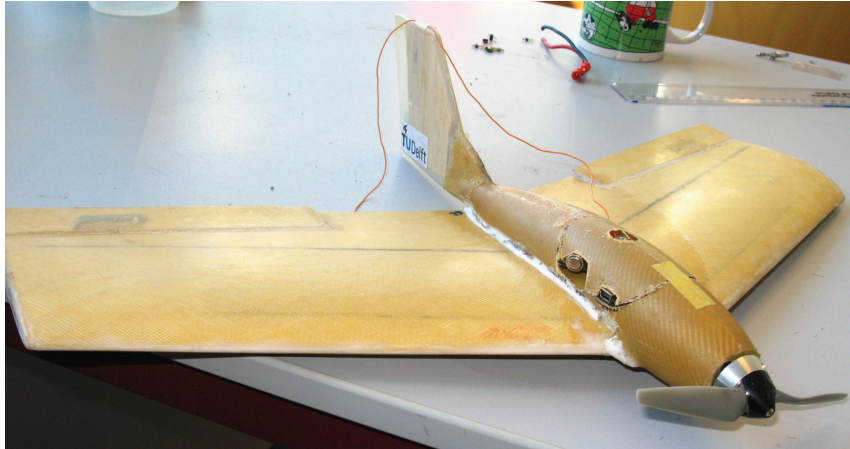


Figure 5.13: The finished competition aircraft.

5.1.4 Wind Tunnel Test Plan

During both wind tunnel campaigns the same tests plan was followed. This test plan involved aerodynamic force measurements and boundary layer visualizations. A detailed overview of the tests is presented next.

Force measurements

The force measurements were performed to analyze the aerodynamic efficiency and the stability of the aircraft.

The first set of tests:

- Configuration:
 - No turbulator strips
 - No propeller mounted
 - Elevons in the neutral position
- Angle of attack range: $0^\circ \rightarrow stall \rightarrow -5^\circ \rightarrow 0^\circ$
- Side slip angle range: 0°
- Velocity: $15m/s, 20m/s, 25m/s$

These tests have to provide insight in the effects caused by different Reynolds numbers. Expected differences are the maximum lift coefficient and changes in the drag curve.

The second set of tests:

- Configuration:
 - Turbulator strips added at different locations
 - No propeller mounted
 - Elevons in the neutral position
- Angle of attack range: $0^\circ \rightarrow stall \rightarrow -5^\circ \rightarrow 0^\circ$
- Side slip angle range: 0°
- Velocity: $20m/s$

Changing the locations and shapes of the turbulator strips will most likely change the drag curve. The situation that provides the best lift over drag ratio will be used for the following tests.

The third set of tests:

- Configuration:
 - Turbulator strips added at the best locations
 - Propeller mounted and motor on
 - Elevons in the neutral position
- Angle of attack range: $3^\circ \rightarrow 8^\circ$
- Side slip angle range: 0°
- Velocity: $15m/s, 20m/s, 25m/s$

During these tests the motor will be set at different power settings. This is to provide an insight in the power required to maintain straight horizontal flight, and to determine the efficiency of the propulsion system at different speeds.

The fourth set of tests:

- Configuration:
 - Turbulator strips added at the best locations
 - No propeller mounted
 - Symmetric elevon deflections
- Angle of attack range: $0^\circ \rightarrow stall \rightarrow -5^\circ \rightarrow 0^\circ$
- Side slip angle range: 0°

- Velocity: $20m/s$

During these test the elvons will be deflected symmetrically at different upward and downward angles. This is to determine the elevator efficiency, $C_{M_{\delta_e}}$.

The fifth set of tests:

- Configuration:
 - Turbulator strips added at the best locations
 - No propeller mounted
 - Asymmetric elevon deflection
- Angle of attack range: $0^\circ \rightarrow stall \rightarrow -5^\circ \rightarrow 0^\circ$
- Side slip angle range: 0°
- Velocity: $20m/s$

Asymmetric elevon deflections provide information about the aileron efficiency of the aircraft. It is interesting to investigate this as it is noticed that mini-UAV's are extremely responsive to aileron deflections.

The sixth set of tests:

- Configuration:
 - Turbulator strips added at the best locations
 - No propeller mounted
 - Elevons in the neutral position
- Angle of attack range: $3^\circ \rightarrow 8^\circ$
- Side slip angle range: $0^\circ \rightarrow 12^\circ \rightarrow 0^\circ$
- Velocity: $20m/s$ ($15m/s$, $25m/s$)

Setting the aircraft under different side slip angles provides information about the yaw-stability of the aircraft. It might be interesting to perform these tests at low speeds to investigate if the yaw-stability is maintained at low speeds.

Reserve set of tests:

- Configuration:
 - Turbulator strips added at the best locations
 - Propeller mounted and motor on
 - Symmetric and Asymmetric elevon deflections
- Angle of attack range: $3^\circ \rightarrow 8^\circ$
- Side slip angle range: 0°
- Velocity: $20m/s$

These test can be performed when there is still some testing time left. This provides information on the effect of the propeller on the elevon effectiveness.

Boundary Layer Visualizations

During the first wind tunnel campaign the boundary layer visualizations were limited to three cases. All of them are performed at the angle of attack corresponding to the maximum lift over drag ratio and at a velocity of $20m/s$. The following situations were visualized:

1. Propeller mounted and motor on, without turbulator strips
2. No propeller mounted and without turbulator strips
3. No propeller mounted and a turbulator strip close to the wing leading edge.

The first two boundary visualizations are to investigate the effect of the propeller flow on the boundary layer. The third one was to investigate if the turbulator strips were effective in tripping the boundary layer.

During the second wind tunnel campaign the visualizations were expanded to investigate more situations. The same tests as in the first campaign were performed to establish differences between the two wing shapes. The added visualizations were to establish trends in the boundary layer, like the effects of different angles of attack and changes due to elevon deflections. The added visualizations are:

First set of visualizations:

- Configuration:
 - No propeller mounted
 - No turbulator strips
 - Elevons neutral
- Angle of attack range: 0° , 5° , 10° , 20°
- Side slip angle range: 0°
- Velocity: $20m/s$
- Visualizations on upper and lower wing surface

Second set of visualizations

- Configuration:
 - No propeller mounted
 - No turbulator strips
 - Elevons 11° up
- Angle of attack range: 5°
- Side slip angle range: 0°
- Velocity: $20m/s$
- Visualizations on upper and lower wing surface

5.2 Wind Tunnel Results

In this section the results obtained during the wind tunnel testing will be presented. All the tests mentioned in the test plan were performed. However after a thorough investigation of the force measurements it had to be concluded that some mistakes had occurred during the measurements. It was discovered that these problems were related to the yaw-pitch system of the balance. It was decided to use the results from the force measurements to give a clear analysis of the problems that have presented them self such that they will not occur again. This however implies that the results can not be used for the intended validation of the quasi-3D tool and the optimizer.

The boundary layer visualization on the other hand are very nice and present some really clear illustrations of low Reynolds number effects on the boundary layer. Comparisons and trends observed with these visualizations can be found in section 5.2.2.

5.2.1 Force Measurements

The force measurements showed signs that they might be wrong. These signs will be explained in the first part of this section. After that an overview will be presented of possible causes that contributed to the errors. The last part will be to show how sensitive the results are to these mentioned causes.

Indications for Incorrect Results

Problems with the Lift at $\alpha = 0^\circ$

The first and clear sign that something was wrong could be seen in the lift at $\alpha = 0^\circ$. The definition of the angle of attack was chosen the same as for the CFD-calculation and the quasi-3D method. An angle of attack equal to zero of the aircraft corresponds to a zero angle of attack for the root airfoil. The prototype wing had a linear twist of -3° . This means that all airfoils in the wing are positioned at a negative angle of attack when the aircraft is at zero angle of attack.

In figure 5.14 the lift curve of the airfoil used in the prototype wing, obtained from Xfoil and wind tunnel results obtained from reference [25], are plotted. From this graph it can be seen that the zero lift angle of attack for the airfoil is located at $\alpha = -0.8^\circ$ ⁴. This means that, while keeping the twist in mind, about 75% of the wing span has a angle of attack lower than the airfoils zero lift angle of attack, and thus expecting the wing to produce a slightly negative lift. When looking at a comparison between CFD, the quasi-3D method and the wind tunnel results, in figure 5.15, a large difference can be noted at $\alpha = 0^\circ$. The results obtained with the quasi-3D method and CFD do not include the fuselage while the experimental results do. However the results seen in figure 5.15 show that, at an angle of attack of zero, for the CFD and quasi-3D results the lift is indeed

⁴The differences between the curves in figure 5.14 are due to an overestimation of the lift coefficient by Xfoil and an underestimation in the wind tunnel data. The wind tunnel data are obtained with balance measurements, instead of pressure measurements, taking into account separated flow at the wind tunnel-model edges.

slightly negative ($C_L = -0.024$), the wind tunnel results however suggest a rather large lift coefficient ($C_L = 0.067$) at that angle.

There is also a large difference in the lift curve slope. This difference however was not used as an argument to treat the results as incorrect. A possible cause for the difference was found and will be discussed later on in this chapter.

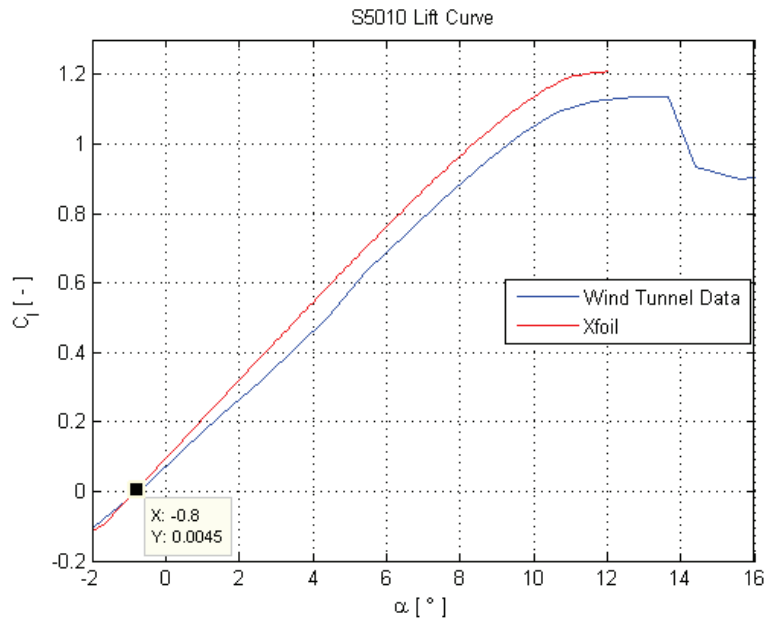


Figure 5.14: Lift coefficient against the angle of attack for the S5010 airfoil.

Changes in the Drag due to Elevon Deflections

This argument is purely based on a trend discovered in the data while deflecting the elevons up. Having a elevon up deflection it can be expected that the lift will shift down and the moment coefficient shift up, at the same angle of attack. This was the case, however the minimum drag was lower than the ones without elevon deflection. This is illustrated in figure 5.16.

On top of that the maximum lift over drag and increased to 18 for a 7.5° elevon deflection (see figure 5.17). The only logical explanation at the time was that the lift distribution improved to a more elliptical one, improving the induced drag. A good validation of the maximum lift over drag ratio was to check it against the maximum theoretical lift over drag ratio.

Assuming an elliptical lift distribution ($e = 1$) it is possible to determine the maximum theoretical lift over drag ratio using equation 3.57. In this equation A was set equal to the prototype aspect ratio and C_{D_0} was obtained from the wind tunnel data (elevon deflected

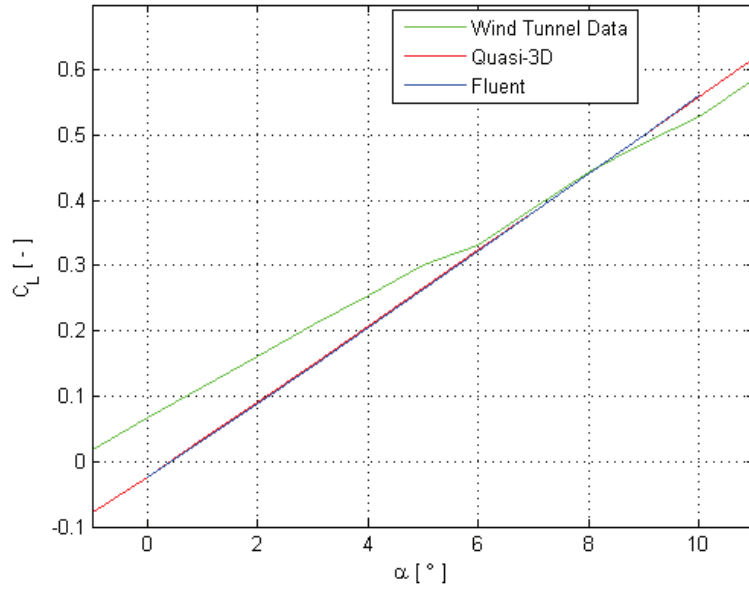


Figure 5.15: Lift coefficient against the angle of attack for the Prototype wing. Experimental data compared to CFD and the quasi-3D method.

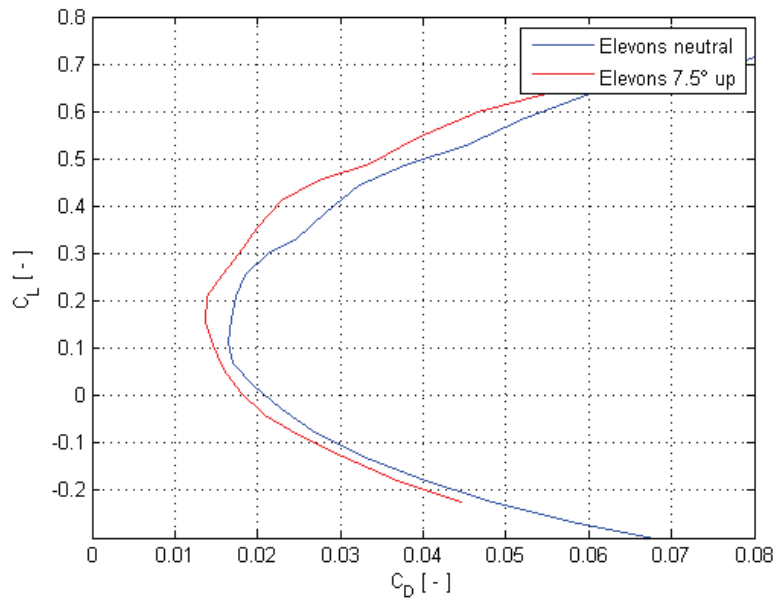


Figure 5.16: Drag polar for elevons in neutral position and for a deflection of 7.5° up.

up).

$$\left(\frac{C_L}{C_D}\right)_{max} = \frac{\sqrt{\pi}}{2} \sqrt{\frac{Ae}{C_{D_0}}} = \frac{\sqrt{\pi}}{2} \sqrt{\frac{3.07}{0.01378}} = 13.23 \quad (5.17)$$

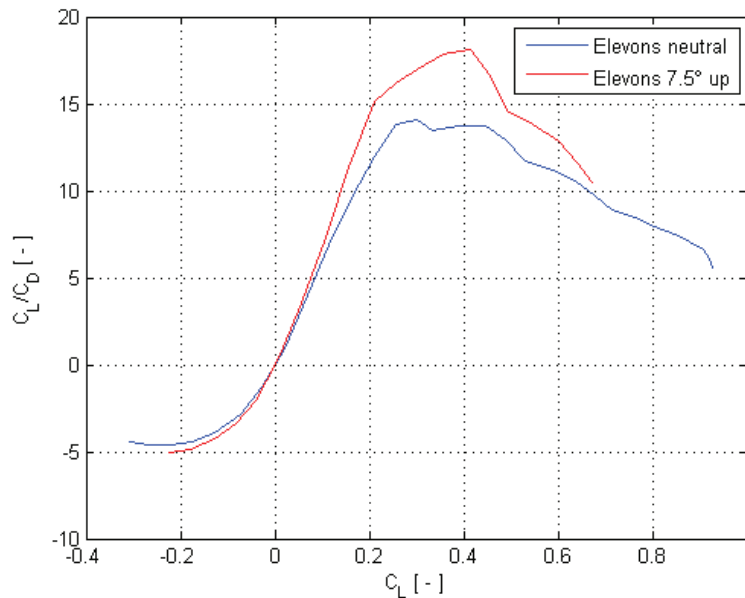


Figure 5.17: Drag polar for elevons in neutral position and for a deflection of 7.5° up.

It was thus discovered that the theoretical maximum lift over drag ratio was exceeded by 38%. This is impossible and required further attention.

Visual Inspection During Wind Tunnel Testing

During the second wind tunnel campaign it was decided to look for visual clues that something might be wrong. During one of the tests the model was set at an angle of attack of 5° , with the tunnel turned off. A viewfinder was then pointed at a corner of the propeller mount, this then served as a visual reference. The tunnel was turned on and no changes were noted in the angle of attack. The next step was to set the elevons in the full up position, which then resulted in a clear change in the angle of attack. No exact measurements could be taken through the viewfinder but the change in angle of attack was estimated to be around 1° to 1.6° . Setting the elevons back to the neutral position, a return towards the original position could be observed, however about half the error in angle of attack remained. This remaining error is most likely to be caused by friction in the linkages.

Possible Causes for the Errors

The sensor used has a high accuracy and was assumed not to be the cause of the measurement problems. The yaw-pitch system on the other hand already proved to possess some imperfections. It was concluded that something might be wrong in setting the angles. Another aspect is the fact that the balance is a rather large object in the tunnel compared to the aircraft. Flows over the balance cover might also have contributed to the problem.

Errors in the Pitch Angle

The first step is to create an overview of all the components involved in setting the pitch angle. These are then put in a table, table 5.1, together with a rating of the influence they might have on producing an error in the pitch angle.

Table 5.1: Overview of components involved in setting the pitch angle and their likelihood of causing errors.

Software controlling the servo	unlikely
Electronics controlling the servo	unlikely
Servo accuracy	very likely
Servo holding force	very likely
Servo mount	unlikely
Linkage between the servo and the balance head	very likely
Play in the pitch axis	unlikely
Sensor stiffness	very likely
Error in determining the pitch offset between the sensor and the model	likely
Structural flexibility of the model close to the connection to the sensor	unlikely

The software used to control the servo has a higher resolution than the servo digital input, that's why it is unlikely to have a negative effect. The same is true for the electronics used to control the servo, as it was developed for autopilot purposes which require high accuracy.

The servo accuracy is degraded by the fact that the potentiometer is positioned on the second to last gear and thus does not take into account the play between the last two gears. The holding force of the servo might also cause problems at the higher angles of attack as the aerodynamic moment might be higher than the maximum servo force. The servo mount is unlikely to have any effect as it is a quite sturdy mount together with a rather small moment-arm acting on it. A picture of the servo mount can be seen in figure 5.18.

The linkage between the servo and the balance head is shown in figure 5.3. Two issues are involved with this system, namely play in the linkages between different components and strain due to the forces put on the system. The linkage has some weak spots which are likely to flex under high stresses. Play in the axis on which the balance head rotates, to set the pitch angle, has been removed before the first measurements and is unlikely to cause problems any more. The rotational stiffness of the sensor is known and is presented in the sensor data sheet which can be seen in appendix C.

The pitch offset between the sensor and the model can be seen in figure 5.6. If this angle is not entirely correct, the rotation of the forces and moments from the measurement reference frame to the aerodynamic reference frame will be wrong. This can be seen in equation 5.1 and 5.2. This error is likely to be present because only a small error in this angle has a rather large effect on the drag coefficient. In case of a wind tunnel model with structural flexibility around the connection to the sensor, results in this angle to change with the angles of attack. This however was assumed not to be the case for the models under consideration in this report.

So summarizing these issues in angles gives:

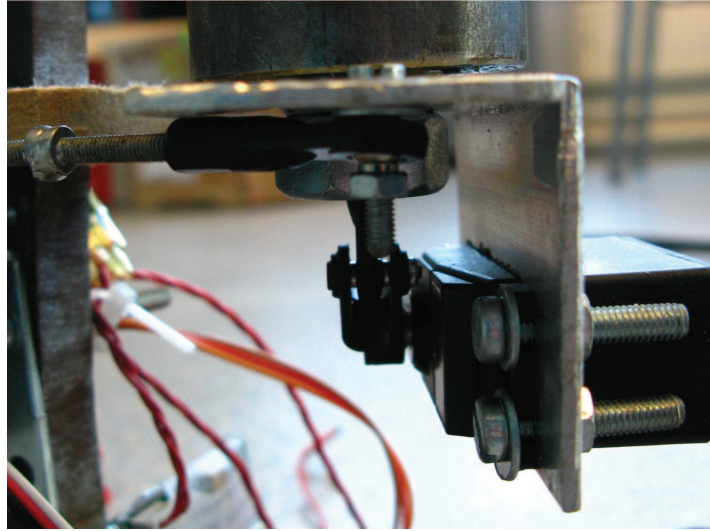


Figure 5.18: Servo mount for the pitch servo.

- $\Delta\alpha_{strain} = \Delta\alpha_{servo} + \Delta\alpha_{linkage} + \Delta\alpha_{sensor}$
- $\Delta\alpha_{play}$
- $\Delta\alpha_{maxHF}$
- $\Delta\alpha_{offset}$

The $\Delta\alpha_{strain}$ is a collection of the changes in pitch angle due to the forces and moments acting on the different components. The $\Delta\alpha_{sensor}$ is easy to model using:

$$\Delta\alpha_{sensor} = \frac{-T_{y_{aero}}}{K_{t_y}}; \quad (5.18)$$

In which K_{t_y} is obtained from the sensor data sheet in appendix C and $T_{y_{aero}}$ is the measured moment around the y-axis with the zero-run measurement subtracted. The other components in the $\Delta\alpha_{strain}$ are harder to determine. It is possible to determine a similar value as the K_{t_y} in equation 5.18 but than for the complete mechanical system from servo gears to balance head. However a better solution to the problem would be to measure the angle at the head of the balance or even better, creating a feedback loop between the sensor head and the servo input.

The $\Delta\alpha_{play}$ and $\Delta\alpha_{maxHF}$ are discontinues errors. The play in the mechanical connections is pushed into the same direction as the force acting on it. A constant change in the pitch angle can be noticed once the force switches from one direction to the other. The $\Delta\alpha_{maxHF}$ is the change in the pitch angle once the force acting on the servo exceeds the maximum holding force. The servo will keep the pitch angle fixed at the angle were the maximum holding force balances the aerodynamic forces and moments. An angle measurement at the head of the balance or a feedback loop will also bring solution to these discrepancies.

The pitch offset has to be measured before the wind tunnel tests and should be very accurate as a small difference in this angle results in rather large errors in the coefficients as will be shown in section 5.2.1.

Flow Interference between the Model and the Balance

It is likely that, apart from solid blockage, there is a kind of interaction between the balance and the model. Two kinds of disturbances can be distinguished:

- Near field disturbances, caused by the sensor-model connection.
- Far field disturbances, caused by flows over the balance cover.

A detailed investigation, probably involving wind tunnel testing, will be required to state something useful concerning this subject.

Sensitivity of the Results

Establishing how the aerodynamic coefficients are influenced by having discrepancies in the angle of attack will be shown in this section.

As was seen in equations 5.1 and 5.2, the angle of attack, which is the same as the pitch angle, is required to calculate the coefficients. Assuming that whatever error in the pitch angle, happens before the force and moment measurements are taken, means that the discrepancy in the angle of attack must be taken into account for calculating the aerodynamic coefficients. It does not suffice to only correct the angle of attack after determining the coefficients. However, the correction to the angle of attack still has to be applied and is taken into account in the graphs presented in this section.

Effect of Strain

Lets try to define a correction for the angle change due to strain. Figure 5.19 shows all the forces involved in producing deformations in the model, sensor and yaw-pitch system.

The force and moment due to the weight of the model were taken into account during the calibration of the angles and can thus be emitted from the problem. With the remaining forces, moments and dimensions equation 5.19 can be formulated. The $T_{y_{aero}}$ and the $F_{z_{aero}}$ are shown, in figure 5.19, in positive direction.

$$\Delta\alpha_{strain} = \frac{1}{K_{tot}}(T_{y_{aero}} + F_{z_{aero}} \cdot x_1) \quad (5.19)$$

In this equation $T_{y_{aero}}$ and $F_{z_{aero}}$ are the measured aerodynamic moment around the y-axis and the measured aerodynamic force in the z-direction, respectively. The torsional stiffness of the complete system, K_{tot} , can be estimated with the values previously defined in section 5.2.1. Assuming a $\Delta\alpha = 1.3^\circ$ was observed and the change in aerodynamic force and moment due to the elevon deflection are established at $\Delta F_{z_{aero}} = -0.7299$ and

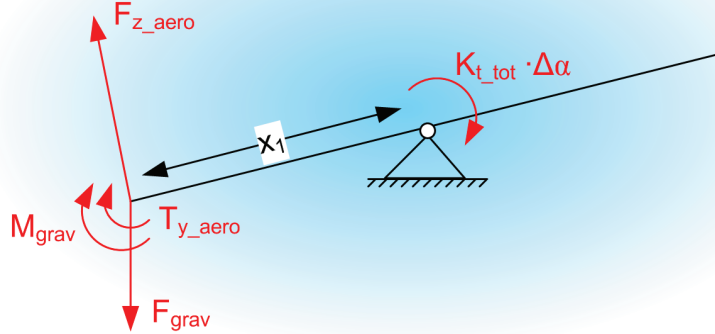


Figure 5.19: Forces acting on the balance head causing strain in the system.

$\Delta T_{y_{aero}} = -0.1256$. The value of x_1 was measured to be $1.35 \cdot 10^{-2}m$. Then $K_{t_{tot}}$ is defined as,

$$K_{t_{tot}} = \frac{(\Delta T_{y_{aero}} + \Delta F_{z_{aero}} \cdot x_1)}{\Delta \alpha_{measured}} = -0.104 \left[\frac{Nm}{deg} \right] \quad (5.20)$$

This creates a large change in the aerodynamic coefficients as can be observed in figures 5.20 to 5.22. The observations from these figures can be summarized in:

- An increase in the lift curve slope
- The drag variation with the lift has changed drastically
- The maximum lift over drag ratio has changed drastically due to the previous mentioned changes.

Conclusion: The effect of strain in the system is unforgiving when it is not modeled correctly.

Effect of the Discontinues Angle Changes

Two discontinues angle changes were defined in section 5.2.1 namely the angle due to mechanical play and the angle due to exceeding the maximum holding force of the servo.

It is hard to predict the change in the pitch angle when the system has a combination of mechanical play and friction. The effect without friction will be that a change in the angle of attack will only occur when the force pulling on the mechanical linkages, is opposite to the force exerted on the system during calibration. An indication of mechanical play combined with friction was seen in the measurements when they were performed for angles of attack ranging up to stall and then returning over the same angles. This is visualized in figure 5.23. The difference in the drag, at the low lift coefficients, is most probably

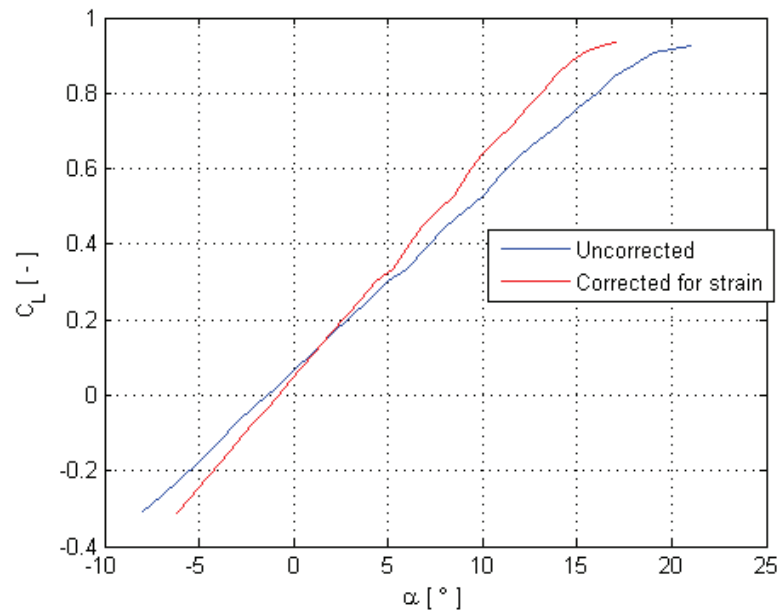


Figure 5.20: Changes in the lift coefficient due to a strain correction on the results.

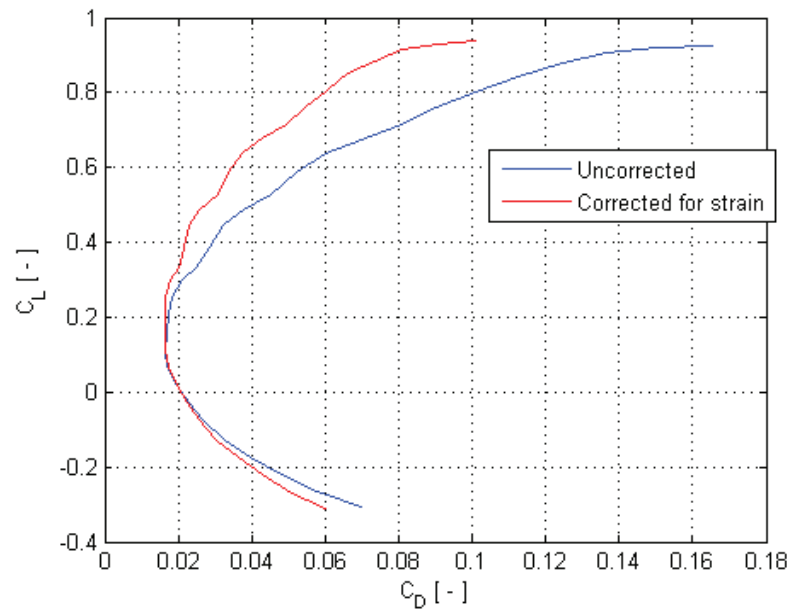


Figure 5.21: Changes in the drag polar due to a strain correction on the results.

due to a remaining difference in the angle of attack, as was also observed in section 5.2.1. It is unlikely to be aerodynamic hysteresis as this only occurs after stall and disappears completely when the angle of attack is decreased below a certain threshold.

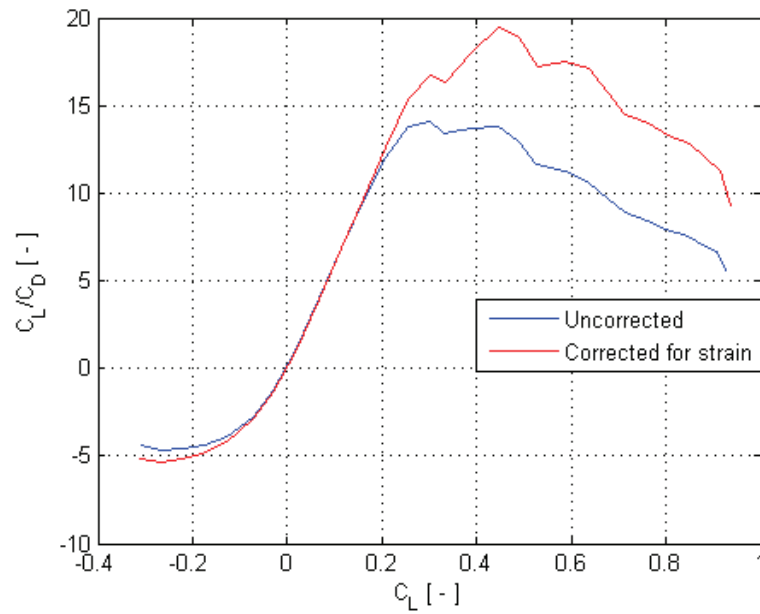


Figure 5.22: Changes in the lift over drag ratio due to a strain correction on the results.

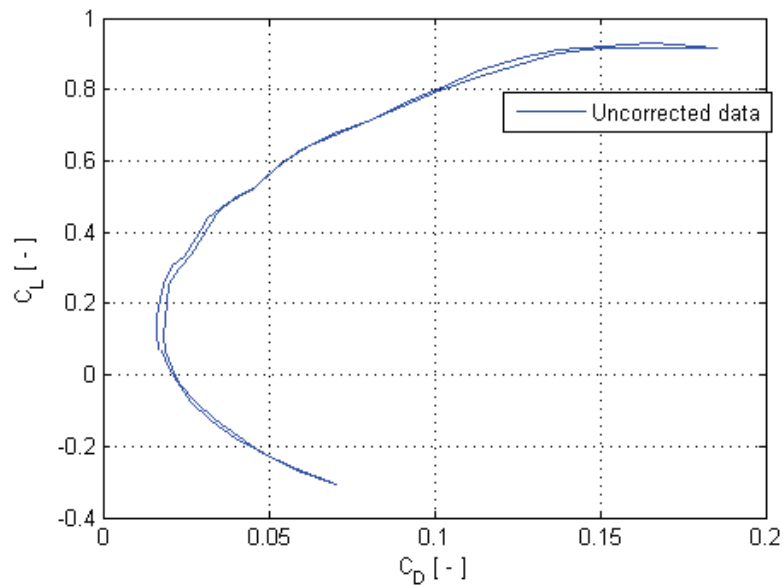


Figure 5.23: Drag polar for angles of attack going from $0^\circ \rightarrow 22^\circ \rightarrow -8^\circ \rightarrow 0^\circ$.

During some of the measurements it was noted that the servo was unable to set the angle of attack above a certain value. When this is not taken care of, it might lead to thinking that the stall angle of attack is reached, as the input to the servo increases, thus believing to be at higher angle of attack, while the lift coefficient remains constant.

Effect of an Error in the Pitch-offset

This effect is best illustrated by simply showing the difference by simply changing $\alpha_{pitch-offset}$ from 1.42° to 1.92° . The change in the pitch-offset is small but the effect it has on the maximum lift over drag ratio is rather large (14%). This is illustrated in figure 5.24. The difference is only caused by a change in the drag coefficient, which can be seen in figure 5.25.

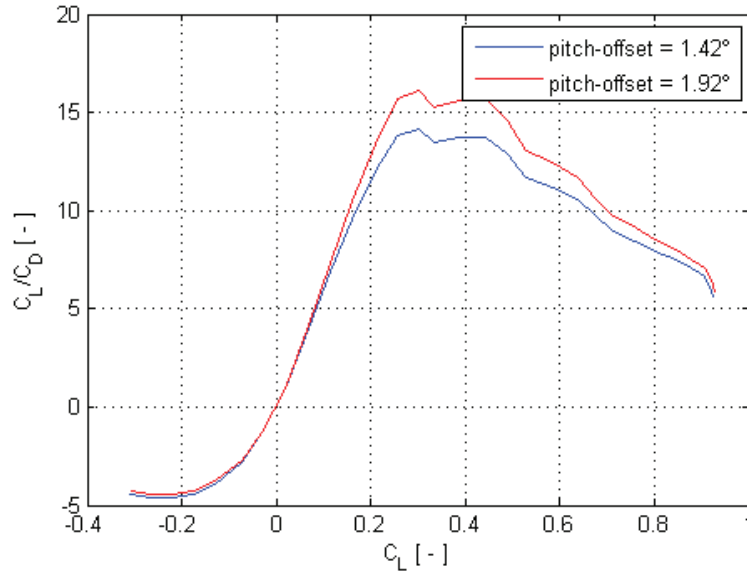


Figure 5.24: Effect of the pitch-offset angle on the lift over drag ratio.

5.2.2 Boundary Layer Visualizations

During each of the two wind tunnel campaigns a different model, Prototype A and B, was tested. The fuselage was kept the same for both models while the wing geometry changed. A detailed geometric description of both wings is presented in table 5.2. A 3-view of each model can be found in appendix D.

Table 5.2: Wing geometries of the two prototypes.

Prototype	b	c_{root}	λ	$\Lambda_{0.25}$	root afl.	tip afl.	ϵ	S	A	c_{mac}
	[m]	[m]	[-]	[deg]	[-]	[-]	[deg]	[m ²]	[-]	[m]
A	0.47	0.17	0.8	23.3	S5010	S5010	-3	0.0719	3.1	0.154
B	0.47	0.17	0.7	33.3	S5010	S5010	-3.5	0.0678	3.3	0.146

In this section several boundary layer visualizations will be compared to each other. This is to provide an insight into the flow phenomena on finite wings submitted to low Reynolds numbers. They will help to establish the best inputs for the optimization tool.

The visualizations presented in this section are rather unique. No visualizations could be

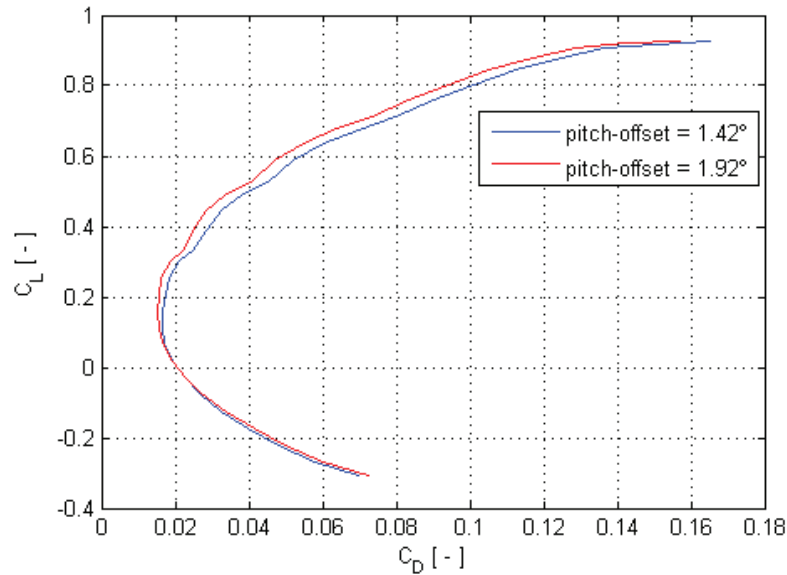


Figure 5.25: Effect of the pitch-offset angle on the drag coefficient.

found in literature that showed a boundary layer on a low aspect ratio wing at these low Reynolds numbers ($\sim 2 \cdot 10^5$).

The angles of attack mentioned in this section are all angles at which the aircraft was set without any of the previous mentioned corrections. Whenever referring to left and right in this section, it is assumed to be from the readers point of view.

Comparison between Prototype A and B

A picture of the boundary layer for each prototype can be seen in figure 5.26. These pictures are taken when both aircraft were under an angle of attack of 5 degrees without any turbulator strips, and without the propeller.

In these pictures a top-down view is seen from the upper surface of the wing. The leading edge is pointed to the upside of the page.

To start this explanation some typical features of a low Reynolds number boundary layer will be addressed. At the leading edge of the wing, the boundary layer starts as a laminar layer which is represented by the darker area above the bright yellow area. As explained earlier, the laminar boundary layer separates from the wing surface after which it destabilizes and finally transitions into a turbulent boundary layer. This turbulent boundary layer reattaches to the wing leaving behind a so called laminar separation bubble. This bubble is clearly visual as the bright yellow region on the wing. After this region the boundary layer is turbulent up until the trailing edge. These are typical features which can also be seen in an Xfoil-calculated pressure distribution over the airfoil (See figure 5.27).

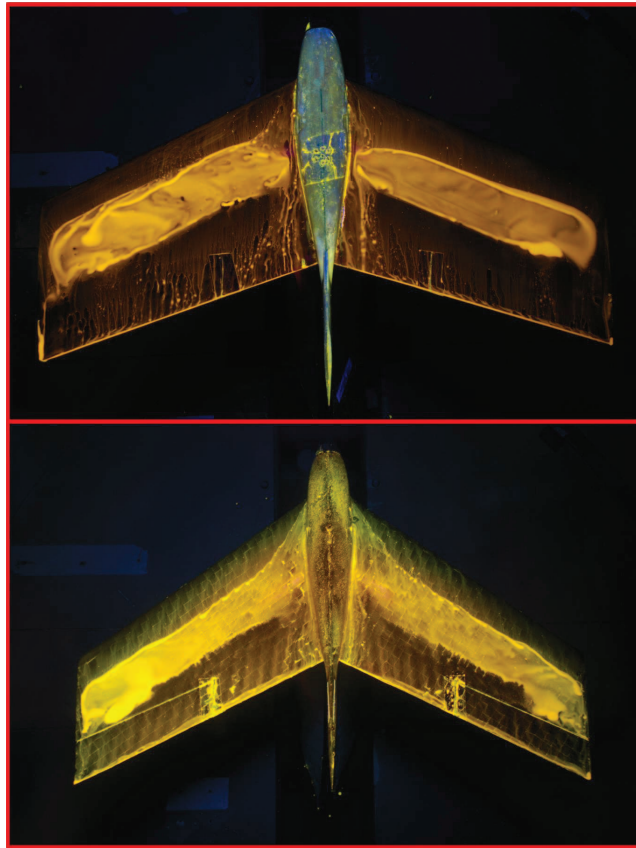


Figure 5.26: Boundary layer visualization for prototype A (upper) and prototype B (lower) at $\alpha = 5^\circ$.

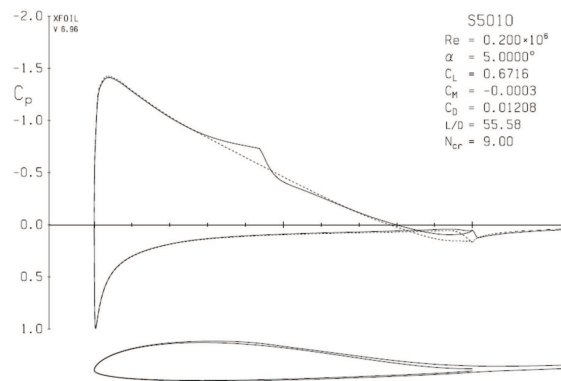


Figure 5.27: Boundary layer features on the S5010 airfoil at $\alpha = 5^\circ$ and $Re = 2 \cdot 10^5$.

Looking back at figure 5.26 some interesting features and difference between the models can be noted.

Starting at the root of the wing a clear difference can be seen between the laminar

separation bubbles of models A and B. In model A (the upper picture) the laminar separation bubble appears to have a local decrease in its chord wise length and even disappears close to the fuselage. The decrease in size is probably due to a local change in the pressure distribution due to the presence of the fuselage. The disappearance of the bubble has probably its origin in the fact that the boundary layer over the fuselage is turbulent and interacts with the boundary layer of the wing.

Model B shows some different features close to the root. Here it appears as if the bubble starts at the interface between the wing leading edge and the fuselage and reattaches at about 50% of the wing chord. A strong backward movement of the laminar separation is noticed up until 20% of the span after which it remains more or less parallel with the leading edge.

Another noticeable difference can be seen at the tip of the wing. For model A it is not very clear for the right wing tip, however the left wingtip shows sufficient detail. It can be seen that the bubble only extends to about 95% of the wing span for model A and up to about 98% for model B. This has probably to do with the shape of the tip and how the tip vortex curls around it. The tip vortex introduces a lot of disturbances in the boundary layer making it turbulent and thus removing the laminar boundary layer. A change to the tip shape had been introduced after reading in reference [15] about the influence the tip shape has on the effective aspect ratio.

Model A has a rounded tip while model B has a straight wing tip. An illustration of these wing tips and their effects on the tip vortex can be seen in figure 5.28. The rounded tip keeps the vortex closer to the wing while the straight tip sheds it further reducing its effect on the wing.

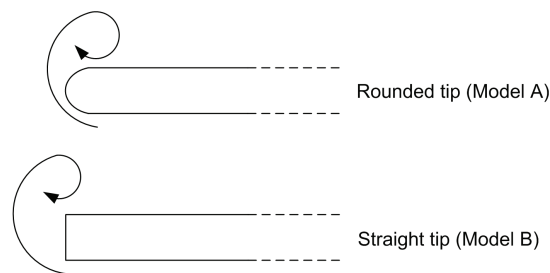


Figure 5.28: Illustration of a rounded tip and a straight tip with their tip vortex.

A difference can also be noted between the left and the right wing of model A. This was actually the first aircraft produced and due to the lack of experience in building, it suffered from a slight indentation over quite a large portion of the left wing. This distorted the airfoil shape and is believed to have caused the difference between both sides.

The laminar separation bubble on model B also seems to increase in size, on both sides, at about 75% of the wing span. However no clear explanation can be given for this phenomenon which is not present in model A. It might have something to do with the increased sweep of this model.

Tripping the Boundary Layer

Adding a sufficiently thick turbulator, that does not protrude through the boundary layer, at the correct location, will force the boundary layer to trip before laminar separation can occur. In figure 5.29 a turbulator strip is added to the wing of model A at 5% of the chord length. The wing is still at a 5 degree angle of attack, and it is clearly visible that the laminar separation bubble has disappeared. This shows that the laminar flow has transitioned before separating from the surface. This however does not directly imply that the drag is lower. The pressure drag originally present over the separation bubble has been removed, but in stead the friction drag due to the turbulent boundary layer has increased.

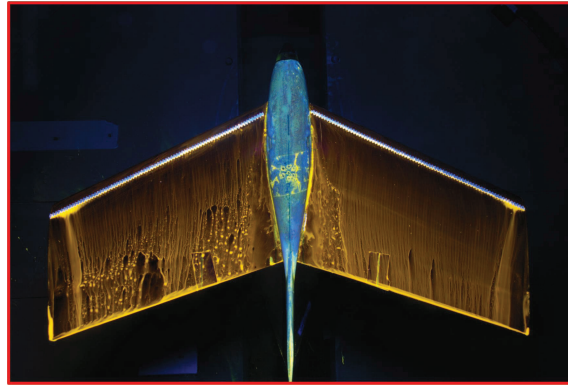


Figure 5.29: Boundary layer visualization for prototype A at $\alpha = 5^\circ$ and a turbulator strip at 5% of the chord length.

In figure 5.30 a different type of turbulator was used at 30% of the chord length of model A. The wing, still at an angle of 5 degrees, shows that the bubble has not been eliminated but encapsulated the turbulator reducing its effectiveness. It can be seen that in the inboard 50% of the span there appears to be some turbulent flow right after the turbulator, but it is not enough to trip the boundary layer further downstream.

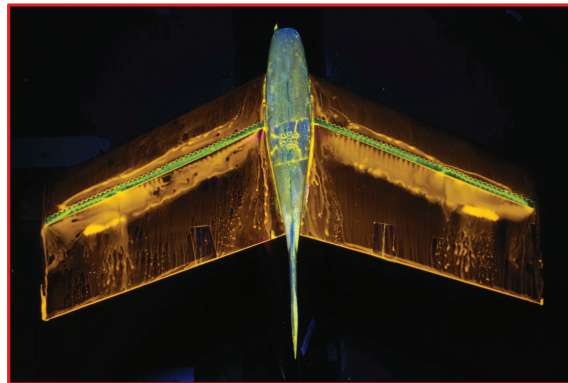


Figure 5.30: Boundary layer visualization for prototype A at $\alpha = 5^\circ$, with a turbulator strip encapsulated by the bubble.

Boundary Layer at Different Angles of Attack

For prototype B, boundary layer visualizations were performed at different angles of attack. For the upper surface, the expected trend would be that the laminar separation bubble moves towards the leading edge and its chord-wise length decreases. The forward motion is because of the increasing adverse pressure gradient, right after the leading edge, with increasing angle of attack. The laminar boundary layer is not good in handling strong adverse gradients and will thus separate earlier. The transition point moves forward too but at a slightly higher rate than the separation bubble, causing this bubble to be shorter. The lower surface on the other hand is expected to be fully laminar, or at least up to the elevon hinge.

Looking at figure 5.31 it can be seen that for the upper surface the bubble does seem to follow the previous conclusions for angles of attack ranging from 0 to 10 degrees. At $\alpha = 20^\circ$ a very different image is presented. A bubble seems to be located right at the leading edge (small yellow line on the leading edge). This bubble is followed by turbulent flow (visual as the darker area) which seems to separate not long after transition. The separated flow has most probably started at the trailing edge, at lower angle of attack, and moved towards the leading edge with increasing angle of attack. This is known as trailing edge stall, which mostly results in a docile stall behavior.

A slight difference can also be noted between the left and the right wing, at $\alpha = 20^\circ$, close to the fuselage. On the right wing it appears as if the bubble on the leading edge has burst, producing a full separated flow region over the inner 25% of the wing span. Probably a slight imperfection in the leading edge and a unstable separated flow emanating from the wing-fuselage interface are the underlying cause of the difference.

The lower surface shows some slight discrepancies from what was expected. At $\alpha = 0^\circ$ a rather large separated flow region can be observed on both wing-sides, however on the right wing this separated region is larger than on the left wing. The laminar flow on the lower surface, at this angle of attack, is probably close to the maximum pressure gradient it can handle, a small imperfection in the surface will cause it to separate. In this picture it can also be seen that the separated flow moves forward, towards the leading edge, when getting closer to the tip of the wing. This has to do with the negative twist in the wing, causing a gradual increase in the adverse pressure gradient, moving from the root to the tip.

The separated flow region decreases with increasing angle of attack, at $\alpha = 20^\circ$ a full attached laminar flow can be observed. The inner angles of attack, 5° and 10° , show the start of a laminar separation bubble, but transition does not occur before the trailing edge leaving behind a small separated flow region.

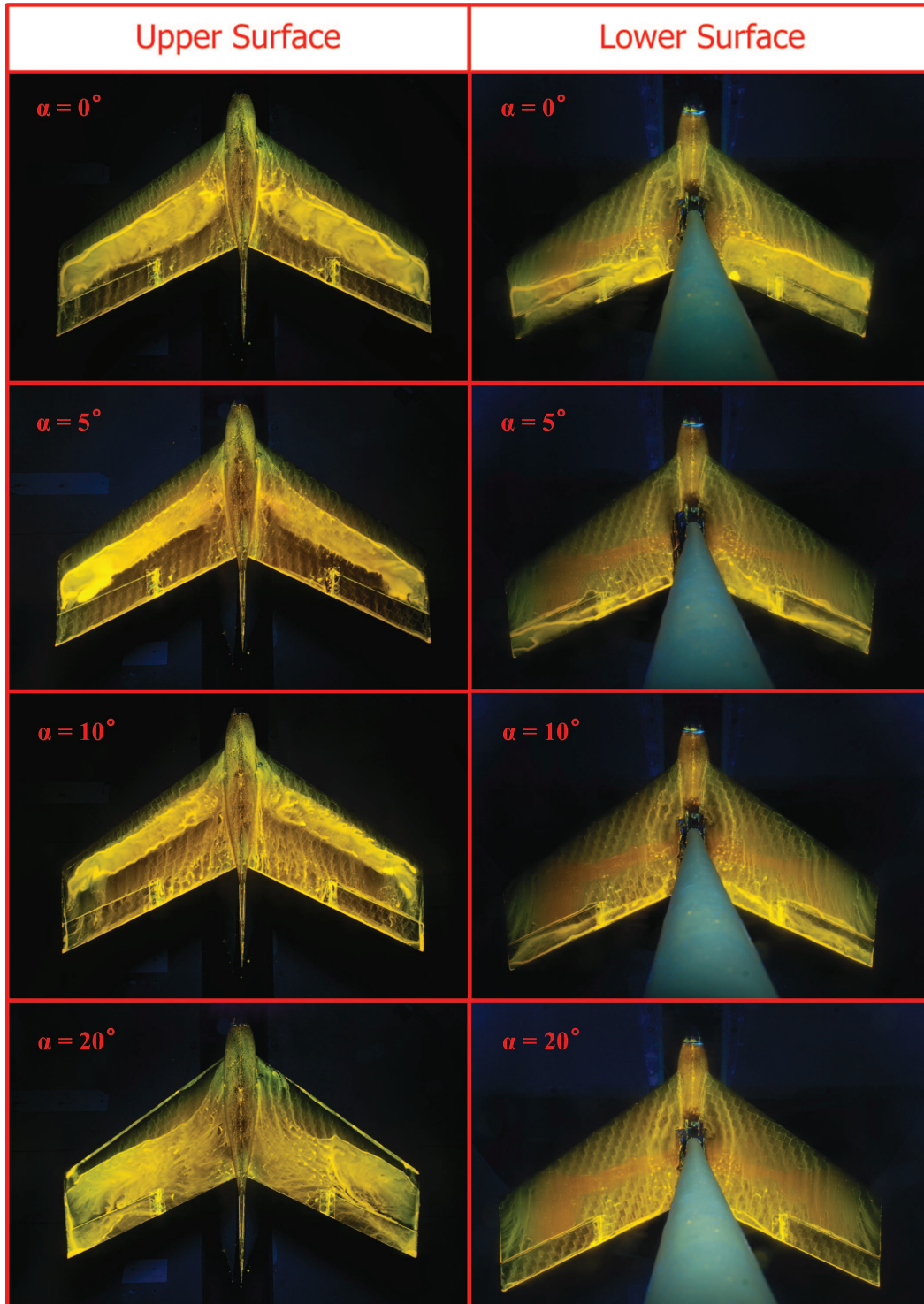


Figure 5.31: Boundary layer visualization of upper and lower wing surface for prototype B at different angles of attack.

Effect of the Propeller on the Boundary Layer

The effect of the propeller on the boundary layer is not exactly clear (see figure 5.32). The large laminar separation bubble has disappeared in the span region covered by the propeller. Focusing on this region it can be seen that close to the leading edge there is still some laminar flow present, this is followed by a highly swept bright line, connecting the interface between the wing leading edge and the fuselage to the front side of the laminar separation bubble. This line might be a vortex emanating from the wing-fuselage interface, or it is a small laminar separation bubble. This bubble is then reduced in size due to the higher Reynolds number produced by the velocity increase induced by the propeller. Both the vortex and the separation bubble would explain why the large separation bubble disappears in this portion of the wing.

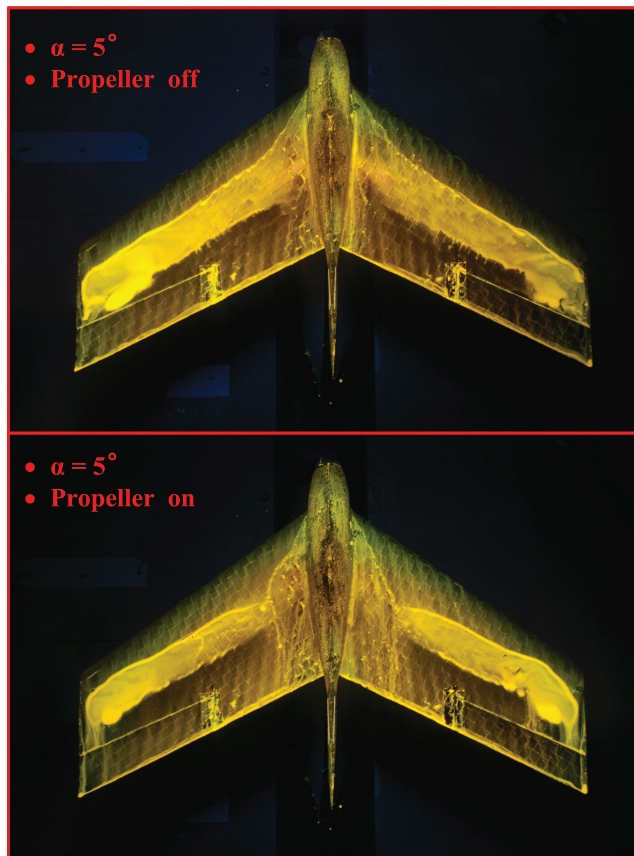


Figure 5.32: Boundary layer comparison between a propeller off and a propeller/motor on case for prototype B ($\alpha = 5^\circ$).

Effect of Elevon Deflection on the Boundary Layer

The elevons in figure 5.33 are deflected upward by 11° . This means that on the upper surface there will be a strong concave region, introducing a high pressure in this region. This in turn causes a stronger adverse pressure gradient which causes the laminar boundary

layer to separate earlier pushing the separation bubble closer to the leading edge. This is clearly visual on the left side of figure 5.33, especially the part close to the tip, which had an increased bubble size, is pushed forward.

For the lower surface the opposite is true. A sharp convex corner is created by the upward deflection of the elevon, producing a sudden decrease in the pressure which is then followed by a strong adverse pressure gradient tripping the boundary layer. Looking at the right side of figure 5.33 it can be seen that the laminar separation, that originally extended into the wake, is now followed by transition creating a closed bubble over the elevon. Close to the edge of the elevon, parallel with the flow, no bubble is visual which probably has to do with vortices emanating from these edges.

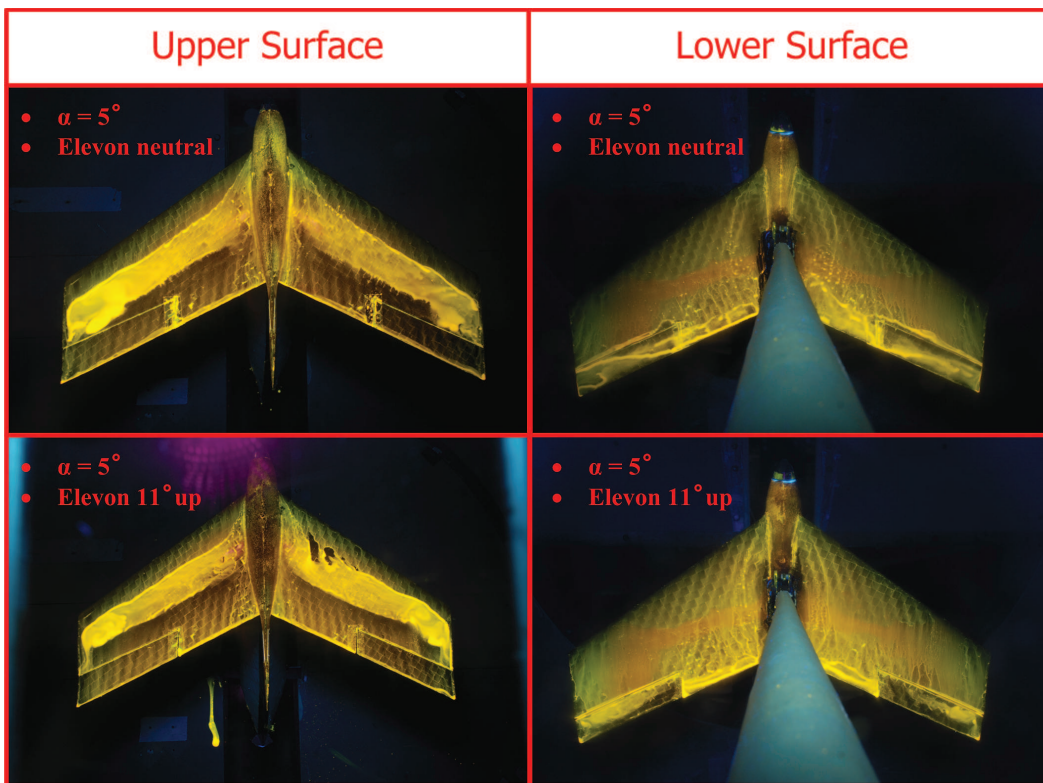


Figure 5.33: Boundary layer comparison for the prototype B wing with the elevons neutral and 11° ($\alpha = 5^\circ$).

5.3 Conclusions Concerning the Wind Tunnel Experiments

The intended validation of the quasi-3D method with wind tunnel force measurements could not be performed. This was due to the high level of uncertainty present in the data. The uncertainty was introduced by several factors like, the lack of accuracy in the angle of attack, due to several problems with the yaw-pitch system of the balance, and the undetermined effects the balance has on the flow field around the aircraft.

The boundary layer visualizations on the other hand provided insight in the low Reynolds number effects on the wing. This helps in getting the right settings for the optimizer such that the best approximation of the lift over drag ratio can be established. It also provided proof of the fact that laminar flow is present and how it is influenced by several factors like the propeller flow and elevon deflections.

Chapter 6

Results

In this chapter the results obtained with the wing-optimizer will be discussed and the final design for the competition aircraft will be presented. Three different optimizations were performed to establish the best possible design for the EMAV2009 long range competition aircraft. Two of these optimizations were used to establish the best possible wing assuming the same fuselage as used for the prototypes. For the third optimization this constraint was removed to see how much could be gained with a different fuselage. Results of these optimizations can be seen in section 6.1.

A detailed description of the final design for the competition aircraft can be found in section 6.2. The geometry and subsystems will be discussed followed by a performance analysis of its range capabilities.

6.1 Optimization Results

Three different optimizations were performed of which the results will be presented here. The first optimization used the prototype aircraft as an initial point for the variables. The boundaries and constraints on the variables were set such that the final result would provide sufficient space for the batteries in the wing and that the same fuselage as the prototype could be used.

The second optimization was set up exactly the same way as the first optimization, with the sole difference that it used a bad wing, in an aerodynamic sense, as a initial starting point. This was to provide insight in the capability of the optimizer of finding the same final result.

The third optimization was provided a lot more freedom, by increasing the range between the upper and lower bounds on the variables. It started with a reasonably good initial wing and would have to find its way to the best possible wing in the domain enclosed by the constraints. This was to show the maximum attainable aerodynamic efficiency and how it related to the result obtained by the previous two optimizations. It thus provided

insight on what to do with the fuselage. Changing to a new fuselage would require new molds and a lot of work, compared to having the prototype fuselage and accepting a small loss in the aerodynamic efficiency.

6.1.1 Optimization with Tight Constraints and the Prototype as an Initial Point

Mathematical Description of the Problem

The mathematical description for this optimization is the following:

Objective function:

$$\min_{\mathbf{x}} f(\mathbf{x}, \mathbf{c}) = -\frac{C_L(\mathbf{x}, \mathbf{c})}{C_D(\mathbf{x}, \mathbf{c})}$$

In which \mathbf{x} represents the vector with geometric variables for the optimization, containing:

- $\mathbf{x}(1) = b/2$
- $\mathbf{x}(2) = c_{root}$
- $\mathbf{x}(3) = \Lambda$
- $\mathbf{x}(4) = \lambda$
- $\mathbf{x}(5) = V_\infty$

The vector \mathbf{c} contains all constant values to define the fuselage, tail, aircraft weight and certain flow aspects on the wing. The values of the constants for this , and the following optimizations are:

- Aircraft weight = $0.5kg$
- Aircraft stability margin = 2.5%
- Forced transition on lower surface (for root and tip section) = $[0.8 \ 0.8]\%c$
- Forced transition on upper surface (for root and tip section) = $[1 \ 1]\%c$
- Fuselage cross-sectional shape = *circular*
- Fuselage length = $0.25m$
- Fuselage maximum diameter = $0.043m$
- Fuselage transition point = $0\%l^*$
- Propulsive efficiency = 0.7
- Number of tails = 1

- Tail root chord = $0.1m$
- Tail tip chord = $0.06m$
- Tail span = $0.08m$
- Tail airfoil = *naca0012*

Linear constraints:

$$\begin{aligned} 0.05 &\leq \mathbf{x}(1) \quad , \quad \mathbf{x}(1) \leq 0.235 \\ 0.169 &\leq \mathbf{x}(2) \quad , \quad \mathbf{x}(2) \leq 0.17 \\ 0 &\leq \mathbf{x}(3) \quad , \quad \mathbf{x}(3) \leq 40 \\ 0.5 &\leq \mathbf{x}(4) \quad , \quad \mathbf{x}(4) \leq 1 \\ 10 &\leq \mathbf{x}(5) \quad , \quad \mathbf{x}(5) \leq 35 \end{aligned}$$

Non-linear constraints:

Constraint on the Reynolds number:

$$\frac{\mathbf{x}(2) \cdot \mathbf{x}(4) \cdot \mathbf{x}(5)}{1.4607 \cdot 10^{-5}} \geq 6.5 \cdot 10^4$$

Constraint on the stall speed:

$$\sqrt{\frac{2W}{(\mathbf{x}(2) + \mathbf{x}(2) \cdot \mathbf{x}(4)) \cdot \mathbf{x}(1) \cdot 1.225 \cdot C_{Lmax}}} \leq 12$$

In this equation W represents the aircraft weight and the maximum lift coefficient is set equal to 0.95.

Constraint on the twist angle:

$$|\epsilon(\mathbf{x}, \mathbf{c})| \leq 10$$

The twist is a intricate function dependent on variables and constants as explained in section 4.1.2.

Constraint on the design lift coefficient:

$$\frac{2W}{(\mathbf{x}(2) + \mathbf{x}(2) \cdot \mathbf{x}(4)) \cdot \mathbf{x}(1) \cdot 1.225 \cdot (\mathbf{x}(5))^2} \leq 1.4$$

Initial point:

$$\begin{aligned} \mathbf{x}_0(1) &= 0.235 \\ \mathbf{x}_0(2) &= 0.17 \\ \mathbf{x}_0(3) &= 23.274 \\ \mathbf{x}_0(4) &= 0.8 \\ \mathbf{x}_0(5) &= 20 \end{aligned}$$

Optimized Geometry

After 29 hours, 13 iteration and 139 objective function evaluations, the optimization was terminated. The reason for the termination was the magnitude of the step size in the search direction, which had decreased below $1 \cdot 10^{-10}$.

The optimized result, \mathbf{x}^* , is:

$$\begin{aligned}\mathbf{x}^*(1) &= b/2 = 0.235[m] \\ \mathbf{x}^*(2) &= c_{root} = 0.169[m] \\ \mathbf{x}^*(3) &= \Lambda = 37.131[^\circ] \\ \mathbf{x}^*(4) &= \lambda = 0.5[-] \\ \mathbf{x}^*(5) &= V_\infty = 19.05[m/s]\end{aligned}$$

The twist corresponding to this \mathbf{x}^* , airfoil and stability margin, is -6.56° . The S5010 airfoil was selected, before the optimization, for both the root and tip airfoil. In figure 6.1 the difference can be seen between the initial wing and the resulting new geometry.

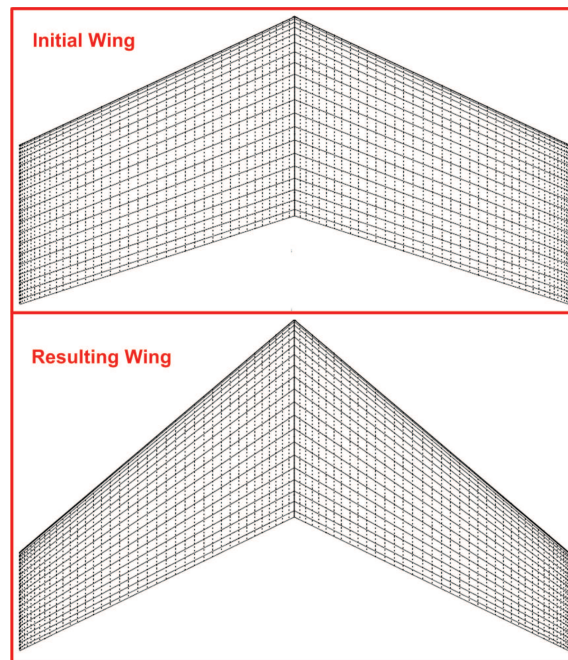


Figure 6.1: Comparison between the initial wing geometry and the resulting geometry after the optimization.

From figure 6.1 and \mathbf{x}^* it is clear that the optimizer tried to get the highest possible aspect ratio. This was accomplished by having the span at the upper bound, while the root chord and the taper ratio were forced to the lower bound. This increased the aspect ratio from 3.07 to 3.71, with the most likely result of reducing the induced drag. When evaluating the non-linear constraints it is noted that non of them are actually active. The stall speed limit is getting close with $11.89m/s$.

Range Performance

The lift and drag coefficients for the optimized wing were calculated after the optimization, and can be seen in figure 6.3. The maximum lift over drag is 12.76 at a lift coefficient of 0.457. The optimizer however established a value of 12.65 to be the optimum at a lift coefficient of 0.37 ($V_\infty = 19.1m/s$). This however does not mean that the optimizer has not found the optimum. To go up to the $C_L = 0.457$ it requires less speed to remain in a straight level flight. Changing this requires the twist to decrease further and the Reynolds number lowers, resulting in more profile drag. Calculating the lift over drag ratio by changing the velocity, but remaining in straight level and trimmed flight, gives the plot as can be seen in figure 6.2. From this figure it is clear that the maximum lift over drag ratio is obtained at $19m/s$ as was obtained with the optimizer.

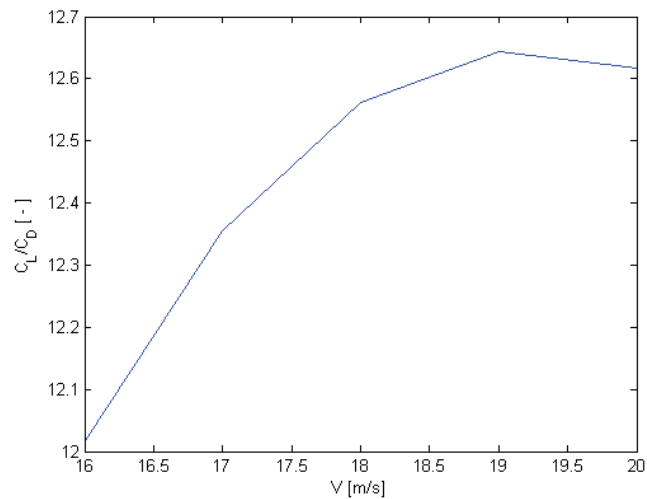


Figure 6.2: Lift over drag ratio for different velocities, maintaining straight, level and trimmed flight.

The total distance that can be flown, using the propulsive system as described in section 6.2.2 and a battery capacity of $4.27Ah$, can be calculated using equation 3.60. The subsystems are assumed to consume about $5W$ which corresponds to a subsystem current of $0.71A$. This results in a total range of:

$$R = 103.8 \text{ km}$$

For the starting point of the optimization this was $100.4km$, which was obtained with an lift over drag ratio of 11.91 and a velocity of $20m/s$. This means an improvement of about 3.4%

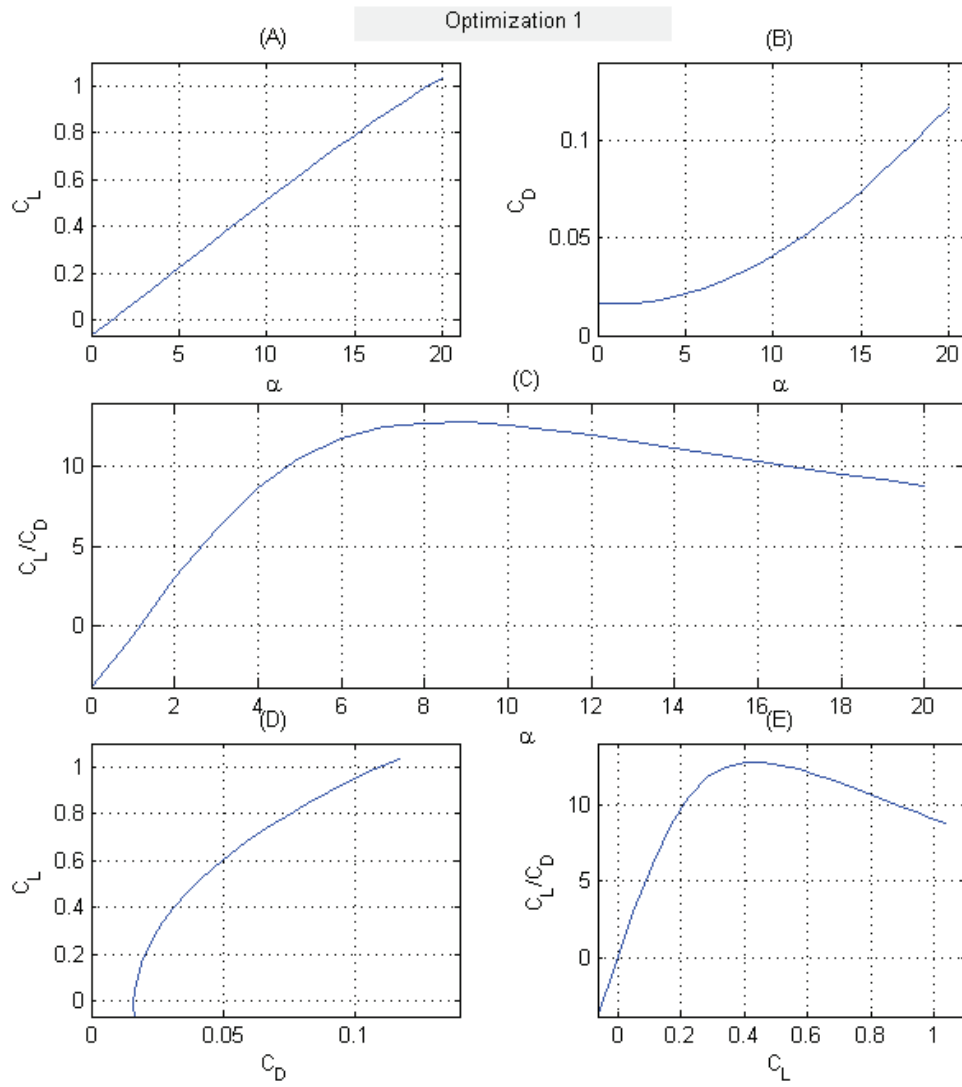


Figure 6.3: Aerodynamic coefficients for the optimized wing at 19.1m/s.

6.1.2 Optimization with Tight Constraints and an Inferior Initial Point

Mathematical Description of the Problem

The mathematical description of this problem only differs, compared to the one in section 6.1.1, in the initial point, which is changed into:

$$\begin{aligned} \mathbf{x}_0(1) &= 0.15 \\ \mathbf{x}_0(2) &= 0.17 \\ \mathbf{x}_0(3) &= 10 \\ \mathbf{x}_0(4) &= 1 \\ \mathbf{x}_0(5) &= 35 \end{aligned}$$

Optimized Geometry

First of all it is interesting to see how the result of this optimization compares to the one previously obtained from a better starting point. The first difference that could be noted was the number of iterations and function evaluations needed to obtain the optimum. This optimization required 24 iterations, 11 more than the first optimization, and 213 function evaluations. This resulted in a total running time of about 47 hours, which is a 60% increase in the calculation time. From this it can be concluded that starting at a good initial point might save quite some time.

The result of this optimization matches closely with the results obtained from the first optimization. The optimized \mathbf{x} is the following:

$$\begin{aligned} \mathbf{x}^*(1) &= b/2 = 0.235[m] \\ \mathbf{x}^*(2) &= c_{root} = 0.169[m] \\ \mathbf{x}^*(3) &= \Lambda = 35.608[^\circ] \\ \mathbf{x}^*(4) &= \lambda = 0.5[-] \\ \mathbf{x}^*(5) &= V_\infty = 19.286[m/s] \end{aligned}$$

The difference between this result and the previous optimization is in the sweep angle and the velocity. The sweep angle only differs by about 1.5° and is most probably caused by the very small gradient in the lift over drag with respect to the sweep angle, as was observed in section 4.3. The very small velocity difference probably is related to the discrepancy in the sweep. It can be concluded that the optimization works well even when the initial estimate is far from the optimal point. The twist for trimmed flight was determined to be -6.87° , and the airfoil, for the root and tip, was the S5010.

The geometry comparison between the result obtained in the previous optimization and in this optimization can be seen in figure 6.4, which clearly illustrates the strong similarity between them.

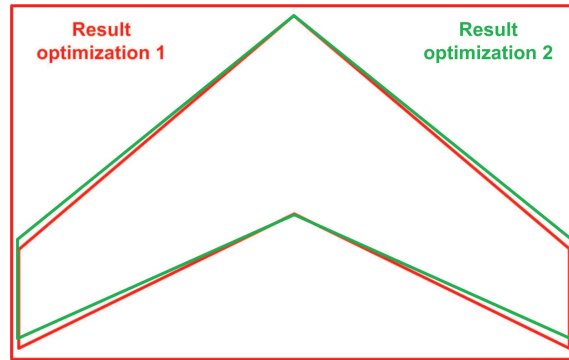


Figure 6.4: Comparison between optimized wing from section 6.1.1 (red) and the optimization of this section (green).

Range Performance

The optimizer established that the maximum lift over drag ratio is 12.651, which is only $6 \cdot 10^{-3}$ higher than the first optimization, showing the extremely small gradient involving the sweep ($0.004 \frac{1}{deg}$). The calculated aerodynamic coefficients can be seen in figure 6.5, and once again the $(\frac{C_L}{C_D})_{max}$ is higher than found by the optimizer. However the same explanation as in section 6.1.1 applies to this wing.

The change in the maximum range between the initial wing and the optimized result is rather impressive for this optimization. The starting wing had a range of $76 km$ while the optimized wing attained a flying distance of:

$$R = 104.2 \text{ km}$$

The gain in range over the optimization is $28.2 km$, which is an increase of 37%.

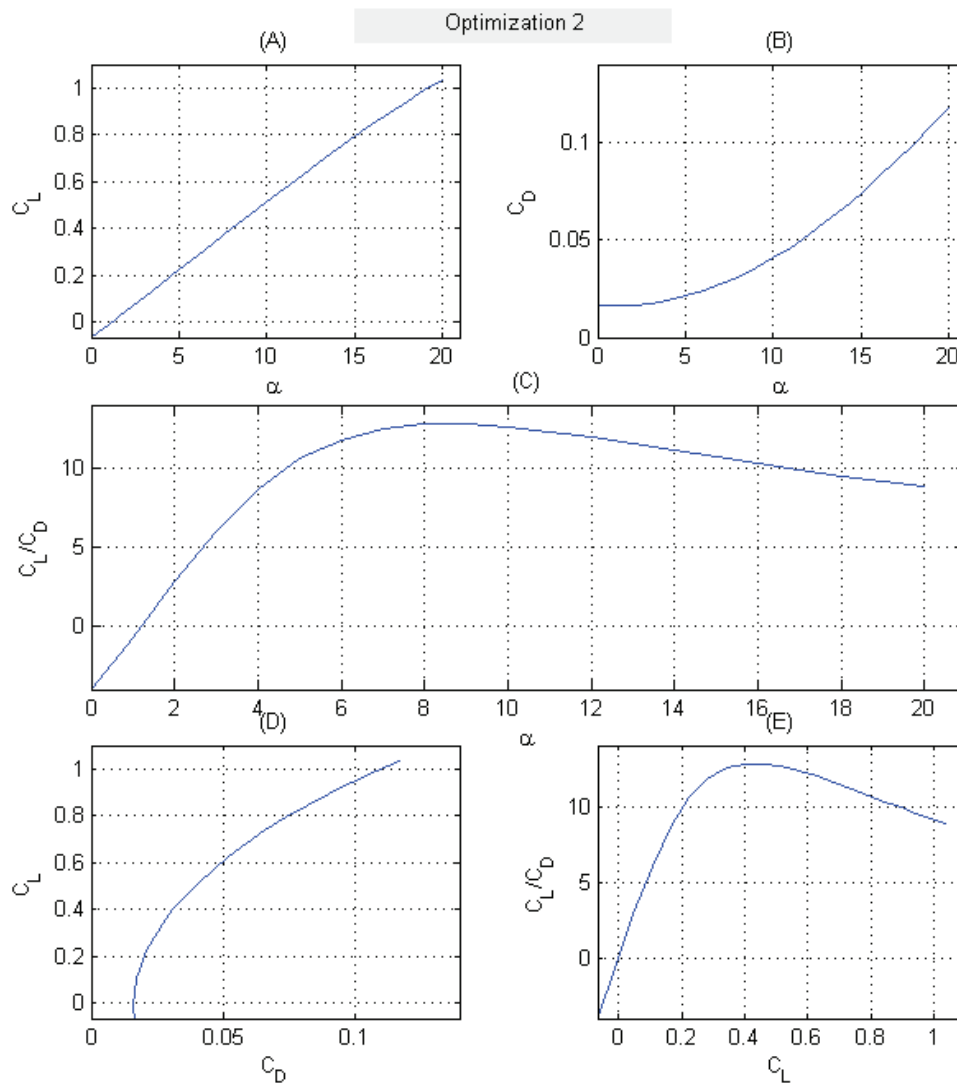


Figure 6.5: Aerodynamic coefficients for the optimized wing at 19.3m/s.

6.1.3 Optimization with Relaxed Constraints

Mathematical Description of the Problem

For this problem the mathematical description remains the same as in section 6.1.1. The only differences are the linear constraints and the initial point. These are transformed into:

Linear constraints:

$$\begin{aligned} 0.05 &\leq \mathbf{x}(1) \quad , \quad \mathbf{x}(1) \leq 0.235 \\ 0.03 &\leq \mathbf{x}(2) \quad , \quad \mathbf{x}(2) \leq 0.5 \\ 0 &\leq \mathbf{x}(3) \quad , \quad \mathbf{x}(3) \leq 40 \\ 0.2 &\leq \mathbf{x}(4) \quad , \quad \mathbf{x}(4) \leq 1 \\ 10 &\leq \mathbf{x}(5) \quad , \quad \mathbf{x}(5) \leq 35 \end{aligned}$$

Initial point:

$$\begin{aligned} \mathbf{x}_0(1) &= 0.235 \\ \mathbf{x}_0(2) &= 0.2 \\ \mathbf{x}_0(3) &= 10 \\ \mathbf{x}_0(4) &= 0.5 \\ \mathbf{x}_0(5) &= 25 \end{aligned}$$

Optimized Geometry

After 50 hours, 27 iterations and 228 function evaluations the optimization terminated with the following result:

$$\begin{aligned} \mathbf{x}^*(1) &= b/2 = 0.235[m] \\ \mathbf{x}^*(2) &= c_{root} = 0.1946[m] \\ \mathbf{x}^*(3) &= \Lambda = 31.683[^\circ] \\ \mathbf{x}^*(4) &= \lambda = 0.28[-] \\ \mathbf{x}^*(5) &= V_\infty = 19.236[m/s] \end{aligned}$$

The visual presentation of this result can be seen in figure 6.6. In this case it is clear that the optimizer tried to establish the highest possible aspect ratio within the non-linear constraints. The linear constraint on the span and the non-linear constraint on the stall speed, together establish the maximum aspect ratio that can be achieved. For this optimization this is:

$$A_{max} = \frac{b_{max}^2}{S_{min}} = \frac{b_{max}^2 \rho V_{stall_{max}}^2 C_{L_{max}}}{2 \cdot W} = 3.77$$

The aspect ratio for the optimized wing is exactly the same. This implies that the stall speed constraint is active. The other nonlinear constraints are not active however the twist is -9.83° which is very close to the maximum 10° . This value is rather high and such a result must thus be treated with care. The airfoil used at the root and tip is once again the S5010.

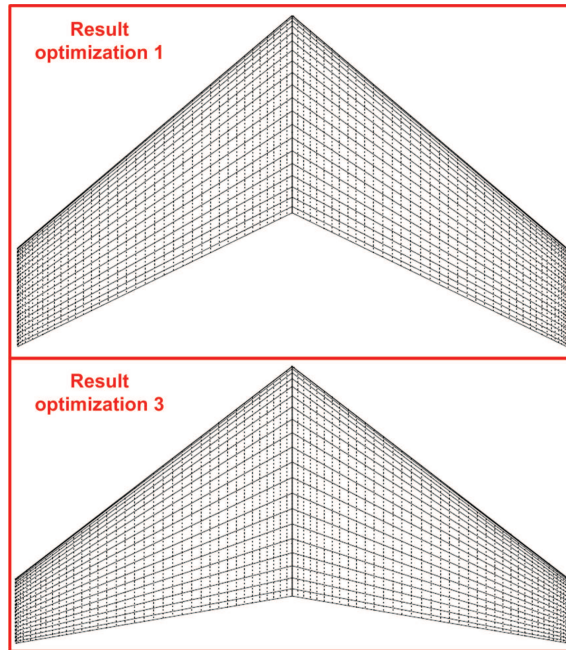


Figure 6.6: Comparison between optimized wing from section 6.1.1 (upper) and the optimization of this section (lower).

Range Performance

The lift over drag ratio for this wing improved from 10.9 for the initial wing to 13.0 for the optimized design. This lift over drag ratio is established at a lift coefficient of 0.369. However the maximum lift over drag ratio in figure 6.7 is 13.13 at a lift coefficient of 0.416. Like before, reaching this lift coefficient requires more twist and thus more drag reducing the lift over drag ratio again.

The total distance this airplane can fly with a battery capacity of $4.27Ah$ and subsystems consuming the same energy as before, is:

$$R = 106.2 \text{ km}$$

With respect to the first optimization result this is only $2.4km$ difference and with respect to the prototype, used as initial point for the first optimization, this is a difference of $5.8km$.

Based on this it can be concluded that creating a new design and new molds is too expensive for an increase in range of only 6%. This range might even be compromised as it is not certain that the same amount of battery capacity still fits in the wing. A better option is to look at the batteries and see if something can be gained in increasing their capacity for the prototype aircraft. This topic will be discussed in section 6.2.2.

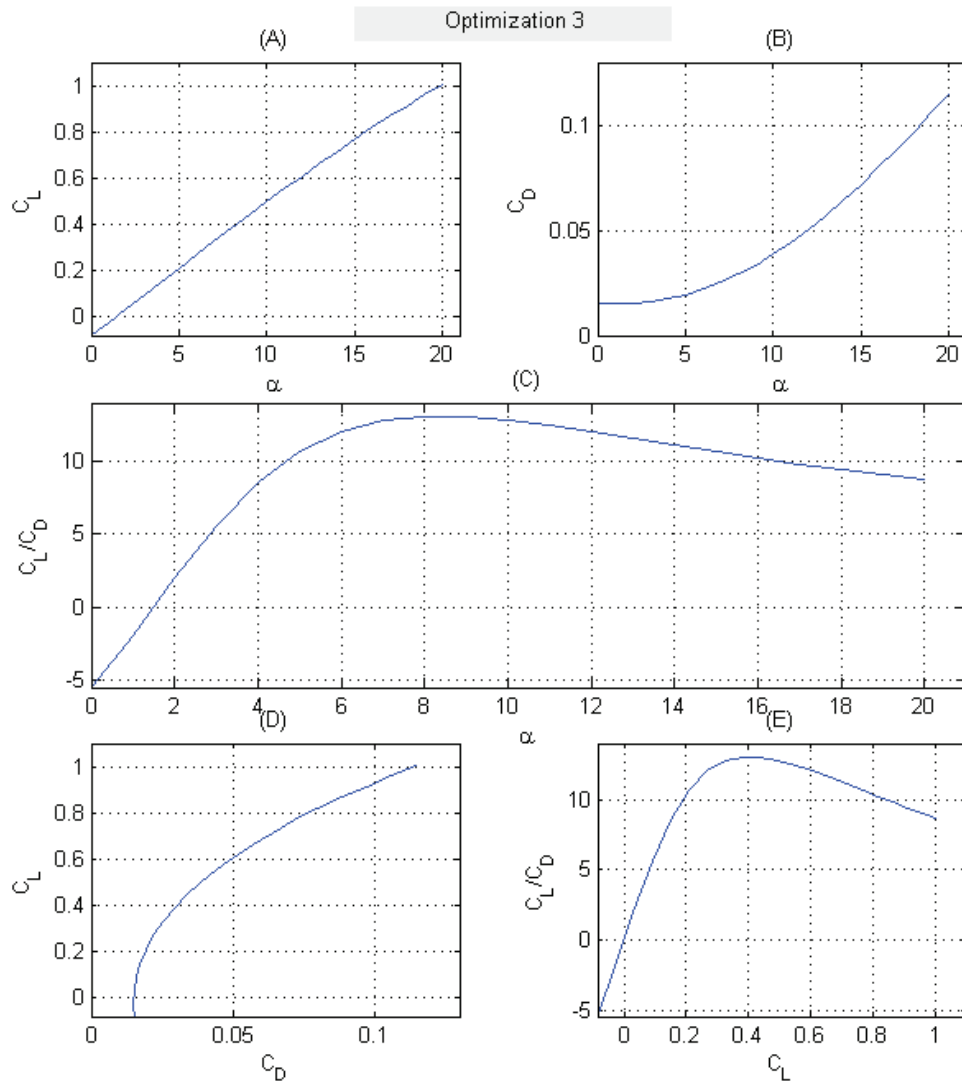


Figure 6.7: Aerodynamic coefficients for the optimized wing.

6.2 The Competition Aircraft

The first prototype was selected as the competition aircraft (further referred to as TRIP50). The reason for selecting this aircraft was based on several arguments. Two major factors were the time available and the budget. They did not allow for the production of new molds and building the new aircraft. At the same time the maximum range of the prototype did not improve too much during an optimizations. Another fact was that a lot of experience had been gained in building this aircraft.

6.2.1 Geometric and Structural Details

The aircraft consists out of a single wing, a fuselage and a tail. A three-view of the TRIP50 can be seen in appendix D.

Wing

The wing has a single tapered shape with a S5010 airfoil at the root and the tip of the wing. The S5010 was selected based on the fact that it is designed for low Reynolds numbers, it has a low moment coefficient, and it has a thickness to chord ratio of 10% providing sufficient space in the wing. The Xfoil results for this airfoil at a Reynolds number of $2 \cdot 10^5$ can be seen in figure 6.8.

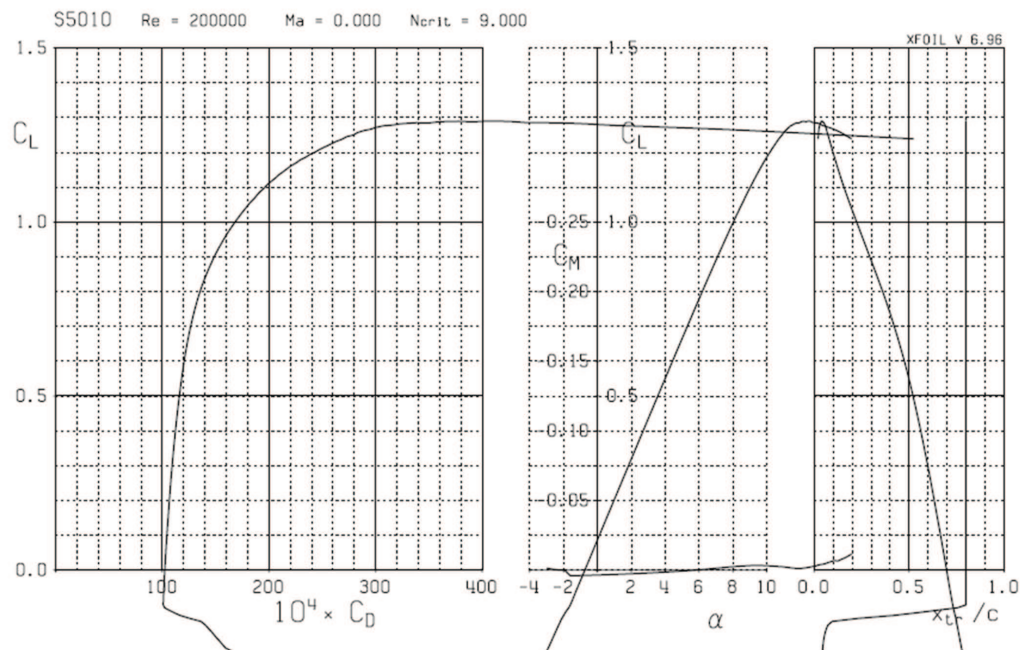


Figure 6.8: polars for the S5010 airfoil at a Reynolds number of $2 \cdot 10^5$.

The TRIP50 wing planform is defined as described in table 6.1, and can be seen in the upper drawing of figure 6.1.

Table 6.1: Wing planform of the TRIP50.

	b	c_{root}	λ	$\Lambda_{0.25}$	ϵ	S	A	c_{mac}
	[m]	[m]	[–]	[deg]	[deg]	[m ²]	[–]	[m]
TRIP50	0.47	0.17	0.8	23.3	-3	0.0719	3.1	0.154

The wing is made out of an upper and a lower shell. These shells are made from an outer layer of $50gr/m^2$ glass-fibers and an inner layer of $36gr/m^2$ Kevlar-fibers. The fibers have a 0-90-orientation but are put under 45° with respect to the trailing edge of the wing to provide torsional stiffness. A low-density polystyrene foam core is located in between those shells, to provide form-rigidity to the shells and to facilitate locating components in the wing. Parallel to the leading edge, at $75mm$ from it, a spar of carbon fiber is located to take the bending loads and to act as part of the torsion box.

Fuselage & Vertical Tail

The fuselage and the tail form a single construction element. The fuselage is $250mm$ long and has a circular cross-section with a diameter of $43mm$ at the thickest point. A detailed description of the fuselage geometry can be found in reference [9]. The tail is a single tapered surface with a naca0012 airfoil. The planform details of the tail are presented in table 6.2.

Table 6.2: Tail planform of the TRIP50.

	b	c_{root}	c_{tip}	Λ_{LE}	ϵ	S	c_{mac}
	[m]	[m]	[m]	[deg]	[deg]	[m ²]	[m]
TRIP50	0.08	0.1	0.06	35	0	0.0064	0.0817

The fuselage-tail structure is build up out of $50gr/m^2$ glass fibers for the tail and $110gr/m^2$ Kevlar for the fuselage itself. The tail is constructed out of two layers of glass fiber with a Rohacell core in between to provide form-rigidity. The fuselage is mainly constructed out of a single layer of Kevlar however at certain points, like the nose and the edges just above the wing, an extra layer is added to withstand hard landings.

6.2.2 Aircraft Components

Propulsion System, Power Source and Electronics

In this section a general outline of the electronics will be presented and a visual overview can be seen in figure 6.9. However not much attention will be given to the autopilot nor on the other electrical components, except for the propulsion system as this is important for the range performance.

The autopilot was especially designed for this competition by the TU Delft MAVLab. The autopilot uses infra-red sensors to establish its attitude and GPS for its position. A picture of the autopilot inside the aircraft can be seen in figure 6.10. The communication with the ground station is established using a 2.4GHz Xbee transceiver. For safety purposes

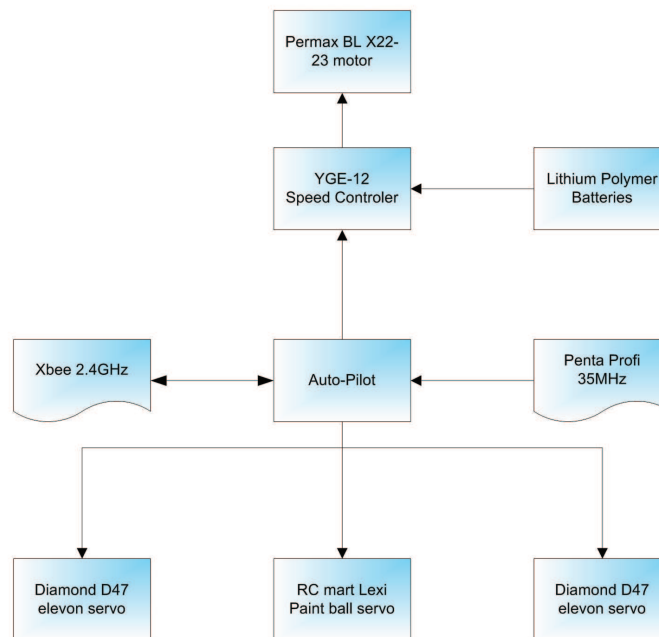


Figure 6.9: General overview of the electric layout for the EMAV2009 competition aircraft.

it was required to be able to manually override the autopilot which required a 35MHz receiver. The “Penta Profi” was selected as the receiver based on its weight and size.

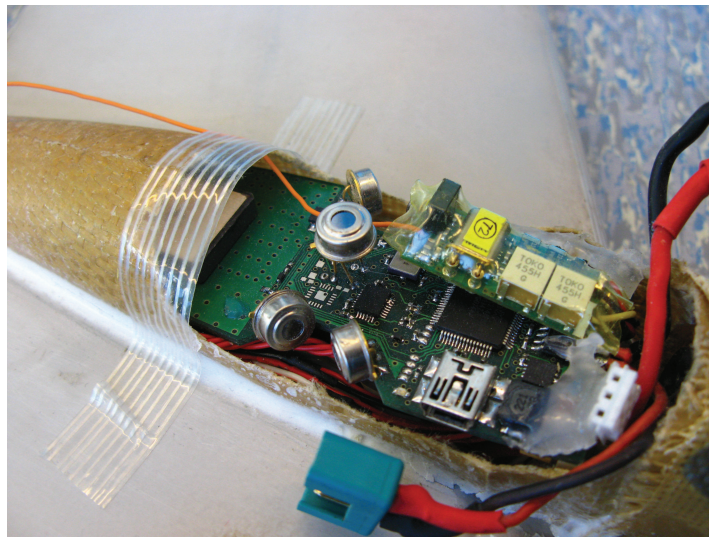


Figure 6.10: Autopilot build into the prototype aircraft.

Three servos were required, two of which controlled the elevons and one for the paint ball drop mechanism. The original idea was to use “RC MART Lexi” servos for the elevons and drop mechanism as they only weigh 2.5gr. However they proved not strong enough

for the elevons and were thus changed for 4.7gr “Diamond D47” servos.

Design of the Propulsive System

This subject was originally part of this assignment but due to the overload of work it was decided to split it into a DAR-exercise. Optimizing the aerodynamics with a certain weight and size for the propulsion system made it possible to see them as separate parts. However this still required information to be passed between the two disciplines to ensure a good design.

Establishing the design of the propulsive system was the topic of the DAR-exercise, reported upon in reference [14]. The final design established in the exercise will be summarized here.

Electrical propulsion was set as a requirement in the EMAV2009-rules. Such a system is build up out of a propeller, a motor, a motor controller and the power source in the form of batteries.

A brushless DC-motor was selected for their higher efficiency and higher power to weight ratio, over brushed motors. For simplicity a direct drive was selected which implicitly requires an outrunner motor. An outrunner, compared to an inrunner, has a lower rpm but a higher torque, both necessary for a direct drive.

The power source would have to be a type of rechargeable batteries. The best option were the Lithium-polymer batteries, as they are light weight while having a high capacity, and no memory problems. A 2 cell battery pack was selected as this provided the highest level of flexibility to locate the batteries and to resort to larger batteries.

Several motor-propeller-battery combinations were evaluated, using Drive calculator, to achieve the highest efficiency. The motor controller was purely selected on the weight. The final combination is as follows:

- Motor: Permax BL X22-23
- Propeller: 4.7×4.7 Graupner
- Battery: Enerland Polyquest 4270LP
- Motor controller: TMM1210-3 PL auto

See reference [14] for more details on the design, selection and technical specifications.

This combination for the propulsive system was applied in the prototype. However during the first test flights the pilot was forced to land as the motor controller stopped working when applying full throttle. This was the reason to change the “TMM1210-3 PL auto” with a “YGE-12” speed controller. Another problem was the propeller breaking at every landing. The Graupner type was then switched for a “ 4.75×4.75 ACP”, which proved to survive 2 to 3 landings.

Improved Battery Capacity

It was clear that the range also depended on the battery capacity. However as the battery capacity increases the total aircraft weight increases as well. A small investigation was performed to establish if it was possible to find a capacity that would optimize the range.

Assuming the aircraft shape, for this case the prototype aircraft, is fixed and that every possible battery fits within this shape. By changing the velocity, such that the lift coefficient was kept constant for the different battery weights, equation 3.60 was used to establish the maximum range. The lift over drag ratio was also assumed constant. The subsystems consume about 5 Watt or a corresponding $I_{sub} = 0.71A$. The weight of the battery varied linearly with the battery capacity, using the energy density (capacity divided by the weight). The total propulsive efficiency, from battery to propeller, was set equal to 0.5, while the battery tension was maintained at 7 Volt (two cell configuration). This resulted in figure 6.11.

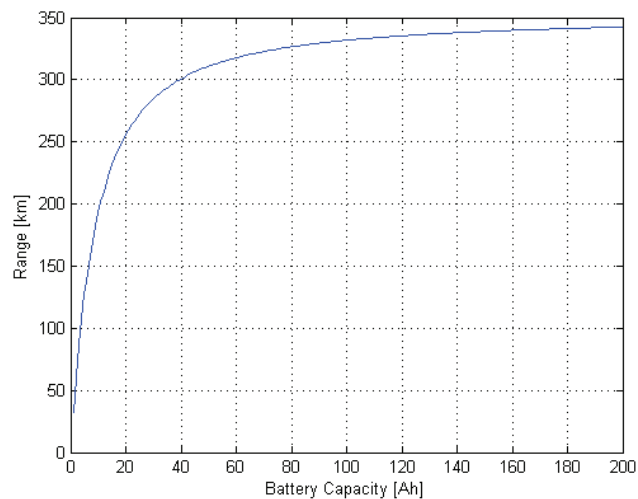


Figure 6.11: Range plotted against the battery capacity (ranging from 0-200 Ah), for a fixed aircraft shape with a varying weight with respect to the battery capacity, and a 5W subsystem power consumption.

This figure shows that the range keeps increasing towards an asymptote. Thus it could be concluded that the largest battery that still fits in the aircraft, and whose weight does not compromise the stall speed, must be used. That was the reason to start looking for a battery that meets those requirements, which resulted in a 8Ah Hellpower Lithium polymer battery. This change in battery increased the range from 113.5 km to 170.8 km (see figure 6.12), taking into account the above mentioned assumptions. The flight time increased to 2h9min at a velocity of 22m/s.

Weight

Details on the weight for each component are presented in table 6.3, from which it can also be seen that the aircraft weight is 575gr.

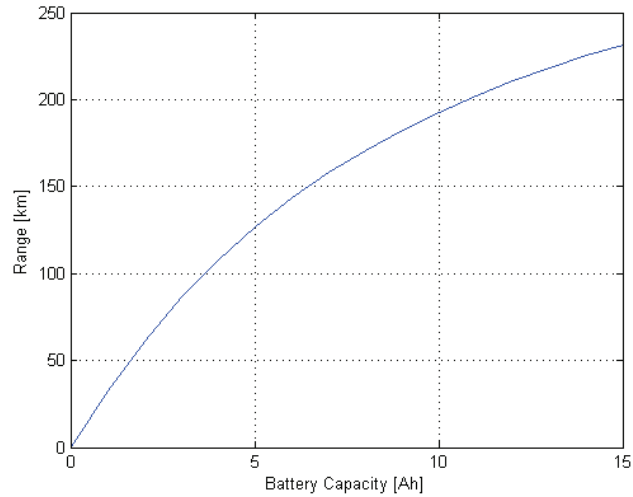


Figure 6.12: Range plotted against the battery capacity (ranging from 0-15 Ah), for a fixed aircraft shape with a varying weight with respect to the battery capacity, and a 5W subsystem power consumption.

The original design weight of the aircraft was 500gr but due to the increased battery size the weight increased with 75gr. This required a small increase of the velocity to maintain the lift coefficient that corresponded to the maximum lift over drag ratio, which meant that the elevons had to be deflected down a small amount to maintain straight, level and trimmed flight.

Layout

The location of all components in the aircraft can be seen in figure 6.13. They were positioned such that they located the center of gravity exactly as required by the stability margin and the location of the neutral point. The location of the neutral point and the center of gravity are illustrated in the 3-view in appendix D, from which it can be deduced that the stability margin is 2.7%. This seems low but a small margin provides the autopilot with a lot of pitch control, meaning that a small deflection of the elevons has a large effect on the pitch angle. A small stability margin makes the airplane more sensitive to gusts however the wing loading of the TRIP50 is rather high for a mini-UAV, $78.4N/m^2$, making it less sensitive to gusts.

6.2.3 Aerodynamics and Performance Details

The aerodynamic coefficients for the TRIP50 can be seen in figure 6.14 for a velocity of 20m/s. The drag for the fuselage and the tail are taken into account by adding a constant drag coefficient to the polar. These constants are:

$$\begin{aligned} C_{D_{fus}} &= 0.002 \\ C_{D_{tail}} &= 0.0016 \end{aligned}$$

Table 6.3: Weight breakdown of the TRIP50.

wing structure	85	gr
fuselage structure	13	gr
batteries	354	gr
motor	35	gr
speed controler	6.8	gr
propeller	5	gr
reciever	4.5	gr
auto-pilot	36	gr
xbee-transciever	3.5	gr
elevon-servos	9.6	gr
servo torsion rods	8	gr
paintball servo	2.95	gr
paintball tube	1.5	gr
cables	10	gr
TOTAL	574.85	gr

Both these drag coefficients are with respect to the wing surface area.

The maximum lift over drag coefficient is equal to 12.31 and is obtained at a flight speed of $19.88m/s$ ($C_L = 0.324$). The moment coefficient at the maximum lift over drag ratio is equal to $4.4 \cdot 10^{-3}$ in stead of the required $8.75 \cdot 10^{-3}$. This is not sufficient to trim the aircraft which has a twist of -3° instead of the required -7.6° . This can be compensated for by deflection of the elevons up generating a higher positive moment. This however comes at the cost of increased drag and thus lowering the lift over drag ratio, which is also the case for increasing the twist. Twisting the wing to -7.6° lowers the lift over drag ratio to 11.76. Taking this value for the lift over drag ratio, assuming the subsystems use $5W$ (which translates to a current of $0.71A$ at a tension of $7V$) and a battery capacity of $8Ah$ gives a range of:

$$R = 166.7 \text{ km}$$

, and a flight time of 2 hours and 20 minutes.

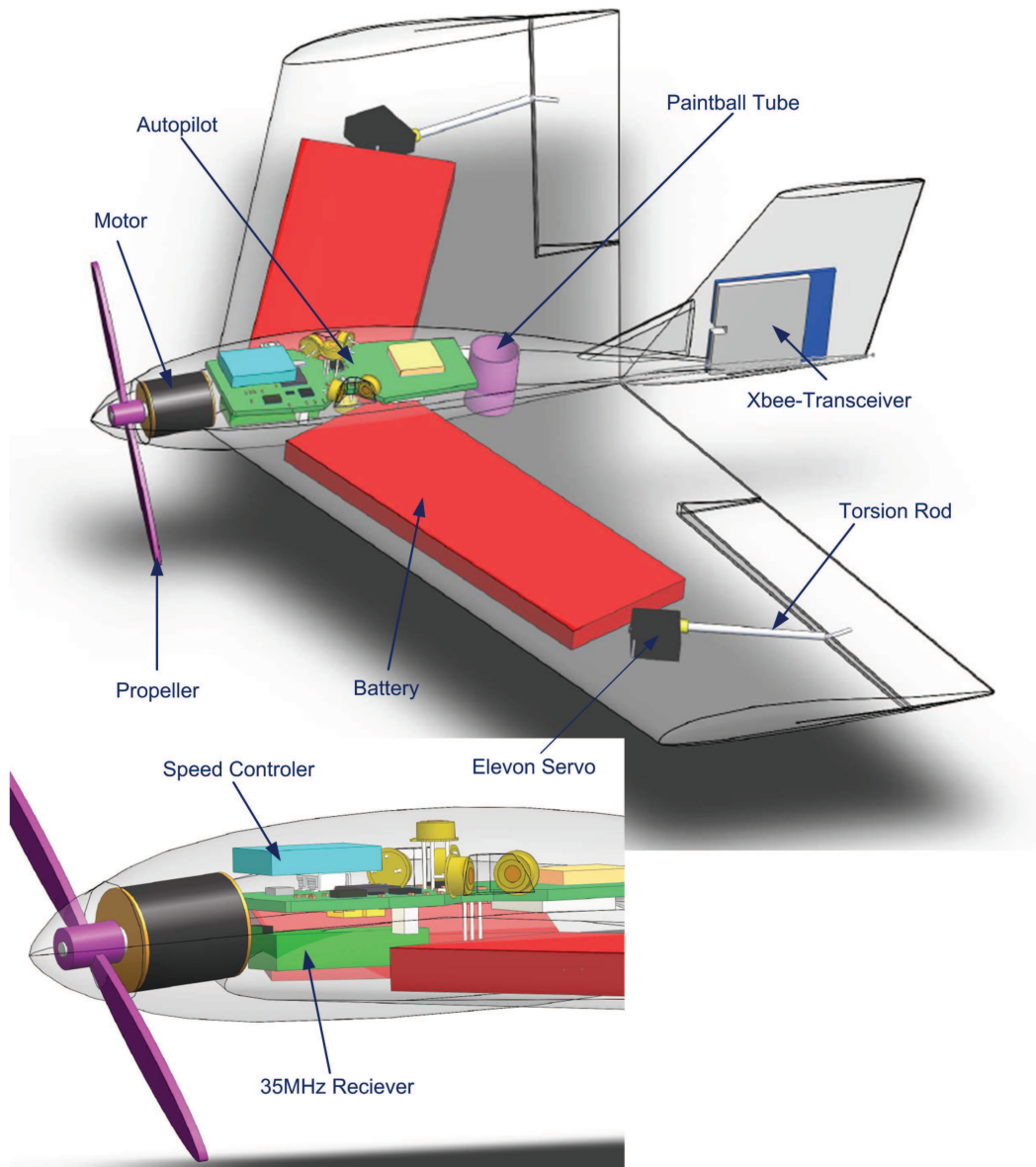


Figure 6.13: Subsystem locations in the aircraft.

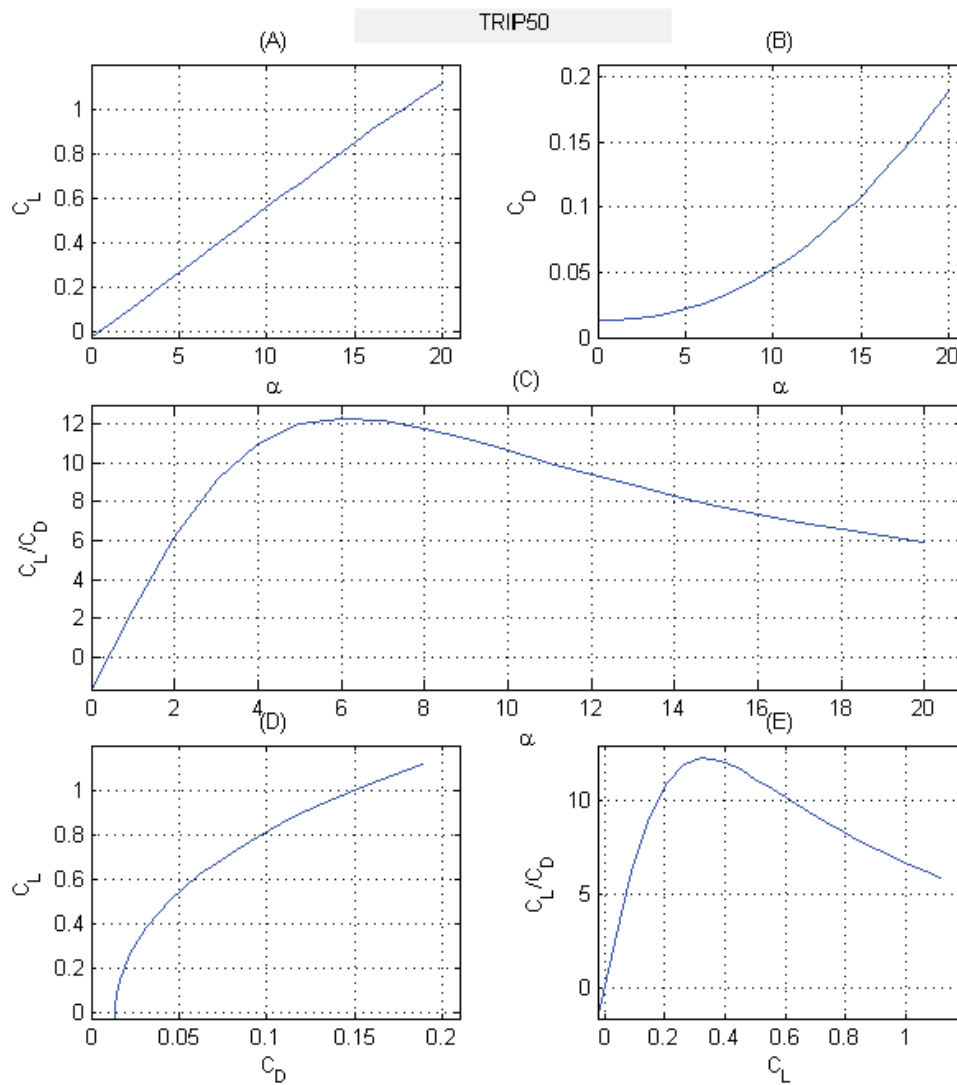


Figure 6.14: Aerodynamic coefficients for the TRIP50 aircraft at 20m/s.

Conclusions and Recommendations

7.1 Conclusions

At the start of this thesis the following project goal was stated:

Design of a mini-UAV for the EMAV 2009 outdoor competition using a novel aerodynamic optimization tool, with the objective to win the competition.

The EMAV 2009 outdoor competition has 3 phases, consisting of flying as far as possible towards a goal, dropping a paint ball, and flying the same distance back. The focus of the competition is mainly on the range performance, that is why this thesis expands on this topic.

To reach the above stated goal an in dept theoretical analysis of the aerodynamics involved was performed. The conclusion of this was that a quasi-3D method would yield the best results considering requirements on computational effort, automatic creation of the computational domain and capability to handle low Reynolds numbers ($< 2.5 \cdot 10^5$). These requirements were set forward by the fact that this analysis tool was going to be implemented in an optimization environment. The quasi-3D method uses a vortex lattice method to simulate the three dimensional aerodynamics and Xfoil results are put on top of the vortex lattice results to obtain information on the profile drag. The exact implementation of this method is presented and a detailed validation is performed against a RANS-CFD method and wind tunnel results obtained from literature. The validations proved that the accuracy of the maximum lift over drag ratio remained within 4%. The wings used for validation varied in sweep, taper ratio, aspect ratio and twist.

The quasi-3D method was then submitted to an optimization algorithm that would be used to established the best wing shape for long range flight. The variables for the optimization would consist out of 4 geometric variables and 1 flow variable. The 4 geometric variables are the wing span, root chord, quarter chord sweep angle and the taper ratio. The velocity is the only flow variable. Apart from these variables several constants are

required. The most important ones are the weight of the aircraft and the stability margin. The other constants are used to establish the fuselage and tail drag, and the values for the constraints. Based on these inputs two values are determined in the objective function, one is the twist angle required to maintain trimmed straight horizontal flight, and the second one is the objective value. The objective functions for range performance of electrically powered propeller aircraft are presented. The lift over drag ratio is taken as the objective for the optimizations presented in this thesis however a better approximation can be attained when the power consumed by the non-propulsive subsystems is taken into account. The domain of the optimization variables was limited by linear and non-linear constraints. These constraints served the purpose to limit the search domain such that a valid design could be obtained.

The optimization algorithm was selected based on its efficiency, ability to find a global minimum in the objective domain and ability to handle linear and non-linear constraints. This resulted in selecting the sequential quadratic programming algorithm as the best option. The requirement for this algorithm to find a global minimum could not be confirmed, due to the intricate way in which the objective value is calculated. It was however verified that the same final result was obtained for different initial points.

Two wind tunnel campaigns were performed to establish the performance of the optimization tool and the quasi-3D method. The required data from the wind tunnel tests, to obtain this goal, were force measurements and boundary layer visualizations. The low speed low turbulence wind tunnel of the TU Delft was selected for the measurements. The required tools for the boundary layer visualizations were available at this facility. The resolution for the force balance, available in the wind tunnel, was too low for the small drag forces on mini-UAV's. This thus required the construction of a new balance with a higher resolution. This resulted in selecting a very accurate force transducer (ATI nano17) for which a yaw-pitch system was build to be able to set the required pitch angles and side slip angles during the measurements.

The force measurements appeared to have major errors in them due to problems with the yaw-pitch system of the balance. A detailed description of the problems with the yaw-pitch system are presented together with an overview of the effects they have on determining the aerodynamic coefficients. The boundary layer visualizations on the other hand proved to be vary useful in understanding the phenomena in the boundary layer at low Reynolds numbers and different angles of attack. They also provided information on what happens on the wing when the propeller is blowing air over it, or what happens when the elevons are deflected.

This thesis work created several spin-offs in the form of 4 DAR-exercises. These exercises focused on producing wind tunnel models and their molds, designing and building the wind tunnel balance, and designing the propulsion system for the competition aircraft. The help obtained from these exercises made the practical execution of this research possible.

In the final stages of the thesis work three different optimizations were performed to establish which design would be selected to become the competition aircraft. The conclusion of this was that the first prototype would be the best option. The only change to it was the battery size which increased the range by 66%. The range this aircraft can fly is *166.7km*.

It could however not be established if the above mentioned goal was obtained. The day of the competition was very rainy, resulting in wet vegetation which had the same temperature as the sky. The autopilot needs a temperature difference between the sky and the ground to establish its attitude with the infra-red sensors. All competitors had the same problem resulting in the competition being canceled.

7.2 Recommendations

A summary of the recommendations will be presented on which future work might expand.

Quasi-3D method:

- Improving the determination of the induced downwash angle such that the induced drag can be determined using the quasi-3D technique.
- Improving the estimation of the zero lift angle of attack.
- Improving the estimation of the vortex parameter K_v for swept and tapered wings.
- Improving the lift over drag estimation for swept wings such that its gradient is better estimated.
- Implement the interpolation of forced transition points for the airfoil data.
- Include and validate dihedral in the geometry.
- Improve and validate the determination of the maximum lift coefficient by the quasi-3D method.

Optimization tool:

- Include altitude in the optimization.
- Better implementation of the airfoils in the optimization, maybe even including shape optimization of the airfoils.

Wind tunnel Balance:

One of the improvements that has to be in place before new wind tunnel force measurements are performed, is a feedback loop between the required input angles and the measured angles at the head of the yaw-pitch system. It might even be necessary to completely redesign this system taking into account the experience obtained with this balance.

On the software side it would be convenient if:

- The aerodynamic coefficients could be evaluated real time during the wind tunnel measurements.
- The windtunnel settings and the atmospheric data are logged automatically.

Bibliography

- [1] Matlab help files on: Constraint optimization, sequential quadratic programming, August 2007. Matlab Version 7.5.0.342(R2007b).
- [2] Emav 2009 website, December 2008. www.emav09.org.
- [3] Tu delft lst website, December 2009. <http://www.lr.tudelft.nl/live/pagina.jsp?id=2cbe9c14-0aa6-4efa-b128-bb006b447210&lang=en>.
- [4] Xfoil website, January 2009. <http://web.mit.edu/drela/Public/web/xfoil/>.
- [5] Raymond F. Anderson. Determination of the characteristics of tapered wings. Naca report 572, National Advisory Committee for Aeronautics, 1936.
- [6] Raymond F. Anderson. The experimental and calculated characteristics of 22 tapered wings. Naca report 627, National Advisory Committee for Aeronautics, 1938.
- [7] Ir. L.L.M. Boermans. Aerodynamic design of aircraft and advanced transportation systems. In *Part I*. Delft University Copy Machine, 1998.
- [8] Ir. L.L.M. Boermans. Aerodynamic design of aircraft and advanced transportation systems. In *Part II: The Real Case*. Delft University Copy Machine, 1998.
- [9] B.A.P Bruggeman. Designing and constructing the molds for emav2009 uav. DAR-exercise Report.
- [10] P.D. Chappell. Wing pitching moment at zero lift at subcritical mach numbers. Esdu 87001, ESDU international, 1991.
- [11] T.M.T. Doornbos. Building the half meter uav for emav2009. DAR-exercise Report.
- [12] Mark Drela. Low-reynolds-number airfoil design for the m.i.t. daedalus prototype: A case study. *Journal of Aircraft*, 25(8):724–732, 1988.
- [13] B.F.R. Ewald (Editor). Wind tunnel wall corrections. Agard-ag-336, AGARD, October 1998.

-
- [14] Vinodh Kumar Gunaseelan. Design of propulsive system for micro aerial vehicle and wind tunnel measurement system. DAR-exercise Report.
- [15] S.F. Hoerner. *Fluid-Dynamic Drag*. Hoerner Fluid Dynamics, june 1965.
- [16] John E. Lamar. Extension of leading-edge-suction analogy to wing with separated flow around the side edges at subsonic speeds. Nasa-tr-r-428, NASA Langley Research Center, October 1974.
- [17] John E. Lamar. Prediction of vortex flow characteristics of wings at subsonic and supersonic speeds. *Journal of Aircraft*, 13(7):490–494, 1976.
- [18] Hillier Lieberman. *Introduction to Operations Research*. McGraw-Hill, eight edition, 2005. ISBN 007-123828-X.
- [19] Karl Nickel and Michael Wohlfahrt. *Tailless Aircraft in Theory & Practice*. American Institute of Aeronautics and Astronautics, 1994. ISBN 0-340-61402-1.
- [20] P.cosyn and J. Vierendeels. Numerical investigation of low-aspect-ratio wings at low reynolds numbers. *Journal of Aircraft*, 43(3):713–722, 2006.
- [21] W.F. Phillips and D.F. Hunsaker. Estimating the subsonic aerodynamic center and moment components for swept wings. *Journal of Aircraft*, 45(3):1033–1043, 2008.
- [22] E.C. Polhamus. Prediction of the vortex-lift characteristics by a leading-edge-suction analogy. *Journal of Aircraft*, 8(4):193–199, 1971.
- [23] Alan Pope. *Wind-Tunnel Testing*. John Wiley & Sons, Inc., New York and Chapman & Hall, Limited, London, second edition, 1954.
- [24] Singiresu S. Rao. *Engineering Optimization: Theory and Practice*. John Wiley & Sons, fourth edition, 2009. ISBN 978-0-470-18352-6.
- [25] M. Selig, C. Lyon, P. Giguere, C. Ninham, and J. Guglielmo. Volume 2. In *Summary of Low-Speed Airfoil Data*. SoarTech Publications, 1996. ISBN 0-9646747-2-6.
- [26] Michael Selig. Summary of low-speed airfoil data. Volume 4.
- [27] Michael Selig, Andy Broeren, and Philippe Giguere. Volume 3. In *Summary of Low-Speed Airfoil Data*. SoarTech Publications, 1997. ISBN 0-9646747-3-4.
- [28] Michael Selig, James Guglielmo, Andy Broeren, and Philippe Giguere. Volume 1. In *Summary of Low-Speed Airfoil Data*. SoarTech Publications, 1995. ISBN 0-9646747-1-8.
- [29] E. Torenbeek. *Synthesis of Subsonic Airplane Design*. Delft University Press, 1982. ISBN 90-247-2724-3.
- [30] L.L.M. Veldhuis. Lecture notes for the low speed wind tunnel test 3. Course code: “AE3-193P”.
- [31] L.L.M. Veldhuis. Source code for the tu-delft ltt wind tunnel balance-measurment program. “program w3d” and “subroutine correc”.

-
- [32] A.D. Young. The calculation of the total and skin friction drags of bodies of revolution at zero incidence. Reports and memoranda no. 1874, Aeronautical Research Committee, April 1939.
- [33] Remco Zwinderman. Designing and production of a wind tunnel force measuring system for lightweight uav's. DAR-exercise Report.

Appendix A

Original Assignment Formulation

Proposal M.Sc. Thesis Project Dennis Trips

The main goal of the thesis work will be to find an optimal aerodynamic shape for a MAV aircraft participating in the EMAV09 competition held September next year in Delft. Because of the requirements of the competition ($< 500gr$, $< 50cm$), the study will focus on low Reynolds number aerodynamics.

The aim of the competition is to fly as far as possible, which implies that the design will have to be optimized for low drag. Because of the low Reynolds numbers involved, viscous drag will play a large role and a suitable method of modeling it will have to be found. A fitting method which is commercially available seems to be FLUENT, which allows finite volume calculations both in 2D and 3D.

3D Navier-Stokes calculations will likely be too cumbersome for application in an optimization process. Instead the optimization can be applied to 2D airfoil sections at different wing stations. Global characteristics like wing span, sweep, etc. could be determined using empirical methods. The resulting design can then be validated in 3D, also using FLUENT.

For the optimization itself a number of possibilities are available. The adjoint-equation method seems a good choice, but this would require the integration of the optimization algorithm with the flow solver, which in the case of using a package like FLUENT could be problematic. Other options are for example more conventional gradient based algorithms or some sort of evolutionary algorithm.

During the optimization process there needs to be close communication between the two other disciplines involved, being stability and electronics, to ensure a feasible design with sufficient flight characteristics.

Proposed professor: Michel van Tooren

Proposed tutor: Michiel Straathof

Expertise: MAVLab

Appendix B

Wing Geometry Details

Table B.1: Wing geometries used for the Quasi-3D validation.

	b	c_{root}	λ	$\Lambda_{0.25}$	root airfoil	tip airfoil	ϵ	S	A	c_{mac}
	[m]	[m]	[-]	[deg]	[-]	[-]	[deg]	[m ²]	[-]	[m]
wing001000	0.51	0.17	1	0	S5010	S5010	0	0.0867	3	0.17
wing000500	0.383	0.17	0.5	0	S5010	S5010	0	0.0487	3	0.132
wing000300	0.332	0.17	0.3	0	S5010	S5010	0	0.0366	3	0.121
wing201000	0.51	0.17	1	20	S5010	S5010	0	0.0867	3	0.17
wing401000	0.51	0.17	1	40	S5010	S5010	0	0.0867	3	0.17
naca2400	0.762	0.1693	0.5	0	naca2415	naca2409	0	0.0968	6	0.132
naca24150	0.762	0.1693	0.5	15	naca2415	naca2409	0	0.0968	6	0.132
naca24300	0.762	0.1693	0.5	30	naca2415	naca2409	0	0.0968	6	0.132
naca243085	0.762	0.1693	0.5	30	naca2415	naca2409	-8.5	0.0968	6	0.132
naca3-10-18	0.984	0.1487	0.33	0	naca23018	naca23009	0	0.0975	10	0.107

Appendix C

ATI Nano 17 SI-25-0.25 Data Sheet

Table C.1: Force range and resolution information for the Nano 17 SI-25-0.25.

Range			
F_x, F_y	F_z	T_x, T_y	T_z
25 N	35 N	250 Nmm	250 Nmm
Resolution			
F_x, F_y	F_z	T_x, T_y	T_z
1/160 N	1/160 N	1/32 Nmm	1/32 Nmm

Table C.2: Calculated stiffness information for the Nano 17 SI-25-0.25.

X-axis & Y-axis forces (K_x, K_y)	$8.2 \cdot 10^6$ N/m
Z-axis force (K_z)	$1.1 \cdot 10^7$ N/m
X-axis & Y-axis torque (K_{t_x}, K_{t_y})	$2.4 \cdot 10^2$ Nm/rad
Z-axis torque (K_{t_z})	$3.8 \cdot 10^2$ Nm/rad

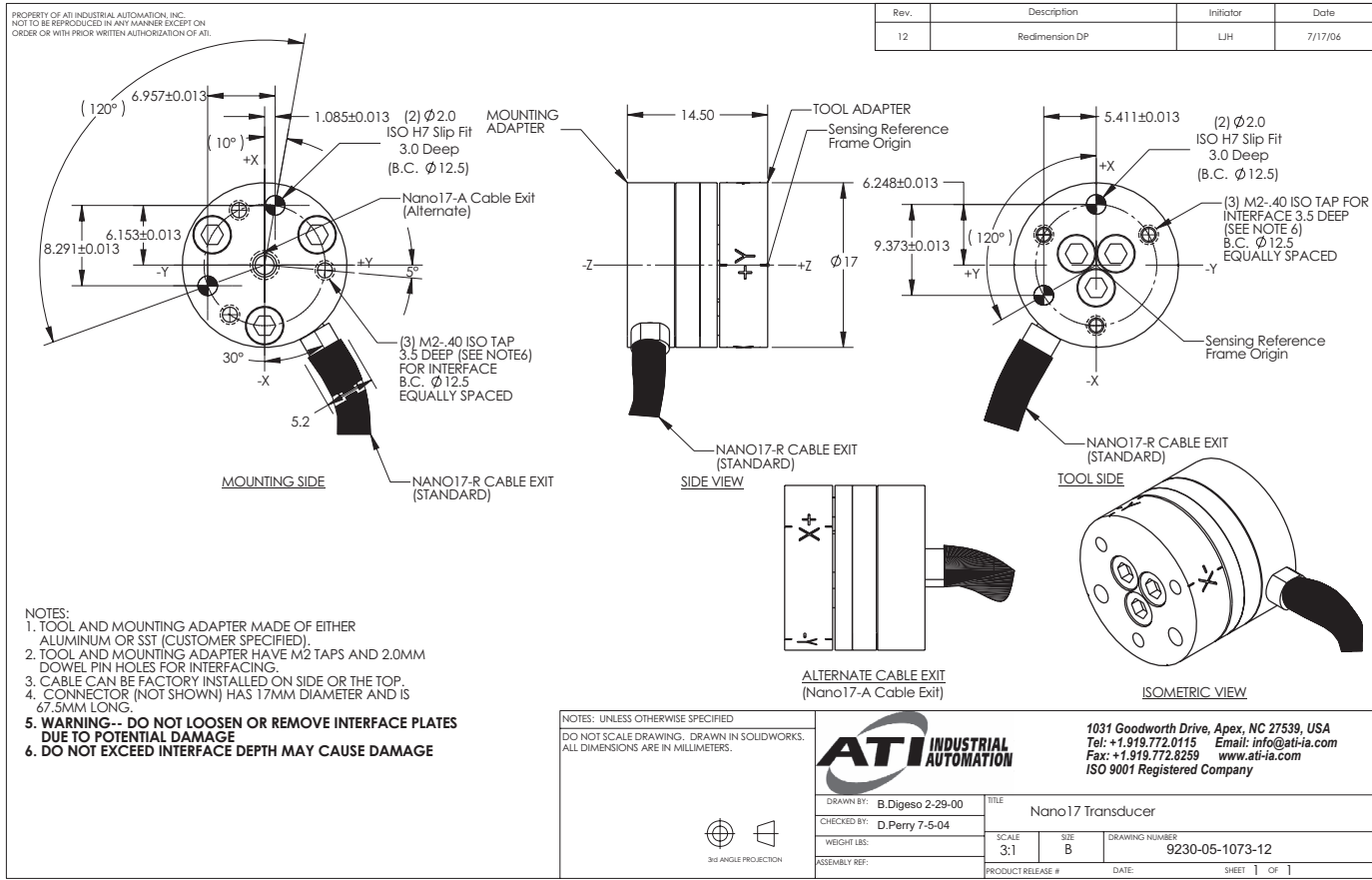


Figure C.1: Nano 17 dimensions.

Appendix D

3-Views

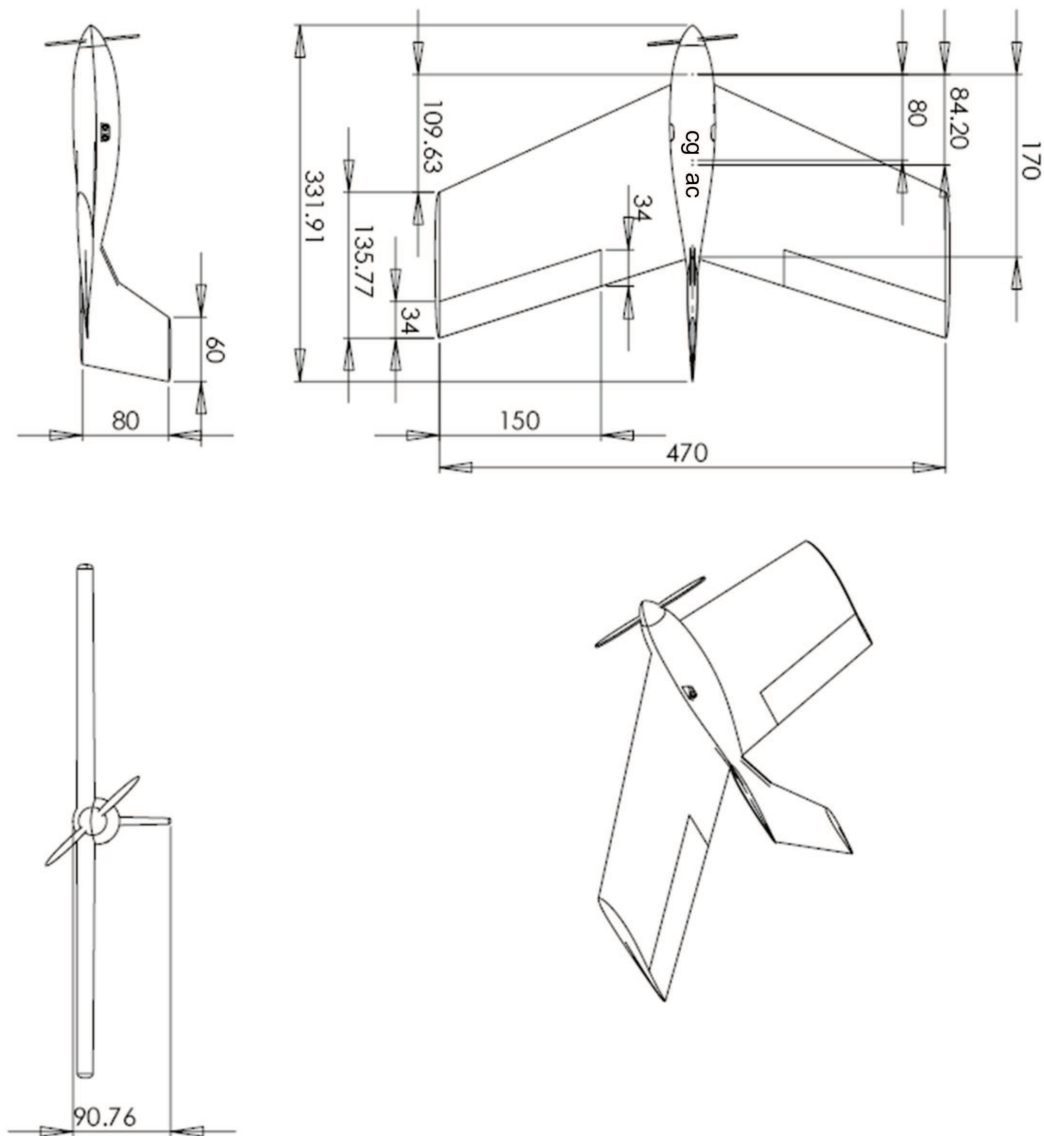


Figure D.1: Three view of Prototype A and the TRIP50.

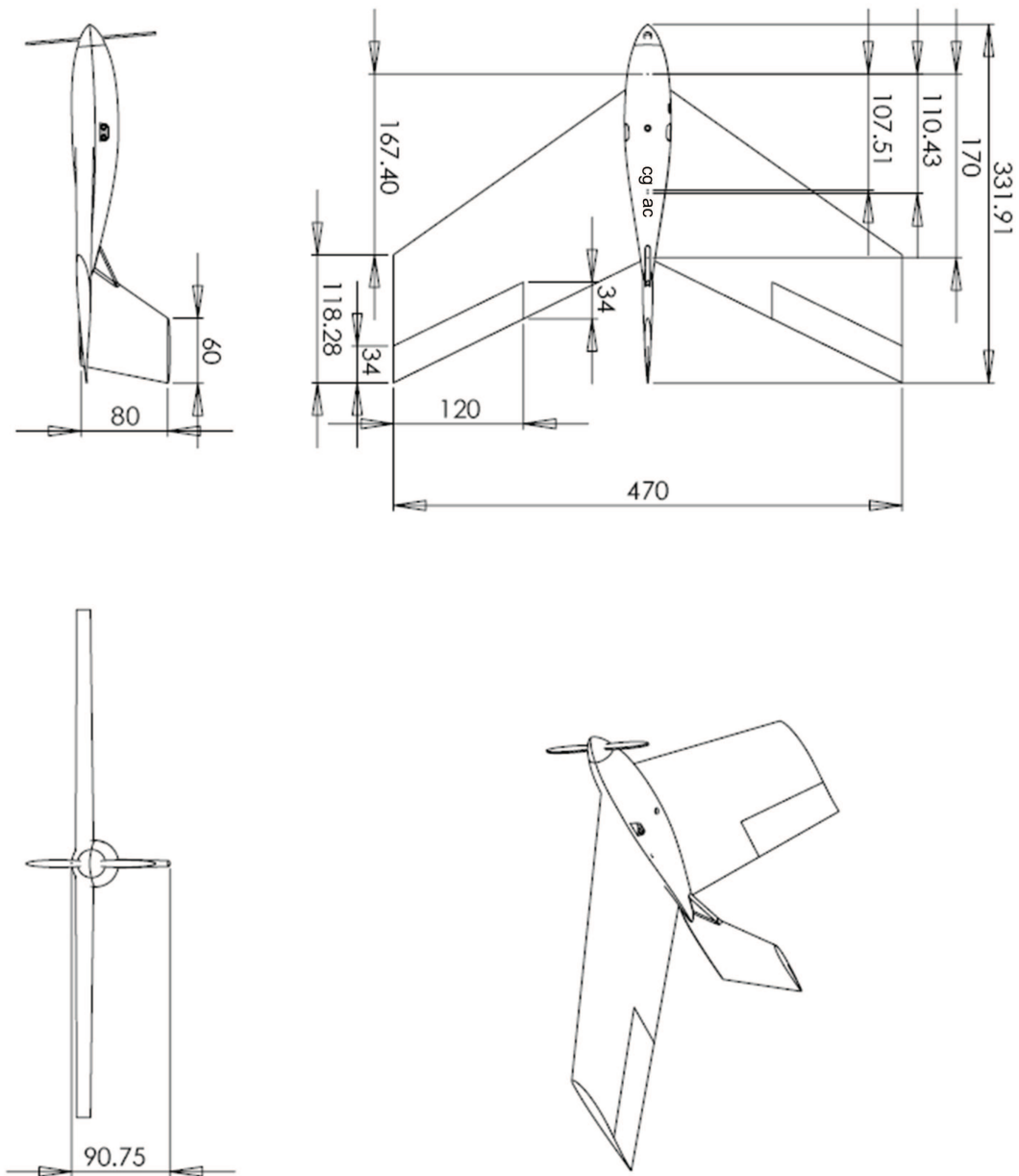


Figure D.2: Three view of Prototype B.

